8-2017

Novel processing approaches for thin film solar and related technologies.

Brandon Lavery
University of Louisville

Follow this and additional works at: http://ir.library.louisville.edu/etd

Part of the Other Chemical Engineering Commons

NOVEL PROCESSING APPROACHES FOR THIN FILM SOLAR AND RELATED
TECHNOLOGIES

By

Brandon Lavery
B.S., Case Western Reserve University, 2012

A Dissertation
Submitted to the Faculty of the
J.B. Speed School of Engineering
In Fulfillment of the Requirements
For the Degree of

Doctor of Philosophy
In Chemical Engineering

Department of Chemical Engineering
University of Louisville
Louisville, KY 40292

August 2017

NOVEL PROCESSING APPROACHES FOR THIN FILM SOLAR AND RELATED
TECHNOLOGIES

By

Brandon Lavery
B.S., Case Western Reserve University, 2012

A Dissertation Approved on

June 12, 2017

By the following Dissertation Committee

_____

Dr. Mahendra Sunkara (Dissertation Director)

_____

Dr. Thad Druffel (Dissertation Director)

_____

Dr. Xiao-an Fu

_____

Dr. Thomas Starr

_____

Dr. Sundar Atre

DEDICATION

This dissertation is dedicated to my friends and family back home. I couldn't have done it

without you.

ACKNOWLEDGEMENTS

ABSTRACT

NOVEL PROCESSING APPROACHES FOR THIN FILM SOLAR AND RELATED

TECHNOLOGIES

Brandon W. Lavery

June 12, 2017

A growing population along with developing nations are increasing the demand for
energy. The International Energy Agency forecasts a global electricity demand increase of
70 percent by 2040. This is an increase from nearly 18 TW to over 30 TW. The sun can be
a great clean source of achieving this energy demand. Despite the large solar industry
development, the market is still growing as solar energy only accounted for 0.87% of the
global energy production in 2013. The opportunity exists to manufacture more affordable
solar energy that can penetrate more of the global energy market. In this dissertation, a
photonic-based manufacturing technique called intense pulsed light (IPL) was investigated
to enhance the photovoltaic properties of CdTe, better understand the $CdCl_2$ treatment used
to create higher efficiency CdTe solar devices, enable the first sintering and efficiency
enhancement of perovskite solar cell (PSC), and study the possible conversion of a stable
2D perovskite to a 3D perovskite.

CdTe thin films grown by low temperature electrodeposition were treated for the
first time with IPL. The low temperature electrodeposition growth resulted in films
consisting of nanoparticles, with reduced melting point temperatures. In combination with
the high temperature rise produced by the pulses of light, the lower melting temperature

resulted in pores/voids being filled as well as enhanced grain growth. As a result, pin-holes and grain boundary recombination were diminished. Subsequently the fill factors of PV devices created using this technology significantly increased. In addition, the IPL also successfully improved the crystallinity in the CdTe films by photonically initiating the popular $CdCl_2$ treatment. To understand the mystery behind the mechanism of the $CdCl_2$ treatment, low temperature PL was utilized and new electrodeposition precursors resulting from the study improved device efficiencies.

Photoactive perovskite $CH_3NH_3PbI_3$ layers were successfully sintered with a novel IPL treatment with efficiencies exceeding 12%. The processing time was reduced to 2 ms, which was significantly faster than those from previous reports. Additionally, the average performance of the IPL-processed samples showed an improvement compared to the hot-plate-processed samples. This advance creates an exciting new method to quickly create dense layers of perovskite, eliminating the rate-limiting annealing step detrimental to industry adoption, and shows the first known occurrence of sintering in $CH_3NH_3PbI_3$ perovskite particles.

Lastly, the fast photonic processing of the IPL enabled the first conversion of a stable 2D perovskite structure into a 3D structure. This caused an band gap shift from 2.0 eV to 1.6 eV and showed the capabilities of band gap tuning enabled by the IPL. While this work is the first documentation of band gap tuning enabled by a photonic effect, it presents a possible inexpensive manufacturing technique that could use one material to create several different colors for the future development of pixel-based LED displays.

TABLE OF CONTENTS

LIST OF FIGURES

CHAPTER 1

INTRODUCTION

1.1 Global Energy Outlook

A growing population along with developing nations are increasing the demand for energy. The International Energy Agency forecasts a global electricity demand increase of 70 percent by 2040.[1] This is an increase from nearly 18 TW to over 30 TW.[2] The sun can be a great clean source of achieving this energy demand. It continuously delivers 174,000 TW to the upper level of Earth's atmosphere.[3] After taking into account atmospheric absorption and scattering, latitude-dependent oblique incidence, seasonal variation, and cloud cover, the global-average solar irradiance over land is 183 W/m^2.[4] To meet the 12 TW increase in energy, 437,160 km^2 of 15% efficient solar panels would be needed. Knowing the Earth has a land surface area of 149 million km^2, this would correspond to only 0.3% of the land being covered with solar panels.[5]

Unlike other forms of emerging renewable energy like thermal generators and wind turbines, solar panels have no moving parts that require maintenance and they retain high efficiencies independent of the size of their application.[6] Another advantage of solar energy is that it can be used anywhere in the world unlike fossil fuels and other extractive sources of energy that may not be readily available in a region. Because of these advantages, there has been rapid growth in the solar market. Between 2000 and 2014, global solar energy capacity doubled nearly every two years and grew from 1.3 GW to 139 GW.[7] Even with these advances, the market is still growing as solar energy only accounted for 0.87% of the

global energy production in 2013.[6] The opportunity exists to manufacture more affordable solar energy that can penetrate more of the global energy market.

1.2 Designing the Next Generation of Solar Energy

To date, the most popular solar energy material being used is silicon. Crystalline silicon (c-Si) solar cells constitute 90% of current global production capacity and are the most mature of all PV technologies with over 60 years of research.[6] Silicon can be manufactured into non-toxic, efficient, and extremely reliable solar cells. However, it may not be the ideal candidate for solar energy needs. Silicon is inherently an indirect bandgap semiconductor which leads to weak light absorption and requires thicknesses of over 100 µm in the absence of light trapping techniques to achieve highly efficient solar cells.[6] This may not appear to be an obstacle, but it restricts fabrication substrates to bulky panels and prevents the industry from advancing toward cheaper and more ergonomic flexible plastic substrates. As silicon prices have continued to decrease over time, module costs are becoming a higher percentage of the total cost of the silicon solar cell (exceeding 35%) as designs and materials remain largely unchanged.[8] The majority of these module costs come from the glass, backsheet and frame with no cheaper replacements anticipated in the upcoming years.

Efforts to decrease the cost of manufacturing related to the solar industry have motivated researchers to create next generation solar cells. When creating next generation solar cells, the first requirement is to find a material that absorbs as much of the solar spectrum as possible. The solar spectrum consists of wavelengths spanning from the ultraviolet, to the visible and infrared sections of the electromagnetic spectrum. As it passes through Earth's atmosphere, light of less than 300 nm is filtered out by atomic and

molecular oxygen, ozone and nitrogen. At the higher end of the electromagnetic spectrum, infrared is mostly absorbed by water and carbon dioxide (CO_2). Given these filtered regions, the greatest irradiance is between the visible wavelengths of 300-800 nm **(Figure 1.1)**, so the ideal solar cell should absorb in this range of wavelengths.
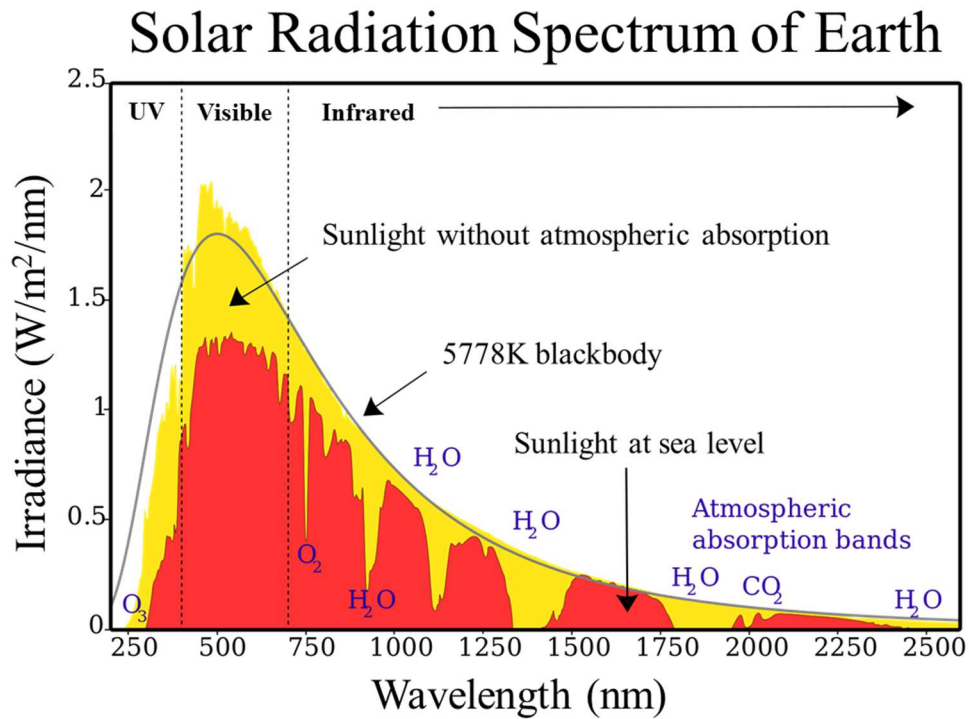
Figure 1.1. Solar spectrum of Earth including regions absorbed by atmospheric gases H_2O and CO_2

The next fundamental requirement for the material is to be able to separate charges and produce electricity. As the material absorbs sunlight, it will need to promote an electron from the ground state to a state of higher energy (excited state) that can be extracted in the form of electricity. This level of separation from the ground state to the excited state should be large compared to the Boltzmann's constant K_bT and contain at least two or more energy

3

levels. Materials with these characteristics are called semiconductors and contain a separation of energy levels called the band gap.

Within semiconductors there are two distinct classes of band gaps, the direct and indirect band gap. Of the two, a direct band gap semiconductor would be desirable for next generation solar cells because they have a higher efficiency in separating charges, leading to less material needed to absorb the solar spectrum. Less material usage saves cost in manufacturing and produces thinner materials with enhanced flexibility that can be used on roll-to-roll processes. Meanwhile, indirect band gap semiconductors like silicon require an additional momentum change from lattice vibrations (phonons) in addition to solar energies greater than the band gap to generate charge separation. This additional momentum requirement means that solar absorption is usually weaker in indirect semiconductors so thicker devices incorporating these materials are needed to fully absorb the solar spectrum. The solar cells based on indirect semiconductors require more material to manufacture and have limited flexibility leading to rigid panels.

The last primary objective in finding next generation solar cell materials is finding abundant low cost materials that can be fabricated near atmospheric conditions without the need for expensive vacuum or high temperature manufacturing. This is difficult to find in semiconductor materials as they typically require chemical vapor deposition (CVD) performed under vacuum to achieve highly crystalline materials with minimized defects. The defects are further minimized by using high temperature treatments to anneal and eliminate defects in-between crystals.

Of the current and emerging next generation solar cell technologies, cadmium telluride and perovskite solar cells (PSCs) are among the most promising and are

categorized as thin film solar. They require device thicknesses on the nanometer range, reducing material usage and providing the opportunity to create new solar array form factors on flexible substrates. Additionally, thin film solar technologies will produce less greenhouse gas emissions during production compared to c-Si PV (45 g CO_2-equivalent per kWh for c-Si, 21 g CO_2-eqivalent per kWh for a-Si:H, 14 g CO_2-equivalent per kWh for CdTe, and 27 g CO_2-equivalent per kWh for CIGS solar cells).[9-10]

Cadmium telluride heterojunction solar cells with cadmium sulfide have long been considered as an alternative to silicon based solar cells. The technology has a global photovoltaic (PV) market share of 5% and leads the thin film market with 56% in 2013.[11] This combination of semiconductors from groups II and VI have attained efficiencies of greater than 21%.[12] Although efficiencies were largely stagnant from 1992 to 2012, devices have improved considerably by over 4% in the last 5 years with the implementation of graded band gap architectures that can achieve IPCE values of over 140% due to impact ionization effects.[13] With a band gap of ~1.5 eV, CdTe solar cells have a high absorption coefficient $> 5 \times 10^5$/cm and can achieve high efficiencies in thin cells within 2 μm.[14]

As mentioned previously, PSCs have also attracted increased interest in thin film solar manufacturing with efficiencies exceeding 22%.[15] The term "perovskite" refers to the ABX_3 crystal structure. In the case of the organometal halide perovskite, the A site refers to an organic group, B represents a metal such as lead, and X is a halide group such as iodide, chloride, or bromide **(Figure 1.2)**.[16] Unlike traditional semiconductor solar cells, the PSC is amenable to changes in the atoms of its crystal structure. This opens up many possibilities in tuning band gaps,[17] as the optical bandgaps can be tuned from 1.25 to 3.0

eV by cation (A, B) or anion (X) substitution (e.g., $HC(NH_2)_2$-$Pb(I_{1-x}Br_x)_3$,[17] $CH_3NH_3SnI_3$,[18-19] and $CH_3NH_3Pb(I_{1-x}Br_x)3$.[20]
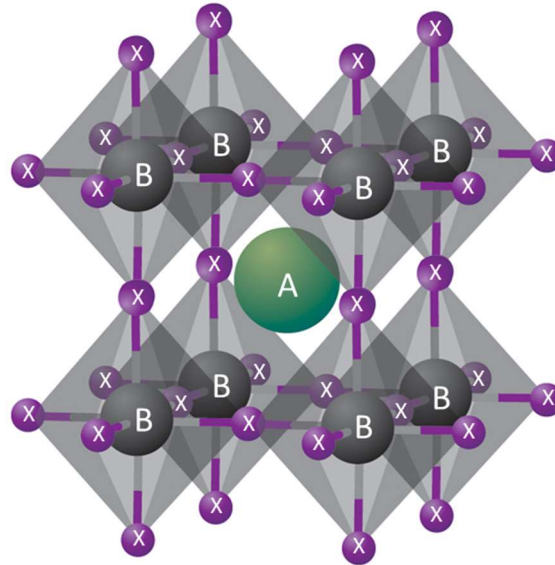
Figure 1.2. The perovskite ABX_3 crystal structure. In the case of the organometal halide perovskite, the A site refers to an organic group, B represents a metal such as lead, and X is a halide group such as iodide, chloride, or bromide

Beyond the large material sets that enable band gap engineering and durability, the PSC technology offers a processing advantage using solution phase depositions and low temperature synthesis. The majority of the PSC devices reported in the literature, including the highest performing cells, use low cost and low temperature techniques. PSCs form at temperatures below 200 ºC compared to the 800-900 ºC temperatures needed to fabricate crystalline silicon solar cells.[21] Reductions in heat treatment will generate cost savings in solar cell manufacturing, enabling a cheaper product that can be sold to more consumers. The low temperature synthesis of PSCs also promotes different cell configurations,[22-23] and promotes multiple processing techniques and the possibility for roll-to-roll manufacturing.[24-25]

1.3 Challenges in Thin Film Solar

CdTe and perovskite solar cells share similar challenges. Both are in need of faster low temperature annealing techniques that enlarge crystal grains. Grain boundaries exist in-between crystal grains that cause recombination centers leading to decreases in solar cell device efficiencies, so it is beneficial to grow crystal grains to eliminate their occurrence.

For the CdTe system, the highest devices are still those created using closed space sublimation (CSS). Closed space sublimation uses a vacuum environment and high temperatures to sublimate CdTe precursors to substrates in close proximities in excess of 400 °C. Low temperature CdTe solar cells can be fabricated using a technique called electrodeposition. A known shortcoming of electrodeposited CdTe films are their resulting small grains that limit devices from achieving high efficiencies. For the electrodeposited CdTe solar cells to achieve higher efficiencies comparable to those using the CSS technique, a second higher temperature annealing step is required.

In the case of the PSC, crystal growth is desired but thus far conventional annealing methods used on other semiconductors have not been applicable to the perovskite material. A problem that often arises when annealing at high temperatures is reduced surface coverage, resulting in the formation of perovskite islands due to agglomeration during heating. Eperon et al. demonstrated that as the annealing temperature increases, the number of pores in the final film decreases, but the size of the pores increases and the morphology transitions from a continuous layer into discrete islands of perovskite.[26] An active layer morphology composed of discrete islands can create multiple shunting pathways by exposing the underlying contact and severely dampens solar cell performance. Creating larger perovskite crystals and improving the surface coverage of perovskite films is

therefore important for optimizing device performance and has been a topic of discussion in PSC research.

Initially researchers improved the crystal formation by utilizing a two-step sequential deposition of PbI_2 followed by methylammonium iodide (MAI).[23] Recently, a more expedient one-step deposition of $CH_3NH_3PbI_3$ was advanced by using solvent-solvent extraction techniques. These techniques utilize low boiling point solvents such as diethyl ether to remove high boiling point solvents such as N-Methylpyrrolidone (NMP) or Dimethylformamide (DMF) from the perovskite films after spin coating.[27-28] While these solvent-solvent extraction techniques can be used to produce highly efficient solar cells with larger grains, they add another step in the perovskite manufacturing process and require the use of hazardous chemicals such as diethyl ether, toluene, or chlorobenzene.

1.4 Proposed Approach

While perovskite and CdTe solar cells are impressive candidates for flexible substrates, given their high performance as a thin-film, both still require long annealing times of excess of an hour. This is detrimental to roll-to-roll processing and creates a bottleneck in a continuous operation. To overcome this, a new technique called intense pulsed light (IPL) will be used to manufacture CdTe and PSCs. The IPL process **(Figure 1.3)** delivers high-energy pulses of light from a Xenon flash lamp in a very short duration over a large processing area, able to heat thin films containing photosensitive materials to temperatures exceeding several hundred degrees Celsius.[29-30] The light energy absorbed by the thin films results in a near instantaneous rise in temperature that lasts for the duration of the pulse, commonly a few milliseconds. These thin films exist on a substrate carrier with a thermal mass many times larger hence the time to establish thermal equilibrium

8

between the film and the substrate exceeds that of the flash. Consequently, the high temperatures are not transmitted into the substrates as the amount of heat energy introduced is quickly dissipated.[31] Thus the process focuses heat only where it is necessary, which is on the thin film and can be implemented on more fragile organic substrates such as polymers and papers.
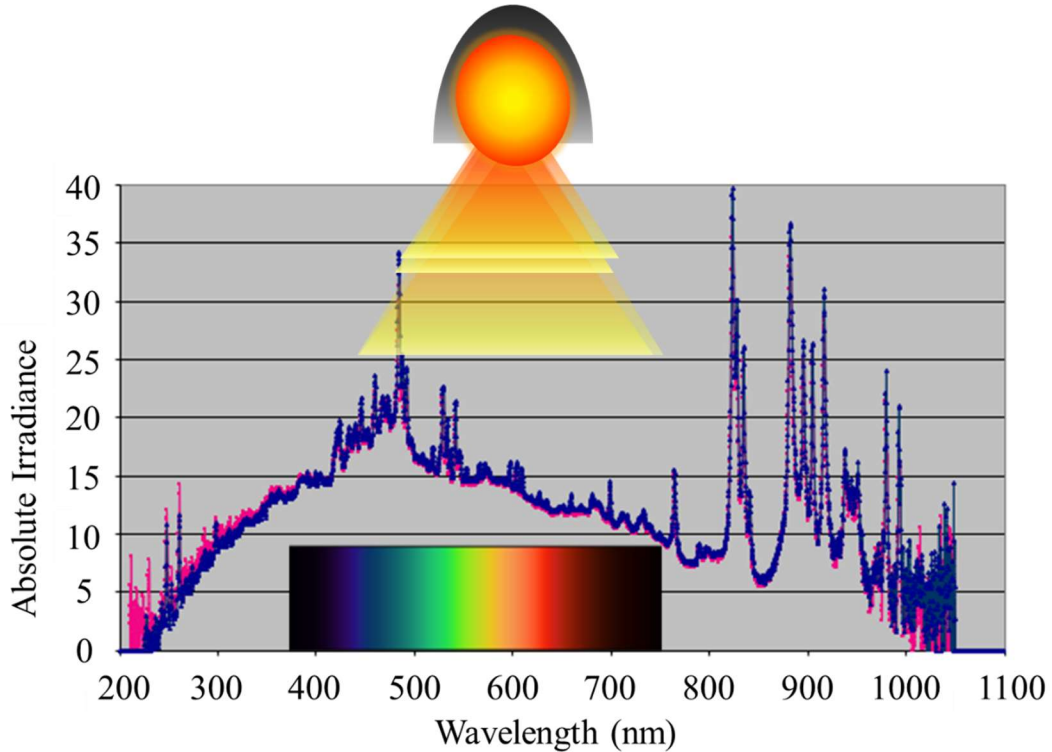
Figure 1.3. Schematic of the Intense Pulse Light (IPL) displaying the wavelengths emitted from the Xenon plasma flash lamp with a color guide as reference

Bulk CdTe has a high melting temperature of 1092 °C, so it is unlikely the IPL processed films would be able to reach temperatures high enough to induce changes in the film. However, electrodeposited CdTe exhibits much smaller grains on the nanometer scale. Reducing the size of a semiconductor to the nanoparticle regime is known to produce significant physical and chemical changes to a material's behavior. Within this size range, quantum confinement effects created by these extremely small sizes results in a rise in the

optical bandgap of the semiconductors, whereas the enhanced surface area can improve the materials photocatalytic properties.[32-33] Increasing the surface to volume ratio of the semiconductor particle can also yield a substantial depression in the melting point temperature.[34] This effect is caused by the relatively smaller cohesive energy of atoms positioned at the surface of a film or particle compared to the atoms in the bulk. Consequently, the temperature needed to melt the surface is lower than for the bulk of the material. Typically, a particle size less than 20 nm in diameter is needed to produce a decrease in the melting point temperature by a few hundred degrees centigrade.[35-36] This characteristic is beginning to be employed in the printed electronic industry in order to produce conductive metal patterns on low temperature substrates for metal nanoparticulate inks.[37] However, this development has yet to be fully exploited in the semiconductor manufacturing industry.

Unlike the CdTe system, the perovskite in PSCs does not need to be in the nanoparticle regime to have a melting point temperature low enough for IPL processing. As previously mentioned, high temperatures exceeding 150 °C are known to cause degradation of the material. For the perovskites used in PSCs, a different strategy based on sintering will be used for the IPL processing. Sintering is the process of particles converting into a coherent object of controlled density and microstructure at an elevated temperature (but below the melting point) due to the thermodynamic tendency of the particle system to decrease its total surface and interfacial energy.[38] The recognized forms of solid-state transport sintering mechanisms include: surface diffusion, volume diffusion, grain boundary diffusion, viscous flow, plastic flow, and vapor transport.[39] In the initial stage, particles begin to bond to one another through necking. In this stage, the surface area is

still at least 50% of its original value. In the intermediate phase, pores are smoother and grain growth occurs. Then in the final stage, pores are spherical and closed and total porosity is less than 8%. Sintering generally uses multiple mechanisms to achieve a densified layer. The sintering in the perovskite could be induced by vapor phase transport, solid-state growth of particles, the melting of the organic components and the formation of new seed sites, the breaking and reforming of hydrogen bonds, the transport of halide ions across surfaces to enable new seed sites at boundary interfaces, etc. Literature proposes that the most likely scenario for the sintering of perovskites used in PSCs is the local evaporation and condensation of the material **(Figure 1.4)**. This form of sintering dominates the sintering of low-stability materials such as lead and lead-based compounds and also in halide complexes.[39] In evaporation-condensation sintering, vapor transport leads to the repositioning of atoms located on the particle surface without densification. Evaporation occurs from a surface and transport occurs across pore space, leading to condensation on a nearby surface. The sintering is controlled by the equilibrium vapor pressure:

$$P = P_0 \exp\left(\frac{-Q}{kT}\right)$$

in which the equilibrium vapor pressure (P) depends on the absolute temperature (T) with an Arrhenius dependence (thermally activated), P_0 is the pre-exponential material constant, and Q is the activation energy for evaporation with k being the Boltzmann constant. From the above equation, higher temperatures correspond to higher vapor-pressures and increased vapor-phase transport, as flux depends on the evaporation rate. The condensation occurs in-between particles where the vapor pressure is below equilibrium.
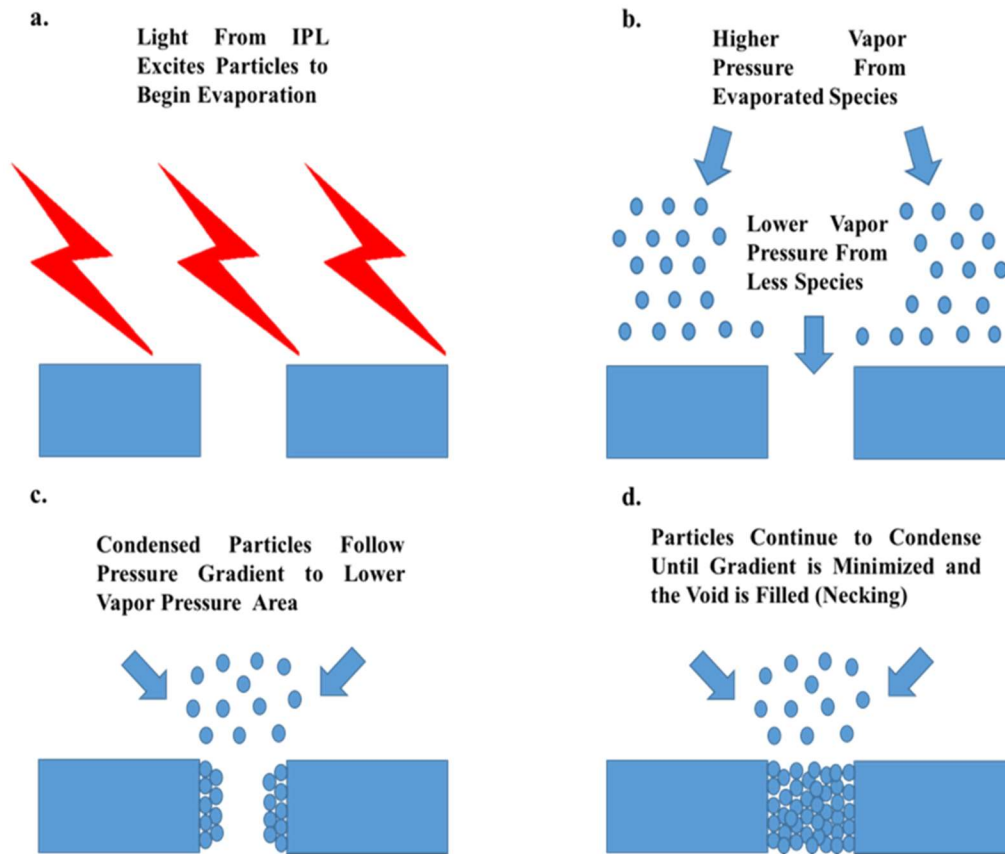
Figure 1.4. Illustration of proposed sintering mechanism of $CH_3NH_3PbI_3$ perovskite

1.5 Objectives of This Study

The main goal of this study is to enhance the processing of CdTe and PSCs by utilizing a low cost and faster IPL manufacturing technique. Using the IPL to photonically process these materials and enhance their efficiencies will aid in the processing of next generation thin film solar energy on more affordable plastic substrates. Meanwhile the objective of this dissertation is to understand the capabilities of IPL processing through its effects on a variety of materials.

1.5.1 Specific Objectives

a) Enlarge the grain size of electrodeposited CdTe through IPL processing and determine the optimal processing window.

b) Understand the effects of the IPL on the crystal orientation of CdTe as well as its electronic properties.

c) Use the IPL to initiate the $CdCl_2$ treatment of electrodeposited CdTe and understand the reaction that enables higher efficiency devices after being exposed to $CdCl_2$.

d) Sinter perovskites used in PSCs using the IPL to create a thermal technique that can be used on temperature sensitive solar materials.

e) Improve the repeatability of creating high efficiency PSCs. The PSC is known to have large deviations in efficiency resulting from wet chemistry synthesis.

f) Develop a method using the IPL to change the band gap of perovskites. Being able to change the band gap of perovskites with a simple photonic technique like the IPL could encourage new developments in tandem solar cell design as well as the LED pixel display research.

1.6 Organization of Thesis

Chapter 1 will provide emphasis for the need of solar energy research, documenting the growing energy demands in the world. It will continue by developing the challenges associated with providing more affordable solar energy and provide the basic background knowledge necessary to understand the development of next generation solar cells. The next generation "thin film" CdTe and perovskite solar cells will be introduced along with their need for more inexpensive fabrication manufacturing. The proposed approach to solving these manufacturing issues by using IPL processing methods and the specific objectives associated with understanding this research endeavor conclude the introduction section of the thesis.

Chapter 2 delivers a comprehensive review for the state-of-the-art solar cells, and their operating principles. It concludes by discussing the manufacturing challenges that compromise the development of next generation solar cell technologies.

Chapter 3 details an overview of the experimental procedures used to fabricate CdTe and PSCs. Each step of the experimental procedure will be dissected and explained to provide insight on the problems presented in thin film solar research. In addition, the section highlights the characterization techniques and tools that provide understanding of the materials physical, optical, and electrical characteristics.

Chapter 4 shows the results of IPL processed CdTe solar cells. It documents the changes underwent by electrochemically deposited CdTe and delivers a proof of concept that IPL processing can be used for solar cell research.

Chapter 5 continues to access the problems of the CdTe solar cell. In this chapter the popular $CdCl_2$ treatment is investigated and utilized in IPL processing. Furthermore, the findings of the $CdCl_2$ treatment mechanism prompted studies of changes needed in the precursor solutions of electrochemically deposited CdTe. The results of these changes and improvements to the CdTe solar cells are discussed.

Chapter 6 documents the first ever sintering of the perovskite material used in PSCs and discusses improvements made to its operation. This section illustrates the effects of IPL processing on the perovskite material used in PSCs and provides a process map for roll-to-roll manufacturing using the IPL.

Chapter 7 investigates another intriguing feature of PSCs: the ability to tune band gaps. The highlights of this chapter provide the first ever transition of a stable 2D layered

perovskite to a 3D perovskite and provide a material that could someday be a possible entry into the LED pixel display market.

The conclusion and recommendations of this study can be found in chapters 8 and 9, respectively.

CHAPTER 2

BACKGROUND

2.1 Solar Cell Background

In 1839, Becquerel at the age of 19 was the first to uncover the possibilities of using solar to generate electricity when he described the photoelectric effect by generating electricity in an acidic bath using AgCl or AgBr electrodes.[40] The first solar cell material was later developed in 1877 by Adams and Day when they noticed a photoconductive effect in selenium.[41] They attributed the generated current to light induced crystallization of the outer layers of the selenium bar. This process wasn't well understood until the development of semiconductor physics several decades later.

2.11 Semiconductor Physics of Solar Cells

There are several different device architectures and materials used to create solar cell devices. Here, the basic fundamentals that can be applied to all solar cell devices will be discussed to lay the ground work for a more detailed look into the CdTe and perovskite solar cell technologies.

As mentioned in the introduction, solar cells consist of a class of materials called semiconductors. Semiconductors possess a band gap between the occupied states (valence band) and higher energy unoccupied states (conduction band) that is necessary to provide the electrical energy from the extra potential energy that electrons gain from photon absorption **(Figure 2.1)**. The band gap is crucial to solar cell materials, if the band gap is too large as is the case in insulating materials, then most of the energy from the sun will be

insufficient to excite electrons from the valence band to the conduction band and generate electricity. If the band gap is too small like in the case of metals, then the excited electrons do not remain long enough in the higher energy levels to be extracted as electricity. The bands in semiconductors come from the difference in energy levels formed from molecular orbitals arranged at different energy levels. The molecular orbitals originate from the formation of pairs of atomic orbitals. As an increasing amount of atoms are introduced to form a solid, each atomic orbital splits to form a very large number of bands that are so close in energy that they collectively form a band of allowed states. The discrete bands of allowed states are primarily due to the Pauli exclusion principle, which forbids more than two electrons as fermions with spin up and down to occupy one state which causes the energy levels to split. To analyze the crystal band structure of a material, these bands are mapped on a chart of energies (E) vs. wavevector (k) **(Figure 2.1).** The wavevector (k) is used in the Schrödinger's equation to calculate of the energy levels of an atom or molecule.
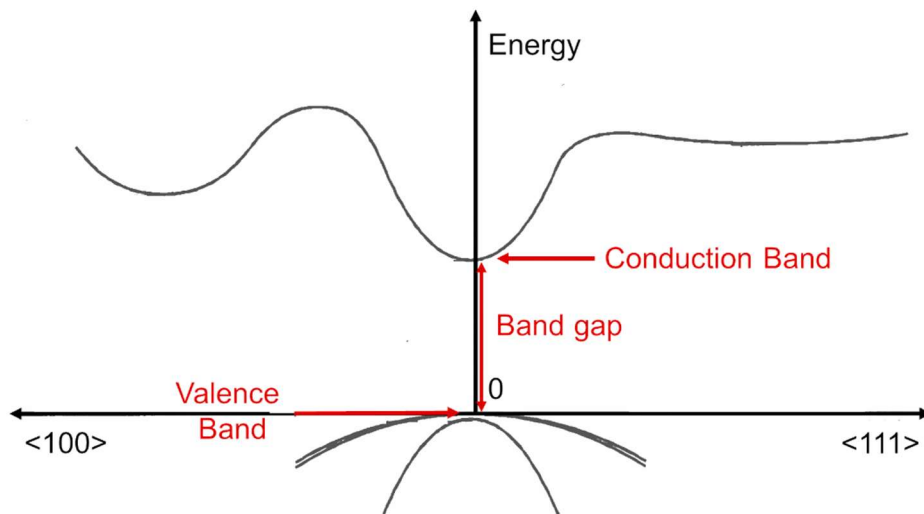
Figure 2.1 Crystal band structure of a semiconductor material, with bands mapped on a chart of energies (E) vs. wavevector (k)

When an electron is removed from a bond between atoms and injected into the conduction band by either by thermal or solar (photonic) input energy, it leaves behind a positively charged region from the vacancy of an electron effectively called a hole. This movement of holes and electrons enables the generation of electricity. For easier generation of holes and electrons, impurity materials with valence electron numbers differing from that of the native atoms can be introduced in a process called doping. Doping is essential to the homogeneous solar cell devices like silicon. Materials that have an injected excess of electrons become negatively charged (n-type) while materials with an excess of holes become positively charged (p-type). In addition, materials generally lacking in charge are known as intrinsic (i-type). For the holes and electrons to move within a solar cell, there needs to be a driving force. This driving force occurs at junctions in a solar cell in which p-type, i-type, or n-type materials come in contact with one another and create an electric field under illumination. The three main contributions to the charge separation at the junctions in a solar cell are: gradients in the vacuum level or work function, gradients in the electron affinity, or gradients in the band gap. Of the three, the most common in today's silicon solar cells use the gradients in the vacuum level or work function by means of doping. The work function is defined as:

$$\Phi = (E_{vac} - E_F)$$

where Φ is the work function, E_{vac} is the energy at vacuum, and E_F is the Fermi Level. The Fermi level (E_F) is described mathematically by using Fermi Dirac statistics when the Fermi Dirac function f_0 is equal to 1/2:

$$f_0(E, E_F, T) = \frac{1}{e^{(E-E_F)/k_B T} + 1}$$

in which f_0 is the fermi dirac function, E_F is the fermi level, k_B is the Boltzmann constant, and T is the temperature

When in equilibrium under illumination, E_F is a constant, causing an electric field between any two regions of differing work functions from the gradient in E_{vac}. This causes band bending, as the quasi fermi levels from each side of the junction must be the same **(Figure 2.2).**
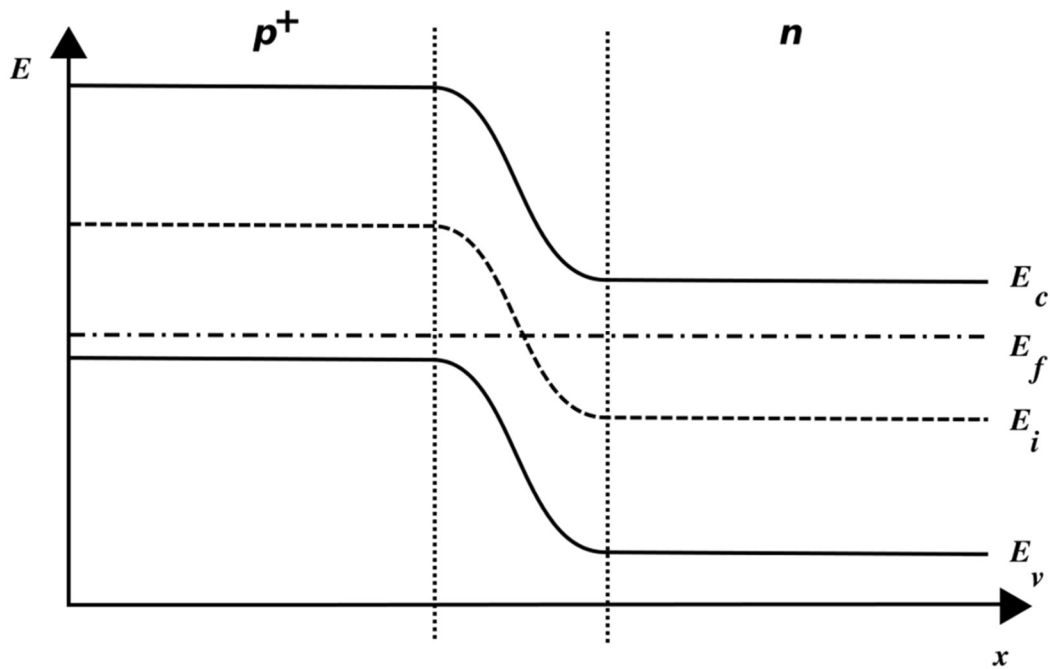
Figure 2.2. Band bending in a semiconductor p-n junction induced by an electric field

Rather than doping, next generation thin film solar devices like CdTe and the PSC utilize multiple materials in heterojunction architectures. In this approach, the materials themselves will be of differing p, i, or n types. The heterojunctions used in thin film solar cells are enhanced by the last two previously mentioned major contributions to the charge separation at the junctions in a solar cell: gradients in the electron affinity, and gradients in the band gap. The disadvantages in using heterojunction designs are the discontinuities in

the conduction and valence band edges at the junction resulting from mismatches in the lattices of the two materials. These mismatches can cause sub-band Schockley Read Hall recombination centers in solar cell devices and limit efficiencies. Other known issues are the diffusion of one material into the other, and the formation of alloys at the junctions.

2.2 CdTe solar cell design

The first CdTe solar cell was reported in 1972 by Bonnet and Rabnehorst when they created a 6% efficient heterojunction CdTe-CdS p-n device. Most of the devices still retain this architecture, incorporating interface layers to improve durability; although newer designs include graded bandgaps to improve efficiencies. The two main methods for depositing CdTe are physical vapor deposition (PVD) and electrodeposition. The PVD process can produce larger grains; however, the electrodeposition technique has advantages in selective doping and can be implemented at a lower cost. The CdTe devices in this dissertation are electrodeposited with an architecture consisting of glass as the substrate with fluorinated tin oxide (FTO) as the conductive oxide, n-type cadmium sulfide (CdS), n-type CdTe, p-type CdTe, and gold (Au) **(Figure 2.3)**.
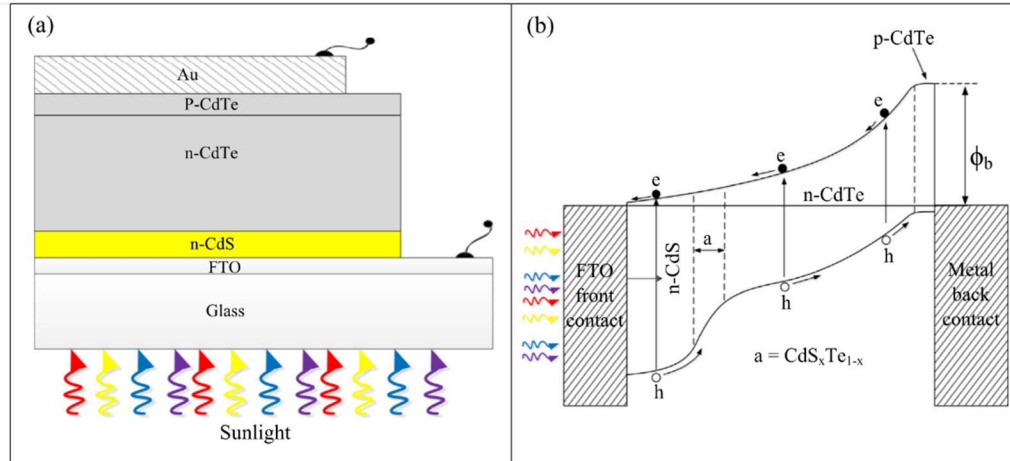
Figure 2.3. (a) Schematic diagram and (b) energy band diagram of the glass/FTO/n-CdS/n-CdTe/p-CdTe/Au thin film electrodeposited CdTe solar cells

The CdTe layer can be grown either n-type or p-type depending on growth conditions.[42-43] Cadmium-rich CdTe is n-type due to the Fermi Level being pinned near the mid gap by Cd^{2+} donors, while tellurium-rich CdTe is p-type as the Fermi Level is pinned close to the valance band.[44] The diffusion length of CdTe is between 1 and 5 μm, so devices are typically constructed in this regime.[45] This is not detrimental to device performance because of the great absorption capabilities of CdTe, displaying over 90% absorption coefficient of photons > 1.45 eV in only a few microns.[46-48]

Although the CdS layer of the CdTe solar cell does not absorb large amounts of energy compared to CdTe because of its larger band gap, it serves many purposes in CdTe solar cell devices such as: enhancing the crystallinity during the formation of the CdTe layer, facilitating the formation of large band gap $CdTe_{1-x}S_x$ mixed crystal layers near the CdS-CdTe interface that improve the properties of the CdTe absorber layer, and providing a "buffer layer" that prevents the interfacial mismatch between the FTO and the CdTe layers.[45, 49] Because of its usage, the CdS layer should be thin (50-100 nm) to provide a

high transmission for the absorbing CdTe layer and uniform to prevent shorting of the device.[49]

2.3 CdTe Manufacturing Issues

CdTe manufacturing is much further in development than the PSC, so several of the significant issues like device lifetime have already been solved by the industry. However, as silicon prices continue to drop, CdTe solar cells will need to implement more inexpensive manufacturing efforts to stay competitive. The first way to reduce the cost of the manufacturing of CdTe solar cells is to reduce the thickness of the CdTe absorber layer to reduce material costs. Tellurium is a scarce material and cadmium is a known toxic health hazard, so successfully reducing CdTe absorber layer thickness from 3-8 μm to a 1 μm design would be economically advantageous.[50] Research has improved in thinner CdTe devices, Gupta et al. achieved an efficiency of 9.7–11.8% for ultrathin CdTe devices of 0.7–1.28 μm compared to standard device with 2.3 μm CdTe (13%).[51] When creating thinner CdTe devices, surface morphology suffers; creating a high density of non-uniform weak diodes and poor yield of high efficiency devices.[51] Another improvement that could be made in the manufacturing of CdTe would be to eliminate or alter the toxic chlorine atmosphere used to activate the junction.[52] Improving this step will help alleviate safety costs. The last improvement that will be mentioned here is to eliminate the high processing temperatures (400-600 °C). Eliminating these steps will reduce the energy costs in the manufacturing. Aside from the obvious energy cost savings, changing the annealing step would prevent the diffusion of harmful substrate materials into the CdS and CdTe layers. Indium can diffuse from indium tin oxide (ITO) transparent conducting oxides during the annealing stages and results in a loss of V_{oc} and facilitates direct contact between CdTe and

ITO via pinholes in the window layer.[49] Sodium from the glass substrates can also contribute in diffusion during the annealing steps and serves as a shallow acceptor in CdTe with a low activation energy of 59 meV and can lower the space charge width and also increase the grain boundaries resulting in decreased efficiencies.[53]

2.4 Perovskite Solar Cell Design

The perovskite solar cell (PSC) has been an exciting addition to solar research in the last several years with its low temperature synthesis, efficiencies exceeding 22%, and flexible device capabilities. With efficiencies already exceeding 22%[15], PSC performance is already comparable to that of the state-of-the-art copper indium gallium diselenide (CIGS) solar cells and is approaching commercial monocrystalline silicon solar cells.[54] Adding to this excitement is the vast number of manufacturing techniques that have been utilized to create these devices and the large number of complementary materials that can be used to produce several different architectures.

The organic perovskite material used in PSCs was first introduced in 1978 when Poglitsch and Weber replaced the cesium ion in the $CsPbX_3$ (X = Cl, Br or I) with the methylammonium cation ($CH_3NH_3^+$).[55] Research continued in the 1990s when IBM published several papers on the materials including tin based perovskites and a paper involving the sequential deposition of the precursors to form perovskite materials.[56-57] IBM was investigating perovskites as attractive candidates for emitter materials in electroluminescent devices. At the time, they were not considered as a possible solar cell material. Later in 2009, Miyasaka et al. used the perovskite for the first time as part of a dye-sensizited solar cell.[58] The breakthrough came in 2012 when Miyasaka teamed up with

Snaith et al. and created the first PSC exhibiting an efficiency of over 10%.[59] Since its inception, the perovskite has reached efficiencies exceeding 22%.

2.4.1 The Instability of PSCs Background

The perovskite solar cell is best described as a p-i-n device **(Figure 2.4)**. The perovskite material is capable of transporting both holes and electrons so it is modeled as an intrinsic semiconductor (i). Holes are injected into the hole transport layer (p) attached to one side of the perovskite layer while electrons are injected into the electron transport layer (n) situated on the opposite side of the device. The devices are generally fabricated on transparent conductive materials such as fluorinated tin oxide (FTO) glass or on indium tin oxide (ITO) polymer substrates and use a metal such as gold for the second contact. The instability of the PSC can originate in any one or several of these layers.
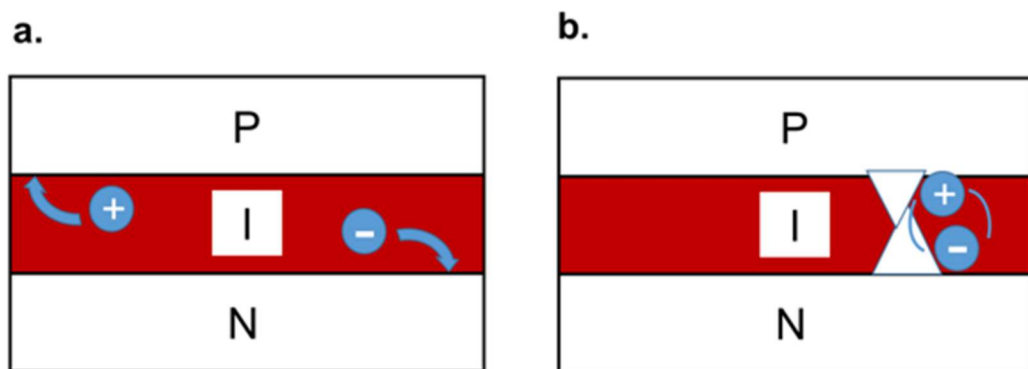
Figure 2.4. Illustration of charge transfer in high efficiency perovskite solar cell from intrinsic perovskite layer (i) to p-type hole transport layer (p) and n-type electron transport layer (n). **b.** Illustration of recombination occurring as the intrinsic perovskite layer (i) is no longer separating the p-type hole transport layer (p) and n-type electron transport layer (n).

2.4.2 Electron transport materials

Table 2.1. Highest performing devices using low temperature electron transport material (ETM) processing and best overall performing devices regardless of processing conditions

Material	Low Temperature (< 200 C) Efficiency			Highest Efficiency Devices		
	Temp	Area	Efficiency	Temp	Area	Efficiency
TiO_2	150 °C	0.108 cm^2	17.35%[60]	450 °C	0.16 cm^2	21.6%[61]
SnO_2	180 °C	0.16 cm^2	20.8%[62]	180 °C	0.16 cm^2	20.8%[62]
ZnO	70 °C	0.071 cm^2	15.7%[63]	250 °C	0.12 cm^2	16.1%[64]
Carbon Fullerenes	150 °C	0.096 cm^2	18.1%[65]	150 °C	0.096 cm^2	18.1%[65]
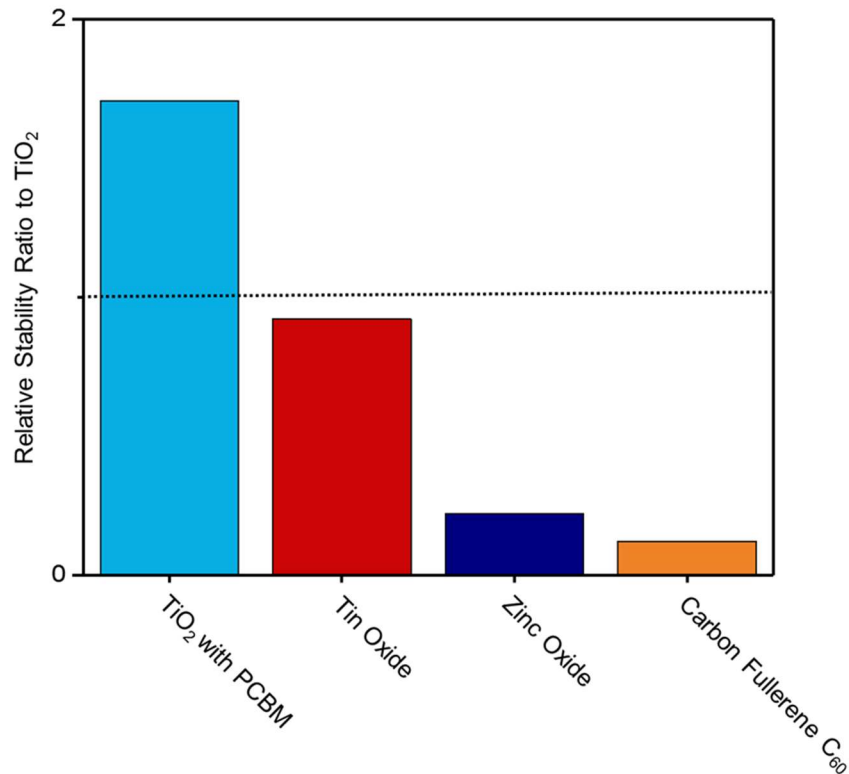
Figure 2.5. Relative stabilities of some of the most common electron transport materials compared to titanium dioxide [60, 62, 66-68]

Titanium dioxide (TiO_2) is currently one of the most popular choices as an electron transport material (ETM) in PSCs and has a history dating back to the dye-sensitized solar cell. Because of this and the wide variety of stability testing conditions with variabilities in humidity, illumination, and temperature, the stability of the ETM discussed in **Figure 2.5** will only come from experiments in which a TiO_2 PSC was used as reference. The relative stability ratio (RSR) in **Figure 2.5** is defined as:

$$RSR = \frac{\% \text{ of the initial efficiency of PSCs made with the specified ETM after stability testing}}{\% \text{ of the initial efficiency of the reference } TiO_2 \text{ PSC after humidity testing}}$$

In scenarios in which one of the devices degraded to nonworking conditions, the devices were compared at the half-life of the least stable device. Devices made using TiO_2

hold the highest efficiency (21.6%) published in a scientific journal for single junction cells.[61] Despite impressive efficiencies, there is concern of UV-initiated TiO_2 superoxide formation that causes deterioration in device performance. Leijtens et al. reported that TiO_2 PSCs encapsulated in a nitrogen atmosphere suffer from an extremely rapid (30min half-life) decay in photocurrent and performance under simulated sunlight with the full UV component present.[69] When a UV cutoff was used in their tests, cells decayed to only 85% of their initial performance within the 5 h. Transient absorption spectroscopy (TAS) and photocurrent extraction measurements suggested the UV-degraded cells suffered from deep trapping of injected electrons within newly available sites in the TiO_2. While photoinduced electron transfer to TiO_2 and hole transfer to spiro-OMeTAD were largely unaffected, a large fraction of the electrons injected into TiO_2 were trapped in deep trap sites where they eventually recombined with holes in the spiro-OMeTAD. The mechanism was described in four steps: (1) UV light caused photogenerated holes to react with the oxygen radicals adsorbed at surface oxygen vacancies on the TiO_2 (2) The molecular oxygen desorbed from these sites, leaving unoccupied, deep surface trap sites and a free electron per site (3) The newly formed electrons then recombined with excess holes in the doped-hole transporter (4) Upon photo excitation of the PSC, electrons are trapped after being injected into the conduction band or go directly into the deep surface trap states where they are immobile and recombine readily with holes in the hole transport material.[69]

Besides stability concerns, another problematic issue of using TiO_2 as an electron transport material is the necessity of a mesoporous layer. This requires an extra step in a manufacturing process. Ideally, PSCs will have a planar structure that requires only one processing step for the ETM. This has been challenging to achieve as TiO_2 planar devices

suffer from low efficiencies and noticeable hysteresis.[70-72] To eliminate the hysteresis, Baena et al. used tin oxide (SnO_2) for planar devices with its more favorable conduction band alignment to the conduction bands of the perovskite materials compared to the larger energy mismatch with the conduction band of TiO_2. The conduction band of $MAPbI_3$ is about 80 meV below that of TiO_2 and about 170 meV above that of SnO_2. This inhibits electron extraction to the TiO_2 in comparison to SnO_2.[73] In addition, bulk SnO_2 with an electron mobility of $240\ cm^2\ V^{-1}\ s^{-1}$ is over 100 times more conductive than TiO_2.[74] Another added benefit in the research was the relatively low processing temperature (120 °C)[73] for SnO_2 devices made with atomic layer deposition (ALD) and 180 °C for SnO_2 devices made using sol-gel spin coating[75] which enables future processing on cost-effective flexible substrates. Anaraki et al. improved the SnO_2 planar device efficiency to 20.8% and enhanced the processing capabilities by using a more scalable wet chemistry approach compared to ALD.[62] Two processing methods were tested to create the 30 nm SnO_2 layers. The first used spin coating of $SnCl_4$ precursor solution in isopropyl alcohol, as shown by Ke et al.[76] The second method added a chemical bath deposition (CBD) as a post treatment after the spin-coating to improve the conformity and blocking capabilities of the SnO_2. The CBD was based on past research by Zhang et al.[77] and was previously used to create SnO_2 blocking layers for PSCs with voltages of over 1.2V containing high fill factors. This approached the maximum thermodynamic voltage of 1.32V.[78-79] The method used $SnCl_2*2H_2O$, urea, and deionized water with the addition of mercaptoacetic acid and hydrochloric acid as precursors. The SnO_2 produced by spin-coating with CBD produced higher efficiencies than the ALD deposited SnO_2 likely from a higher roughness that allowed increased contact of the SnO_2 with the perovskite material during processing.

Another benefit of the work was increased reproducibility compared to the ALD coated devices.[62]

Although SnO_2 is an excellent candidate for planar devices, its durability still falls short of mesoporous TiO_2 devices. Roose et al. created mesoporous SnO_2 cells and showed improved durability under UV illumination compared to mesoporous TiO_2 and planar SnO_2 devices.[80] One complication occurred during the annealing of the SnO_2 mesoporous layer in which fluorine migrated from the FTO slides into SnO_2 mesoporous layer and posed a serious problem that limited device efficiencies below that of the mesoporous TiO_2 and planar SnO_2 devices. The fluorine doped the SnO_2 to an extent in which charge selectivity was compromised and recombination was increased. Switching to aluminum doped zinc oxide (AZO) glass slides increased device efficiencies from 8.7% to 11.6%. After 10 hours of testing under UV conditions, the mesoporous SnO_2 retained $\approx$ 98% of its starting efficiency compared to $\approx$ 87% for mesoporous TiO_2 and $\approx$ 89% for planar SnO_2.[80] It's important to note that the mesoporous devices plateaued in device efficiencies while the planar SnO_2 devices continued to steadily decrease in efficiency after 10 hours. The mesoporous network has been reported to provide mechanical and chemical stability to the PSCs, inhibiting the penetration of harmful substances such as moisture, oxygen, or gold into the perovskite layer.[66, 81] Unfortunately even after implementing AZO and being treated in a UV environment, the mesoporous SnO_2 devices still had inferior efficiencies (10.4%) compared to the mesoporous TiO_2 devices (13%).[80]

The other primary oxide being considered as an ETM is zinc oxide (ZnO). Like tin oxide, the conductivity of ZnO is superior to that of titanium dioxide and it can be processed at lower temperatures in many different microstructures.[82-84] Kelly et al. were

able to create a planar zinc oxide device with an efficiency of 15.7% without needing any high temperature sintering steps.[63] Dong et al. also successfully prepared 13.1% efficiency ZnO devices at low temperatures (70 C) using ALD.[85] Interestingly the perovskite precursors lead chloride (PbCl) and MAI reacted at room temperature within a few minutes without the need of a thermal treatment which would be advantageous in manufacturing. This was due to the reaction between CH_3NH_3Cl and ZnO. At room temperatures, reaction (1) is energetically favorable but its rate is very slow. However if the byproduct of this reaction, CH_3NH_3Cl, is depleted, then reaction (1) will be accelerated.[86] This was easily seen by a color change in the perovskite film on the ALD-ZnO, so it was speculated that the ZnO reacted with CH_3NH_3Cl, as shown in reaction (2). Energy dispersive spectra (EDS) measurements were used to confirm a large number of chloride ions, suggesting the existence of $ZnCl_2$. Oddly, reaction (2) did not happen for the solution prepared ZnO films. The difference between ALD-ZnO and solution prepared ZnO is the larger number of oxygen vacancies in ALD-ZnO.[87] The oxygen vacancies in ALD-ZnO enhanced its reaction activity, shown previously in the photocatalytic field.[87] In the perovskite reaction, the oxygen vacancies promoted the reaction of ZnO and CH_3NH_3Cl. Of the products of reaction (2), CH_3NH_2 is in the gas phase and H_2O is absorbed by $ZnCl_2$ because $ZnCl_2$ is extremely deliquescent in air (reaction (3)). The $ZnCl_2$ prevented the H_2O from decomposing the $CH_3NH_3PbI_3$.[85] →

$$3 \ CH_3NH_3I + PbCl_2 \rightarrow CH_3NH_3PbI_3 + 2 \ CH_3NH_3Cl \qquad (1)$$

$$2 \ CH_3NH_3Cl + ZnO \rightarrow 2 \ CH_3NH_2 + ZnCl_2 + H_2O \qquad (2)$$

$$ZnCl_2 + H_2O \rightarrow H[ZnCl_2(OH)] \qquad (3)$$
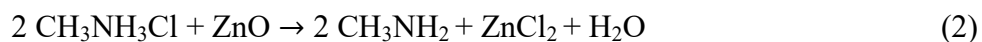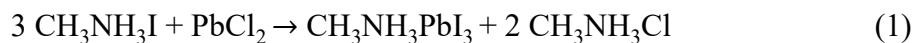
The ZnO based devices achieved 16% efficiency when Mahmood et al. created electron-rich, nitrogen-doped ZnO (N:ZnO) nanorods (NR) with enhanced electron mobility produced using ammonium acetate.[64] Polyethyleneimine (PEI) was used as a dipole layer and a selective polymer capping layer to synergistically promote the formation of high aspect ratio (HAR) electron-rich nitrogen-doped ZnO NRs with reduced work functions suitable for use as ETM in highly efficient mesostructured perovskite solar cells. The high aspect ratio ZnO nanorods improved efficiencies from 10 to 16.1% with decreased hysteresis and stabilized efficiencies.[64] The length of the nanorods was controlled by the growth time. Growth times of 60, 90, and 120 min produced nanorods with lengths of 575 nm, 750 nm, and 1070 nm respectively. Meanwhile, the diameter of the rods was set by the precursor concentration. The 1070 nm long nitrogen-doped ZnO NRs performed with the highest efficiency. Nanorods grown to 1410 nm decreased in efficiency. The nitrogen doping increased the short circuit current and efficiency by increasing the electron density.[88] The increase in open circuit voltage (from 926 to 958.5 mV) after doping was attributed to an increase in the Fermi energy levels, owing to the increase in the charge-carrier density, which broadened the direct optical bandgap and lowered the barrier to electron transfer.[89] It could have also increased due to reduced recombination losses as a result of improved electron-transport properties within the NRs.[88]

The problem facing ZnO devices is their instability attributed to the presence of surface hydroxyl groups and/or acetate ligands, as well as the higher basicity of ZnO, which deprotonates the MAI cation and degrades perovskites.[90-91] Another issue facing ZnO adoption is its weak thermal stability. Without sufficient annealing, perovskite films grown on ZnO contain smaller grain sizes compared to perovskite films grown on TiO_2, and

produce lower efficiencies.[67] Shown in **Figure 2.5**, ZnO is currently the least stable among the most popular ETM for PSCs.

Outside of the oxides, carbon fullerenes like phenyl-C_{61}-butyric acid methyl ester (PCBM) have been used as electron transport materials. PCBM is more conductive than TiO_2 and its lowest unoccupied molecular orbital (LUMO) (-3.9 eV) is well aligned with the LUMO level of $CH_3NH_3PbI_3$ perovskite (-3.93 eV).[92-94] Accordingly, when a fullerene like PCBM or C_{60} is in contact with $CH_3NH_3PbI_3$, PCBM with a LUMO of –4.0 eV and C60 with a LUMO of -4.5 eV have small mismatches in energy and could be ideal "electron acceptors" for perovskites.[95] Heo et al. achieved a high efficiency of 18.1% using PCBM as the ETM.[65]

The best ETM may be a combination of the materials previously mentioned. The surface of TiO_2 films have been modified using a self-assembled monolayer (SAM) of fullerene derivatives to create higher device stabilities against UV illumination.[60] The problem with this approach is the deposition of a SAM layer usually takes more than 10 h for the molecular anchoring, and is not convenient for industrial manufacturing. Li et al. modified the TiO_2 layer by depositing a triblock fullerene derivative [6,6]-phenyl-C61-butyric acid-dioctyl-3,3′-(5-hydroxy-1,3-phenylene)-bis(2-cyanoacry-late) ester (PCBB-2CN-2C8) as a modification layer on the TiO_2.[60] The derivative used electron-deficient cyano-groups to pacify the oxygen vacancies that plague TiO_2 devices. Lewis base groups like -CN and -SCN have been proven to occupy the oxygen vacancies (or Ti^{3+} sites), and thus to pacify oxygen vacancies.[96] To minimize its solubility in polar solvents and not deteriorate during perovskite deposition, dioctyloxy chains and cyano-groups were added to make it highly soluble in nonpolar solvents. In addition, PCBB-2CN-2C8 was

engineered to have a high thermal stability with a decomposition temperature of 356 °C. These stability improvements made the composite the most stable of the ETM analyzed in this review. The composite also increased the efficiency (17.35%) of planar low temperature fabricated (150 °C) TiO_2 devices with minimal hysteresis (hysteresis index of 0.052) enabling manufacturing on plastic substrates.[60]

2.4.3 Perovskite materials

Table 2.2 Highest performing solar cells based on different perovskite systems

Material	Band gap (eV)	Area	Efficiency
Tin Perovskites	1.3-2.15	$0.12\ cm^2$	6.4%[19]
Lead Perovskites	1.48- 2.28	$0.16\ cm^2$	21.1%[97]
Lead and Tin Hybrid Perovskites	1.3-2.28	$0.07 cm^2$	21.7%[98]
Germanium Perovskites	1.6-3.1	unknown	3.2%[99]
Copper Perovskites	1.8-2.5	$0.2\ cm^2$	0.2%[100]
2-D Lead Perovskites	1.6-2.2	$0.5\ cm^2$	12.51%[101]

2.4.3.1 Degradation Pathways

In PSCs, the perovskite layer is typically the least thermally stable so low temperature processing is not an issue compared to the ETM and HTM. Progress has been made to increase the durability of this layer but PSCs are still susceptible to water degradation and oxygen. The generally accepted water degradation[102] for $CH_3NH_3PbI_3$ is as follows:

$$CH_3NH_3PbI_3(s) \rightarrow CH_3NH_2(g) + HI(g) + PbI_2(s) \qquad (4)$$
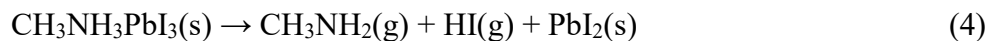
The reaction begins when water deprotonates $CH_3NH_3^+$ resulting in several degradation products. After this step, there still could be many unknown intermediate steps. Intense

research is ongoing to determine these missing steps. The formation of oxides and carbonates like $PbCO_3$, and PbO can occur alongside PbI_2.[103] They form at different rates than from purified PbI_2, suggesting compounds other than stoichiometric PbI_2 may serve as decomposition intermediates.[104] Hydrate complexes can also form with $CH_3NH_3PbI_3$ like $CH_3NH_3PbI_3H_2O$, or $(CH_3NH_3)_4PbI_6*2H_2O$ as shown in the equations below[105-106]:

$$4CH_3NH_3PbI_3 + 4H_2O \leftrightarrow 4[CH_3NH_3PbI_3 \cdot H_2O] \tag{5}$$

$$4CH_3NH_3PbI_3 + 4H_2O \leftrightarrow (CH_3NH_3)4PbI_6 \cdot 2H_2O + 3PbI_2 + 2H_2O \tag{6}$$
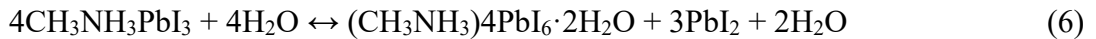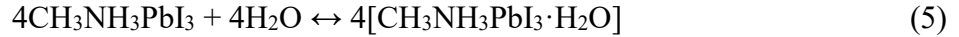
Oxygen radicals are another source of possible degradation to the perovskite layer in the PSC. The reaction (equations 7-9) begins when photoexcited perovskite containing both electrons and holes (MAPbI3*) transfers an electron to molecular oxygen and forms a superoxide $O_2{}^{\cdot-}$. Next the superoxide breaks down the perovskite by first deprotonating the MAI, leading to the formation of PbI_2, iodine, and water as by-products. The resulting water can then participate in further degradation pathways such as the hydrate formations mentioned earlier.[91, 107] Aristidou et al. showed that $CH_3NH_3PbI_3$ films rapidly degrade (e.g., on a timescale of a few hours to days) when exposed to both light and oxygen.[108-109] This could have a significant impact on the future processing capabilities of the PSC.

$$MAPbI_3 \xrightarrow[\text{No moisture}]{\text{Light}} MAPbI_3{}^* \tag{7}$$

$$O_2 \xrightarrow{MAPbI_3{}^*} O_2^{\bullet-} \tag{8}$$

$$MAPbI_3 + O_2^{\bullet-} \xrightarrow{\text{Deprotonation}} MeNH_2 + PbI_2 + 1/2 I_2 + H_2O \tag{9}$$
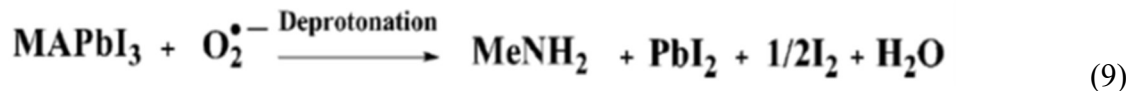
While there are still many degradation issues that need to be addressed in the PSC, there have been several manufacturing and formulation improvements to increase the efficiency,

durability, reproducibility, and uniformity of perovskite films.

2.4.3.2 Halide Substitution

Halide substitutions in the MAPbI$_3$ perovskites have resulted in CH$_3$NH$_3$PBI$_3$, CH$_3$NH$_3$Br$_3$, CH$_3$NH$_3$Cl$_3$ and mixtures of these halides. Varying the amount of bromine has created broad spectrums of colors and band gap tuning from 1.58 eV to 2.28 eV.[110-111] Substituting bromine for iodide increases the conduction band edge minimum and results in open circuit voltages (V$_{oc}$s) as high as 1.5V.[110-111] For formamidinium perovskites the band gap tuning is between 1.48eV to 2.23 eV, and for tin-based devices the band gap tuning ranges from 1.3 eV to 2.15 eV.[17, 19] The highest conversion efficiencies seen thus far for bromine based perovskites without iodine (10.45%) were achieved by Heo et al. by using a solvent-engineering method in which HBr was added to DMF to slow the crystallization process and decrease the evaporation rate. [112]

Adding chlorine to the perovskite structure has also been investigated by several groups, however so far only small amounts of the ion have been successfully added to the structure and the resulting changes on the optical and structural properties are not clearly discernable.[113] Conversely, the electronic property enhancements are well documented, showing increased charge transport and reductions in recombination rates. [114-115]

Substituting either bromine or chlorine encourages cubic structure formation as opposed to the tetragonal formation commonly seen in CH$_3$NH$_3$PbI$_3$. This is due to decreasing the size of the halogen ion from 2.2 Å for I, to 1.96 Å for Br, and 1.81 Å for Cl.[55, 116] Despite cubic perovskite structures having theoretically more enhanced light absorption and electrical properties, their larger band gaps absorb less of the solar spectrum and generate lower power conversion efficiencies. [117]

2.4.3.3 Lead precursors

Zhang et al. studied the lead iodide, lead chloride, and lead acetate growth kinetics with x-ray diffraction (XRD) and revealed faster growth kinetics depended on the choice of lead precursor ($PbAc_2 >> PbCl_2 > PbI_2$). Lead acetate films formed in 2.5 minutes, lead chloride in 10 minutes, and lead iodide in 43.8 minutes.[118] Meanwhile analysis using the Scherrer equation revealed the faster lead acetate kinetics created smaller crystal sizes (>500nm ($PbCl_2$), 305±65 (PbI_2), and 135±45nm ($PbAc_2$). The reason for the faster kinetics of the acetate system are believed to be from the CH_3NH_3Ac byproduct which is unstable and easier to remove than the excess CH_3NH_3Cl and CH_3NH_3I. Thermal gravimetric analysis (TGA) supported this theory: the initial decomposition temperature (defined by T at 95% weight) was 97.4 °C, 226.7 °C, and 245.0 °C for CH_3NH_3Ac, CH_3NH_3Cl and CH_3NH_3I, respectively.[118] The lead acetate precursor created an enhanced morphology and full coverage of the perovskite layer with no discernable pinholes. Enhanced morphology correlated to higher efficiencies. The average PCE with optimized annealing times for perovskites from $PbCl_2$, PbI_2 and $PbAc_2$ routes was 12.0%, 9.3% and 14.0%, respectively.[118]

2.4.3.4 Metal substitution

Lead is a toxic substance so it would help in the manufacturing of PSCs to use another metal. Thus far, tin has remained the most popular metal to substitute for lead. Tin-based perovskites exhibit good electrical properties but their affinity towards the +4 oxidation state when exposed to air rather than the +2 oxidation state needed for perovskite formation has presented many complications. The highest efficiency to date is 6.4% [19] for an all tin device, and 7.37% for the lead containing $CH_3NH_3Sn_{0.25}Pb_{0.75}I_3$.[119] The low photocurrent

densities have been ascribed to poor perovskite film coverage on TiO_2 and the previously mentioned oxidation problem of Sn^{2+} ions ascribed as the cause of low open-circuit voltage. [119] Another problem for tin-based devices is their low charge diffusion length of 30 nm; limiting device performance. [120] Tin based devices improved with incorporation of chlorine atoms to 10.1% efficiency in the $CH_3NH_3Sn_aPb_{1-a}I_{3-x}Cl_x$ planar device. [121] Zhu et al. improved this efficiency to 15.2% by controlling the film formation by introducing DMSO as a solvent. [122] To make the tin more stable in the 2+ oxidation state, SnF_2 and cesium substitution for $CH_3NH_3^+$ have had moderate success at suppressing the +4 oxidation state. [123] Cesium incorporated tin perovskites $CsSnI_3$ are p-type with band gaps around 1.3eV and efficiencies of 1.67%. [124] The stability of the $CH_3NH_3SnI_3$ PSC can be protected by proper sealing. After sealing with surlyn films, Kanatzidis et. al discovered their tin perovskite devices retained almost 80% of the initial performance in the first 12 h. Performance loss was mainly caused from the decrease in photocurrent density and FF, primarily due to the p-type doping via Sn^{2+} oxidation induced during the fabrication process. [19] Bromine incorporated cesium tin perovskites yield higher open circuit voltages by widening the band gap akin to their lead counterparts. [124]

Another possible metal replacement for lead is germanium. Cesium containing germanium perovskites $CsGeX_3$ have a rhombohedral structure and R3m symmetry. [125-126] They are beginning to attract attention with a maximum efficiency of 3.2%. [99] Band gaps of 1.6, 2.3, and 3.1 suggest these structures have higher efficiency potentials. [99] Other metals commonly suggested are the transition metals: Cu, Mn, Fe, Co, and Ni. Transition metal perovskites like K_2NiF_4 tend to form layered structures resulting from smaller ionic radii leading to steric hindrance to the 3D structure. [127] These layered "Ruddlesden-Popper"

phase structures were also evident in the copper containing perovskite $(CH_3NH_3)_2CuCl_{4-x}Br_x$.[99] The incorporation of the Cl ion was necessary to prevent the reduction of Cu^{2+}. Copper perovskite solar cells are relatively new with maximum efficiencies of only 0.02%. Lowered efficiencies come from the partial reduction of Cu^{2+} caused by bromine which causes anion vacancies acting as electron traps.[99]

2.4.3.5 Organic cation substitution

PSCs have also benefited from the substitution of the organic cation. The main organic cations studied to date have been methylammonium $CH_3NH_3^+$ and formamidinium $(HC(NH_2)_2^+)$. Formamidinium-based devices have achieved the highest efficiencies and are preferable as they are less sensitive to temperature degradation than methylammonium-based perovskites. Formamidinium does not show thermal degradation in air at 150 °C whereas methylammonium discolors after 30 minutes.[17]

The allowed organic cation substitutions can be predicted using the Goldschmidt tolerance factor.[128] The tolerance factor is based on the size of the perovskite's constituents. Formamidinium lead perovskites have a tolerance factor of 0.99 which is higher than methylammonium lead perovskites which have a tolerance factor of 0.91. Ideally the cubic phase has a tolerance factor of 1. The perovskite lattice expands as the size of the cation expands; causing for a decrease of the band gap. Although formamidinium has a more ideal band gap of 1.48 as opposed to 1.55, early attempts to make this structure suffered from the yellow polymorth non-perovskite formamidinium structure. Efficiencies improved when higher annealing temperatures were used and transitioned the yellow polymorth to the preferred black structure.[129] Another advantage for formamidinium is the lack of a phase transition at 57 °C that plagued the methylammonium perovskites. A higher power

conversion efficiency (14.9%) was reached by mixing the two cations.[130] In the lead bromide perovskites, formamidinium exhibited longer PL lifetimes and larger charge diffusion length 200 ns vs. 17 ns for methyl containing perovskites.[131]

Another cation used was ethylammonium, however its efficiencies were much lower than that of formamidinium and methylammonium.[132] Future options predicted by the Goldschmidt tolerance factor include hydroxylammonium $[H_3NOH]^+$, hydrazinium $[H_3N-NH_2]^+$, azetidinium $[(CH_2)_3NH_2]^+$, imidazolium $[C_3N_2H^5]$ + and guanidinium $[C(NH_2)^3]^+$.[133] These cations are predicted to form cubic perovskites.[132]

Inorganic cations are another option in perovskite solar cells. Concerns over the low decomposition temperatures (150-200°C) of organic cation based perovskites have sparked the study of using inorganic materials such as cesium. Cesium lead iodide perovskite cells have reached efficiencies of 2.9% for planar and 1.7% for mesoporous structure.[134] Efficiencies for cesium lead iodide perovskites are plagued by a nonideal 1.73 eV band gap and the material decomposing to its yellow orthorhombic non-perovskite structure at room temperature. Eperon et al. discovered that adding hydroiodic acid (HI) can help to stabilize $CsPbI_3$ at lower temperatures.[134]

2.4.3.6 Mixing of Organic Cations, Halides, and Metals

Lately the most efficient solar cells have used mixtures of inorganic cations with organic cations and a variety of different halides. This became highlighted by Gratzel et al. when they studied cesium containing triple cation perovskites. The group created solar cells with efficiencies >21% using $Cs_{0.05}(MA_{0.17}FA_{0.83})_{0.95}Pb(I_{0.83}Br_{0.17})_3$.[97] Cesium was effective in assisting the black phase of formamidinium perovskites due to entropic stabilization.[135] Methylammonium is also able to push formamidinium into the preferred

black perovskite phase but at a much slower rate. The cesium containing "triple cation" perovskites had greater reproducibility than mixtures of methylammonium and formamidinium alone. Gratzel et al. reported that this was likely due to the extreme temperature sensitivity of the crystallization process for formamidinium and methylammonium based devices. In comparison, the triple cation perovskites were more robust and showed a greater potential to be manufactured under a variety of temperatures. At full illumination of over 250 hours, the triple cation devices maintained an efficiency of over 18% meanwhile those lacking cesium fell to below 10% after 50 hours.[97] Saliba et al. later introduced the rubidium ion into the cesium, MAI, FAI based perovskite. After adding 5% rubidium, an efficiency of 20.6% was achieved from the PSC with a band gap of 1.63 eV.[61] The devices were aged for 500 hours at 85°C under continuous illumination with full solar intensity and maximum power point tracking in a nitrogen atmosphere and retained 95% of their initial performance.[61]

The available band gap tuning ability of the PSC has generated interest in creating graded band gap solar cells. Unlike tandem devices that require complex electrical coupling and interconnections between the perovskite sub-cells; generating electron–hole recombination centers, graded band gap solar cells utilize impact ionization to generate current from multiple band gaps within a single cell design.[13, 98] Ergen et al. fabricated $CH_3NH_3SnI_3$ and $CH_3NH_3PbI_{3-x}Br_x$ on plasma-etched GaN to achieve unsteady state efficiencies of nearly 26% and stabilized efficiencies of 21.7%.[98] The tin perovskite in the first layer provided a narrow bandgap in the 1.2 eV to 1.5 eV range.[19, 57, 136-139] Replacing tin with lead in the second layer facilitates a larger bandgap between 1.5 eV to 2.2 eV by varying halide composition.[20, 140-142]

2.4.3.7 Layered 2-D Perovskites

In the 3-D perovskite, the anionic MX_6 octahedra are condensed into a three-dimensional network; however, the size of the cation plays a critical role in determining the thickness and separation of the inorganic layers: if the cation size is too large, it cannot fit into the rigid 3-D perovskite network and, thus, separates the system into layers, forming lower dimensional networks due to steric effects. [143] These layered 2-D halide perovskites take the generic structural formula of $(A)_2(CH_3NH_3)_{n-1}MX_{3n+1}$ (n is an integer), where A is a primary aliphatic or aromatic alkylammonium cation, M is a divalent metal, and X is a halide anion. The 2D network consists of inorganic layers of corner-sharing $[MX_6]^{4-}$ octahedra confined between interdigitating bilayers of intercalated bulky alkylammonium cations.[143] They are known to have two orientations: $\langle 110 \rangle$ or $\langle 100 \rangle$. 2D perovskites possess higher exciton binding energies and poor conductivity in certain crystallographic directions along with less ideal higher band gaps.[144]

The 2D perovskite $(PEA)_2(MA)_2[Pb_3I_{10}]$, (with PEA $(C_6H_5(CH_2)_2NH_3^+)$ and MA $(CH_3NH_3^+)$) as a photovoltaic absorber yielded power conversion efficiencies close to 5%.[145] Using the n-butylammonium compound, a power conversion efficiency of 4.02% was obtained by using $(CH_3(CH_2)_3NH_3)_2(CH_3NH_3)_2Pb_3I_{10}$ as a light absorber, with an open-circuit voltage (V_{oc}) of 929 mV and a short-circuit current (J_{sc}) of 9.42 mA/cm^2.[143] Losses in efficiency are likely a result of poor heterojunction energy band alignment. As more n-butylammonium is substituted into the perovskite, the valence and conduction bands increase in energy and become less ideal in relation to the conventional electron and hole transport materials TiO_2 and Spiro-OMeTAD respectively.[143] A breakthrough in 2D perovskites occurred in 2016, when Tsai et al. created 2D $(BA)_2(MA)_3Pb_4I_{13}$ (BA referring

to n-butylammonium) PSCs with 12.51% efficiency.[101] The films were deposited using a hot casting technique to improve the crystallinity of the films, and produced a textured polycrystalline film in which the crystal domains were oriented with their (101) planes parallel to the substrate surface unlike the room temperature deposited films that contained considerable randomness in the 3D orientation of the crystal domains (grains) within the polycrystalline film. Not only were higher efficiencies obtained, but the stability of the encapsulated cells showed no discernable degradation or hysteresis after constant illumination and 65% humidity for over 2,250 hours of testing. Under the same conditions and encapsulation, the 3D device degraded to 50% of its initial efficiency within the first 10 hours.[101]

2.4.4 Hole transport materials

Table 2.3 Highest performing devices using low temperature hole transport material (HTM) processing and best overall performing devices regardless of processing conditions

Materials	Low Temperature (<200 C) Efficiency			Highest Efficiency		
	Temp	Area	Efficiency	Temp	Area	Efficiency
OMeTPA-FA	Room Temp	N/A	13.63%[146]	Room Temp	unknown	13.63%[146]
PEDOT:PSS (Including Doped)	150 °C	0.096 cm^2	18.1%[65]	150 °C	0.096 cm^2	18.1%[65]
P3HT with carbon nanotubes	Room Temp	0.063 cm^2	15.3%[147]	Room Temp	0.063 cm^2	15.3%[147]
Cu$_2$O	Room Temp	N/A	8.93%[148]	250 °C	0.04 cm^2	13.35%[149]
CuSCN	Room Temp	0.1 cm^2	16.6%[150]	Room Temp	0.1 cm^2	16.6%[150]
CuI	100 °C	0.06 cm^2	13.58%[151]	100 °C	0.06 cm^2	13.58[151]
Nickel Oxide (Including Doped)	200 °C	0.04 cm^2	17.3%[152]	200 °C	0.04 cm^2	17.3%[152]
H101	70 °C	0.2 cm^2	13.8%[153]	70 °C	0.2 cm^2	13.8%[153]
C-12 Carbazole	Room Temp	N/A	11.26%[154]	Room Temp	N/A	11.26%[154]
EDOT-OMeTPA	Room Temp	0.08 cm^2	11.0%[155]	Room Temp	0.08 cm^2	11.0%[155]
CzPAF-SBF	Room Temp	0.11 cm^2	17.03%[156]	Room Temp	0.11 cm^2	17.03%[156]
Carbon	50 °C	0.10 cm^2	12.67%[157]	50 °C	0.10 cm^2	12.67%[157]
Polythiophene	Room Temp	N/A	16.5%[158]	Room Temp	N/A	16.5%[158]
No HTM	100 °C	0.08 cm^2	11.1%[159]	100 °C	0.08 cm^2	11.1%[159]
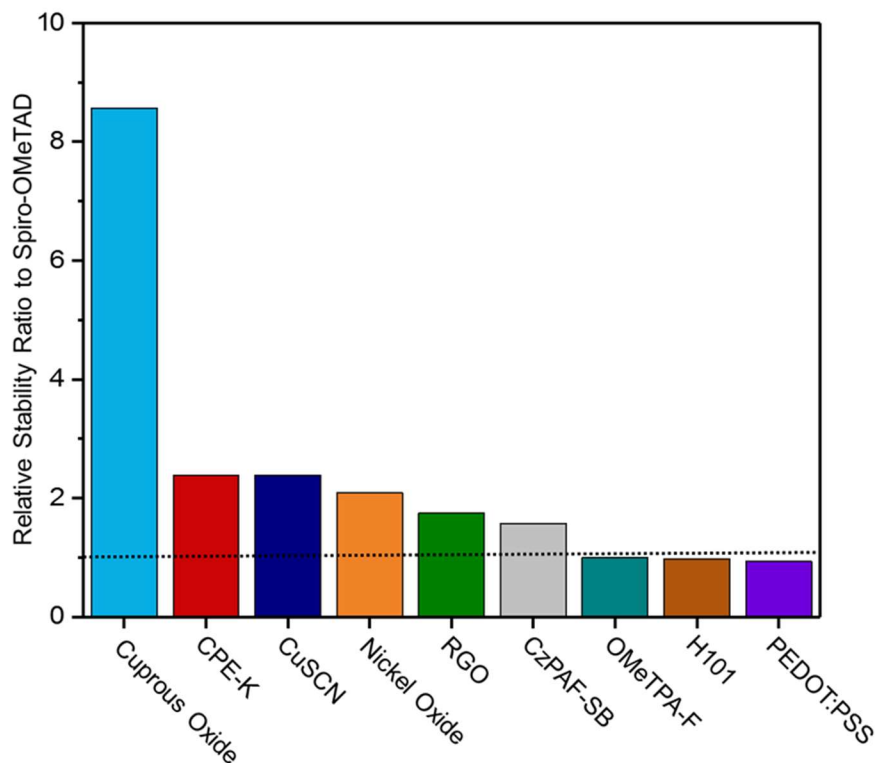
Figure 2.6. Relative stabilities of some of the most common hole transport materials compared to Spiro-OMeTAD [146, 148, 153, 156, 160-164]

The current commercial price of high purity Spiro-OMeTAD is over ten times that of gold and platinum. State-of-the-art devices using this hole transport material (HTM) would add around $40/m^2 to the photovoltaic devices.[155] It is unlikely this price will decrease to an economical level due to the multi-step synthetic methods and high purity needed for photovoltaic applications.[146] In addition, it is known that spiro-OMeTAD causes degradation of the perovskite layer.[165] This is unsurprising as similar results were found with the Dye-Sensitized solar cell.[166-167] Mainly, the issues surrounding the degradation are due to thermal stress effects and oxidation.[168] New HTMs will need to be developed to commercialize the PSC. The most studied of these alternative HTM are shown in **Table**

2.3 and discussed below. Again because of the wide variety of stability testing conditions with variabilities in humidity, illumination, and temperature, and the long history of devices made using spiro-OMeTAD, the stability of the HTMs discussed in **Figure 2.6** will only come from experiments in which a spiro-OMeTAD PSC was used as reference. The relative stability ratio (RSR) in **Figure 2.6** represents

$$RSR = \frac{\% \text{ of the initial efficiency of PSCs made with the HTM specified after stability testing}}{\% \text{ of the initial efficiency of the reference Spiro} - \text{OMeTAD PSC after humidity testing}}$$

In scenarios in which one of the devices degraded to nonworking conditions, the devices were compared at the half-life of the least stable device.

2.4.4.1 Conjugated Organics

In an effort to reduce the number of synthesis steps while maintaining the performance of Spiro-OMeTAD, 2,5-bis(4,4'-bis(methoxyphenyl)aminophen-4''-yl)-3,4-ethylene-dioxythiophene, known commonly as H101 was created.[153] H101 can be manufactured using 2 synthesis steps and produced a yield of 82% prior to any optimization of the process. It's glass transition temperature is also lower at 73 °C than Spiro-OMeTAD (125 °C), making it more suitable as a sealant for the perovskite layer.[153] To improve the material's conductivity and lower its HOMO level, H101 can be doped with tris(2-(1H-pyrazol-1-yl)pyridine)cobalt(III) (FK102). Undoped H101 obtained an efficiency of 10.6%, whereas H101 doped with FK102 reached a maximum of 13.8% efficiency. The stability of H101 was tested by heating prepared perovskite solar cells in a furnace at 70 °C for 7 days while noting the changes in efficiency of the cells. The short circuit current decreased and the overall efficiency suffered a 15% decrease during the 7 days. Spiro-OMeTAD was found to be <5% more durable than H101 during these tests.[153]

After H101 was created, Edot et. al. wanted to reduce the cost of the HTM and

synthesized EDOT-OMeTPA.[155] H101 still required the cross-coupling reactions that needed transition metal catalysts, inert reaction conditions and extensive product purification; making large-scale production cost-prohibitive. The material cost for EDOT-OMeTPA ($10/g) is about an order of magnitude lower compared to other conjugated organic HTMs.[155] To create EDOT-OMeTPA, Schiff base condensation reactions were utilized because of their less complex reactions, near atmospheric reaction conditions, and a favorable by-product of water.[169-174] With its all-aromatic backbone, EDOT-OMeTPA possessed a high thermal stability, with a 5% weight loss at 359 °C and a glass transition temperature of 105 °C.[155] In comparison, H101 had a glass transition temperature 32 °C lower, and spiro-OMeTAD had a glass transition temperature of 125 °C.[155] Resulting devices delivered a performance of 11.0% efficiency and only a decrease in 0.9% efficiency compared to devices made using the same procedure but with spiro-OMeTAD as the hole transport material. Testing of the devices showed a stability of over 1000 hours with less than 10% drop in efficiency when stored in 30% relative humidity. The disadvantage of using EDOT-OMeTPA is its reproducibility; larger spreads in efficiencies were seen in comparison to spiro-OMeTAD. These are likely attributed to pin hole formation and could be corrected with improved manufacturing.

Choi et al. went in a different direction when analyzing alternative HTMs and focused on creating cost-effective small molecule HTMs. Small molecular organic HTMs have high yields, high purities, defined molecular structures, and better batch-to-batch reproducibility. They created planar amine or star-shape triphenyl amine derivatives, coded as OMeTPA-FA and OMeTPA-TPA in an attempt to mimic the structural framework of N,N,N',N'-tetrakis(4-methoxyphenyl)benzidine (MeO-TPD), which was well recognized

as one of the best small molecule HTMs used in solid state dye-sensitized solar cells and organic light emitting diodes.[175-176] Fused quinolizino acridine was chosen as the core unit to increase the lifetime of the charge-separated state by the delocalization of the generated cation over a planar amine. The HOMO levels of OMeTPA-FA and OMeTPA-TPA are 5.15 and 5.13 eV; making it suitable for high charge separation and charge transfer at the interface in the mesoporous TiO_2/$MAPbI_3$/HTM junction. Despite a high efficiency of 13.63% for OMeTPA-FA based devices, both hole transport materials degraded faster than spiro-OMeTAD.[146]

Reddy et al. also wanted to explore inexpensive small molecule HTMs so they created: 7-(9,9′-spirobifluorene-2-yl)-N- (7-(9,9′-spirobifluorene-2-yl)-9,9-dioctyl-9H-fluoren-2-yl)-N- (4-(9H-carbazol-9-yl)phenyl)-9,9-dioctyl-9H-fluoren-2-amine (CzPAF-SBF) and 7-(7′-carbonitrile-9,9′-spirobifluorene-2-yl)- N-(7-(7′-carbonitrile-9,9′-spirobifluorene-2-yl)-9,9-dioctyl-9H- fluoren-2-yl)-N-(4-(9H-carbazol-9-yl)phenyl)-9,9-dioctyl-9H-fluoren-2-amine known as CzPAF-SBFN.[156] In CzPAF, the nitrogen atom serves as a linker between phenylcarbazole and fluorene groups to enhance hole mobility and solubility. Both small molecules possess triphenylamine, dioctylfluorene, and spirobifluorene as the core, spacer and end-caps, respectively which are common to hole transport materials such as PTAA, and spiro-OMeTAD. Despite its similar structure to spiro-OMeTAD, CzPAF-SBF and CzPAF-SBFN (≤$150 USD per gram) are more affordable than spiro-OMeTAD (≈$800 USD per gram). The extracted hole mobilities of pristine CzPAF-SBF and CzPAF-SBFN were 2.18×10^{-4} and 1.05×10^{-4} cm^2 V^{-1} s^{-1}, respectively, which are comparable to or higher than that of spiro-OMeTAD (1.80×10^{-4} cm2 V^{-1} s^{-1}). This impacted the overall efficiencies of the perovskite devices as CzPAF-

SBF (17.03%) had higher efficiencies than spiro-OMeTAD (16.45%), and CzPAF-SBFN (15.90%).[156] Stability tests of 500 hours in ambient conditions showed an improvement in stability for CzPAF-SBF (71% efficiency retention) vs. spiro-OMeTAD (45% efficiency retention). The larger water contact angle of 95.2° for CzPAF-SBF compared to that of spiro-OMeTAD (65.1°) helped to prevent moisture penetration into the perovskite layer.[156]

Research continued for easier to manufacture smaller molecular HTM as Lim et al. synthesized 8,16-didodecyl-8,16-dihydrobenzo[a]benzo[6,7] indolo[2,3-h]carbazole (C12-carbazole).[154] C12-carbzole PSCs achieved an increase in 1.64% efficiency compared to similarly fabricated cells using spiro-OMeTAD.[154] An added benefit of C12-carbazole is its relatively hydrophobic nature. Field effect transistors made of C12-carbazole were synthesized outside of a glove box and experienced no change in performance after 30 days in ambient conditions. Investigating it's electrical properties, C12-carbazole has a hole mobility of 1.5 cm^2 V^{-1} s^{-1} which is much larger than spiro-OMeTAD (5.31 x 10^{-5} cm^2 V^{-1} s^{-1}). [177]

Others sought inspiration from organic solar cell research and wanted to incorporate the popular PEDOT:PSS ((3,4-ethylenedioxythiophene):poly-styrene sulfonate) into the PSC as a replacement for the HTM. In the initial trials, PEDOT:PSS was discovered to be detrimental to device stability and longevity due to its acidic nature.[178] To create a more stable perovskite solar cell, 1.0 wt% MoO_3 was mixed with PEDOT:PSS to yield enhanced stability of the perovskite solar cell for over 250 hours.[179] MoO_3 is not the only material that has been added to prevent the corrosion effects of acidic PEDOT:PSS; $CuAlO_2$ is another candidate that when mixed with PEDOT:PSS demonstrated higher efficiencies of 12.48% vs 10.11% for PEDOT:PSS without $CuAlO_2$ and improved device stability.[180]

Devices with CuAlO$_2$ maintained over 80% of their initial efficiency after 240 hours under ambient conditions, an improvement over the 35% mark set by standard PEDOT:PSS devices under the same conditions.[180]

Choi et. al also wanted to replace the acidic PEDOT:PSS so they developed a pH neutral and low temperature processable conjugated polyelectrolyte. Using poly[2,6-(4,4-bis-potas- siumbutanylsulfonate-4H-cyclopenta-[2,1-b;3,4-b']-dithiophene)- alt-4,7-(2,1,3-benzothiadiazole)] known as CPE-K, the group created devices exceeding 12% efficiency with enhanced durability under ambient conditions.[160] CPE-K displayed enhanced charge separation with more efficient photoluminescence (PL) quenching than PEDOT:PSS, with quenching efficiencies of 71% and 99% for PEDOT:PSS and CPE-K, respectively. Moreover, the average PL decay decreased from 91 ns for glass/PEDOT:PSS/perovskite to 1.41 ns for glass/CPE-K/ perovskite.[160]

To overcome the economic manufacturing limitations associated with creating polymer HTMs by using existing industry techniques like solution-processing or vacuum coating, Yan et al. used electrochemical polymerization to fabricate thin conductive polythiophene films presenting a simple, economic and controllable method to deposit the polymer HTM. [181] Polythiophene showed an improved performance when measured against similarly designed cells using PEDOT:PSS. Time resolved PL demonstrated polythiophene's improved charge transfer with faster decay times of 1.17 ns compared to PEDOT:PSS (2.84 ns). Faster decay rates resulted in higher efficiencies of 15.4%, an improvement over similar devices produced with PEDOT:PSS (11.9%).[181] Polythiophene also demonstrated a higher stability of over 800 hours in a nitrogen-filled glove box. Meanwhile, the PEDOT:PSS cells suffered dramatic decreases in efficiency after one week

under the same conditions.[181] Both tests used the fullerene C_{60} as the electron transport material. To enhance the polythiophene's interface with the perovskite HOMO level, halides bromine and chlorine were added to increase the work function of the polythiophene. Adding chlorine increased the efficiency of polythiophene-based devices to 16.5%.[158]

2.4.4.2 Carbon nanotechnology

Along with spiro-OMeTAD, another common organic hole transport material used in solar cells is P3HT (poly(3-hexylthiophene)). P3HT is popular because of its solubility in a variety of solvents, yet its performance suffers in PSCs due to its flat molecular structure causing enormous charge recombination problems.[182] Another known issue is its low hole conductivity on the order of 10^{-5} S cm^{-1} due to its poor crystalline nature.[183] Carbon single wall nanotubes have been added to encourage crystallinity with π–π stacking interaction.[184] This changes the local molecular orientation of P3HT in a nanoscale dimension along the wall of the nanotubes; resulting in a higher order of crystallinity. The same effects can be seen in multi-walled nanotubes. Bamboo carbon nanotubes (BCN) "knots and joints inside tube structures resembling bamboo" have increased performance from 3.6% efficiency for pure P3HT to 8.3% efficiency for P3HT/(1 wt% BCNs) composites.[182]

Habisreutinger et al. continued the carbon nanotube composite HTM research in PSCs by using Poly(methyl methacrylate) known as PMMA as a sealant for P3HT and carbon nanotubes.[147] They examined the moisture shielding effects of P3HT, Poly[bis(4-phenyl)(2,4,6-trimethylphenyl)amine] (PTAA), and commonly used spiro-OMeTAD by subjecting them to ambient air at 80 °C. spiro-OMeTAD, P3HT, and PTAA all turned from black to yellow, displaying poor protection and degradation to the lead iodide precursor.

The color change to yellow is associated with a transformation of the perovskite crystal structure to a zero-dimensional system in which the individual compounds are present as isolated octahedra.[147] To compensate for the lack of π bonding in PMMA, single-walled carbon nanotubes coated with P3HT were added underneath the sealant of PMMA; creating efficiencies of 15.3% while remaining protected from moisture. The coating was so effective that devices remained operational after submersing them in water.[147]

Carbon can also be utilized alone without the need for a polymer composite. Multi-walled carbon nanotubes with a 15 nm diameter and lengths of several micrometers have achieved efficiencies of 12.67%.[157] Carbon's ability to transmit charge is largely affected by its size as graphite and carbon black 30 nm particles had efficiencies of only 6.1% and 9.4% respectively.[157] Hysteresis was also minimized by using the MWCNTs compared to the graphite or carbon black.

2.4.4.3 Metal Containing HTMs:

In an attempt to move away from difficult and expensive exotic organic HTM syntheses, less expensive metal containing HTMs have been investigated. Cuprous oxide (Cu_2O), copper iodide (CuI), copper thiocyanate (CuSCN), and NiO_2 are among the most studied.[150, 185-188] Cuprous oxide is an ideal hole transport material owing to its' natural p-type conductivity and high carrier mobility of about 100 $cm^2/(V \cdot s)$ and a long carrier diffusion length ranging up to several micrometers.[189-191] Cuprous oxide is a naturally occurring p-type semiconductor because of the negatively charged copper vacancy defects rather than interstitial oxygen.[192] In addition, because of cuprous oxide's relatively large band gap of 2.16 eV, it will not detract light from being absorbed by the perovskite layer. Results of Cu_2O have been impressive with a conversion efficiency of 13.35%, a fill factor

of 0.76, Jsc of 16.52 mA/cm^2, and a V$_{oc}$ of 1.07 V.[149] Cu$_2$O suffers from a transition at room temperature to cupric oxide (CuO). CuO is not as suitable as a HTL since it reduces carrier mobility and hence also the conductivity.[193] In addition, cupric oxide has a smaller band gap (~1.4 eV) that is less suitable in alignment with the perovskite valence band edge.[191] In comparison to spiro-OMeTAD, cuprous oxide devices remained stable after one month in ambient moisture; whereas spiro-OMeTAD based devices lost all efficiency in 12 days.[148]

Another interesting copper HTM is copper thiocyanate (CuSCN), which has good chemical stability, transparency throughout the visible and near infrared spectrum, and a high hole mobility of 0.01 - 0.1 cm^2 V^{-1} s^{-1} (as compared with 4×10^{-5} cm^2 V^{-1} s^{-1} for spiro-OMeTAD).[194-197] Unlike most organic HTMs that cost more than 100 USD per gram, CuSCN costs ~1 USD per gram; making it a promising viable HTM for large scale manufacturing.[186] Furthermore, its low temperature processing makes it compatible with flexible substrates.[186] Qin et al. developed the first CuSCN PSCs with higher efficiencies of 12.4%.[186] Their work revealed a potential manufacturing problem in the partial dissolution of the perovskite during the CuSCN deposition. Ye et al. later used low temperature electrodeposition to increase the efficiency of CuSCN devices to 16.6%.[150] More impressively, the electrodeposition method finished in only 50 s, making it ideal for large-scale manufacturing, with an ideal thickness of 57 nm on ITO.[150]

The last commonly used copper HTM that has been investigated is copper iodide (CuI). Christians et al. used CuI during the early years of perovskite manufacturing, and the results were promising with devices nearing those fabricated using spiro-OMeTAD.[185] The short circuit current density (J$_{sc}$) and conductivity were higher for CuI than spiro-

OMeTAD. However, devices suffered from a low open circuit voltages (V_{oc}). This low V_{oc} was attributed to a higher recombination rate compared to spiro-OMeTAD. The champion CuI solar cell exhibited a power conversion efficiency of 6.0% compared to 7.9% for the group's champion spiro-OMeTAD device.[185] Chen et al. improved the device efficiency to 13.58% in an inverted PSC architecture and utilized PCBM as the electron transport material.[151] Furthermore, CuI devices displayed improved stability compared to PEDOT:PSS devices. The CuI device maintained 90% of its initial efficiency after 14 days storage in air, while the PEDOT:PSS device retained only 27% after 14 days.[151]

Along with cuprous oxide, nickel oxide is another attractive metal oxide candidate with a large band gap and deep valence band (5.4 eV).[198] Undoped nickel oxide layers have delivered 11% efficiency, largely limited by low conductivity.[199] Copper can be used to dope nickel oxide and improve its conductivity from 2.2×10^{-6} S cm^{-1} to 8.4×10^{-4} S cm^{-1}.[198] Devices displayed an increased efficiency of 15.40%.[198] In terms of stability, cells tested in ambient conditions after 240 hours retained 90% of their initial performance compared to PEDOT:PSS devices which deteriorated to below 50% in under 144 hours. This was mainly due to the hygroscopic and acidity problems of PEDOT:PSS mentioned earlier.[198] Park et al. prepared a lower temperature (200 °C) well-ordered nanostructured NiO film by using pulsed laser deposition (PLD).[152] PLD uses the high energy of ejected particles from a target and the resulting laser plume to contribute to the improvement of the crystalline film even at low temperatures. Adjusting the oxygen partial pressure during the deposition changed the film formation from a thin film (10 mTorr) to a nanostructured film (200 mTorr) to a disordered film (900 mTorr). The nanostructured film achieved the highest efficiency with an increased (111) reflection and a minimized (200) reflection.[152]

Lastly, others have tried to avoid a hole transport material by using extremely thin oxide layers like AlO_x. Trimethyl aluminum and water were used as precursor gases in an ALD system using high-purity N_2 as the carrier gas. Five cycles of AlO_x provided an increase in efficiency from 8.6% to 11.1%.[159] IPCE measurements showed that the charge collection ability of the cell in the long-wavelength region was significantly enhanced by the presence of a metal-insulator-conductor (MIS) back contact. The thin the AlO_x layer acted as an electron blocking layer to suppress electron transfer from $CH_3NH_3PbI_3$ to the Au electrode.[159]

2.5 PSC Roll-to-Roll Manufacturing

The ultimate goal for PSCs is roll-to-roll manufacturing on inexpensive plastic substrates that can drive down the cost of solar energy. Despite this realization, most perovskite research articles focus on spin-coating techniques. Spin-coating provides uniform films and has been tremendously successful at the lab scale; however, it is not suited for large-scale industry manufacturing.[200] Instead, this review will focus on established perovskite deposition techniques that are suitable for roll-to-roll manufacturing. Such techniques include spray coating, doctor blading, slot die coating, and inkjet printing. The top devices based on these techniques are shown in **Figure 2.7**.
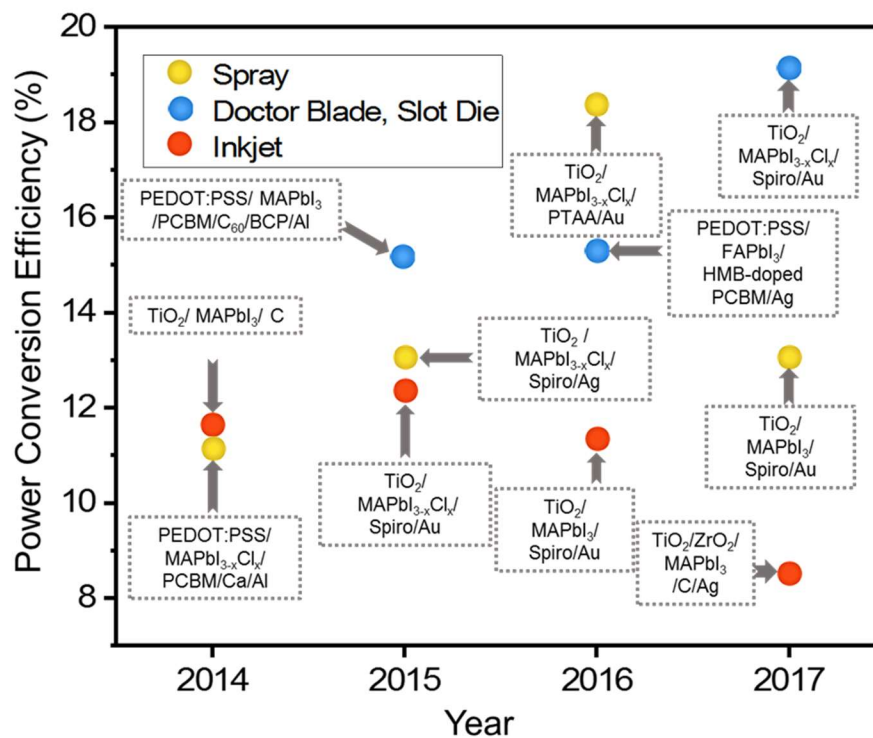
Figure 2.7. Yearly top performing perovskite solar cells using roll-to-roll applicable inexpensive processing techniques and their respective architectures[200-210]

2.5.1 Spray Coating

Spray coating is advantageous in large scale applications as it provides high throughput, uniform film coverage, better control over directional deposition, and has compatibility with a wide range of substrates.[211-214] Spray coating perovskite articles first began to appear in 2014 when Burrows et al. created cells with efficiencies exceeding 11%.[207] The group utilized an ultrasonic spray nozzle to deposit methylammonium iodide (MAI) and lead chloride ($PbCl_2$) to form $CH_3NH_3Pb_{3-x}Cl_x$. The nozzle operated with a 35 kHz vibrating tip. The oscillating nozzle was critical as it minimized the formation of large droplets coalescing on the substrate and effecting film uniformity.[215-216]

Another important aspect of the work highlighted the importance of solvent boiling point. Lower boiling point solvents such as chloroform are prone to pinhole formation as the solvent dries before reaching the substrate. [217] On the contrary, using higher boiling point solvents such as DMF and DMSO can lead to shrinkage or dewetting of the coating from prolonged drying times.[218] To avoid this, a two part thermal treatment was utilized. The first thermal treatment accelerated the drying process to avoid dewetting and shrinkage. The second thermal treatment annealed and crystallized the perovskite to enhance its photovoltaic properties. Optimization of the first thermal treatment proved crucial in creating a uniform layer void of pinholes. Meanwhile the second thermal treatment was optimized between 90 °C and 130 °C. At temperatures less than 90 °C, the perovskite did not fully crystallize while at annealing temperatures above 110 °C, the perovskite underwent partial dewetting and had poor surface coverage.

Spray coated PSC efficiency improved to over 13% in the following year (2015) by optimizing the infusion rate of the precursor and solution concentrations to 3.2 mL/min and 10 wt% solutions respectively. Another addition was the use of a pressurized atomizing nitrogen-gas that prevents clogging of the nozzle head while providing an inert environment for the perovskite precursors.[208]

The research had a breakthrough in 2016 when over 5 works eclipsed the 2015 efficiency. Heo et al. created an 18.3% PSC comprised of $CH_3NH_3Pb_{3-x}Cl_x$ with an atomic ratio of Cl:I of 3:97 by mixing a 3:1 molar ratio of MAI to $PbCl_2$ in a mixture of DMF and GBL.[209] Higher uniformity perovskite crystals were obtained by removing the unreacted products and side products with isopropanol washing and filtration.[209] The perovskite crystals were then redispersed in a solvent mixture of DMF and GBL for spraying. GBL

was added to suppress the vapor pressure and prolong the crystal growth period, creating larger crystals with greater film uniformity. The addition of GBL helped to smooth the perovskite film until it reached a volume ratio 7:3 DMF:GBL . At concentrations > 7:3, dewetting of the film occurred due to incomplete drying. Other important findings included the growth of small deposited crystals by a re-dissolution/grain merging/re-crystallization mechanism, and the inverse correlation between the solvent concentration profile and crystallization rate profile from the top to the bottom of the perovskite film.[209] A larger connected module of 40 cm^2 delivered an efficiency of 15.5%.

Sequential deposition is another method that has been utilized to achieve high efficiencies of over 16%.[219] In this approach DMSO was chosen as the solvent for PbI_2. DMSO was preferred over DMF to prevent rough surface morphologies resulting from the relatively weak interaction between PbI_2 and DMF that leads to fast crystallization and growth of PbI_2 in an atmospheric environment.[220-222] DMSO also has a higher binding energy to PbI_2 so it can be used to produce thicker PbI_2 films. Smooth PbI_2 films were deposited with DMSO resulting in high uniformity; likely from the formation of $PbI_2(DMSO)_x$ complexes. These complexes are important in the PbI_2 film uniformity and full conversion to perovskite upon the addition of MAI. Annealing temperature is also critical to $PbI_2(DMSO)_x$ complexes. At 60 °C, the PbI_2 completely converted to $CH_3NH_3PbI_3$. Temperatures higher than 80 °C were too high for the $PbI_2(DMSO)_x$ complexes and temperatures lower than 60 °C contained an excess concentration of $PbI_2(DMSO)_x$ complexes that produced poor perovskite coverage due to left over $PbI_2(DMSO)_x$ complexes.[219] Another advantage mentioned in the work was the increased thermal stability of the sprayed perovskite in comparison to the spin-coated perovskite. The

spin-coated perovskite began to decompose after a 115 °C heat treatment for 6 hours. However, the spray coated perovskite did not degrade until after 36 hours. This is likely due to higher crystallinity in the spray coated sample as noted by the increase in the intensity of the XRD reflections.[219]

Unlike the first two methods, Tait et al. concurrently sprayed the precursors and allowed them to mix in the process line before reacting on the substrate heated by a hot plate.[223] They investigated precursor mixtures of $PbAc_2$/MAI and $PbCl_2$/MAI in DMF solvent. Molar concentrations of 0.8:2.4 of lead precursor to MAI were used for all devices. The mixing of the precursors produced crystals of higher uniformity and suggested less microstructural strain and defects came from the mixed precursor solutions.[223] The highest efficiency devices were made using a precursor molar ratio of 3:1 $PbAc_2$ to $PbCl_2$. Compositions with <30% $PbAc_2$ required longer annealing times at lower temperatures for optimal coverage and performance. At compositions between 40-90 mol% $PbAc_2$, the fill factors for the devices remained higher than 70%. However, outside of this range the device performance dropped off considerably as pinholes and stress-induced cracks at grain boundaries formed. Substrates were heated at 40-60 °C as lower temperatures resulted in dewetting and higher temperatures dried the droplets before they could coalesce and formed poor films.

While many researchers concentrated on the spraying parameters, others focused on the post-treatment of the sprayed films. Nejand et al. utilized a cold pressing technique that continuously spread viscous liquid and paste by simultaneous rolling and pressing.[224] The cold pressing technique smoothed the roughness caused by spray coating and removed pinholes in the films. A 1:3 molar ratio of $PbCl_2$/MAI in DMF was sprayed on to a heated

substrate at 180 °C followed by a slight vapor stream of DMF (1.67 mL/min) at room temperature before being cold pressed with 0.2 MPa of force. The introduction of the DMF partially dissolved the surface of the perovskite so that it could be compressed into a homogeneous film. The cold pressing compressed taller perovskite columns with smaller diameters into shorter connected columns with wider diameters to obtain a continuous perovskite film. The cold pressing technique improved efficiencies from 10.06 to 13.24%.[224]

In a later work, Nejand et al. also used heated Teflon compression plates to create a smooth pin-hole free film.[225] Whereas other groups insisted that the solvent was essential in the spray coating process, Nejand et al. sprayed perovskite crystals dispersed in isopropanol and avoided hazardous DMF and DMSO solvents. Prior to spraying, the perovskite crystals were ball milled in a ball milling jar containing MAI dissolved in isopropanol in a nitrogen environment. Without the use of DMF and DMSO, it was feasible to fabricate devices on copper iodide and an efficiency of 7.71% was achieved compared to 11.28% using spiro-OMeTAD as the hole transport layer.[225]

Later, perovskite spraying mechanisms were also an area of interest as Remeika et. al investigated the parameters that achieved high quality perovskite spray coatings like wet film thickness and evaporation rate.[210] Laser light interference and scattering enabled real-time monitoring on wet films. The average liquid evaporation rate was determined from oscillations of the reflected beam intensity of the laser. The data provided a way to calculate the evaporation rates of any solvent. This method could be easily adopted to other spray coating systems to determine the evaporative mass transfer coefficient and wet film thickness as a function of specific machine settings. This is a more accurate technique than

a simple mass conservation as spray profiles are difficult to characterize, the fraction of the solvent that evaporates from the ink during its flight from the nozzle to the substrate must be known, and the ink may flow laterally before it achieves a stable thickness.[210]

2.5.2 Doctor Blading and Slot Die

Like spray coating, doctor blading is also appealing to roll-to-roll manufacturing with its simplicity, cost effectiveness, and application onto flexible substrates.[226-228] In 2015, devices were fabricated with efficiencies exceeding 15%.[200] The perovskite was deposited on heated slides at a speed of 27 m/h from precursors of MAI and PbI_2 in DMF. Only 10-20 µL of solvent were required for 2.25 cm^2 slides providing a reduction in material usage when compared to the 50-100 µL of precursor needed for similar sized spin-coating depositions.[200] Similar to spray coating, slide temperature proved to be important for blade coating to obtain dense pinhole free films with high efficiencies. Films formed at 100 °C had rough surfaces with large voids and only amounted to efficiencies of 7%. Meanwhile quick drying films (<2 s) at 125 °C created uniform and continuous films. A study of the composition of the precursors showed that stoichiometric ratios of MAI to PbI_2 yielded the highest efficiencies. Thickness of films was also changed and the highest efficiency devices had a thickness of 3.1 µm. This is much larger than spin coated devices which is likely due to higher carrier diffusion lengths shown in blade coated samples in comparison to spin coated samples. This could be a result of an increase in the (220) plane intensity of the perovskite doctor bladed films. It could also be due to the larger grain sizes, as doctor bladed crystals extended from the anode to the cathode without grain boundaries.

Similar to doctor blade coatings, Hwang et al. developed slot die coatings on planar zinc oxide electron transport material.[229] To avoid ion migration and the formation of

overgrown crystals that produce uncoated areas on films, the substrates were heated and underwent nitrogen gas quenching immediately following the coating. The PbI_2 films formed on the heated substrates proved to be too dense and prevented full reaction of PbI_2 to perovskite when reacted with MAI applied by dip coating or slot die coating. This was common in the sequential perovskite deposition spin-coating process.[23] To avoid this, a solvent vapor soaking technique, used previously in organic solar cells,[230-231] was used immediately following the nitrogen quenching. The technique turned the lead iodide layer cloudy and provided micro cracks in the film for full infiltration and reaction of MAI to form a perovskite layer void of remnant lead iodide without being too large to create pinholes and negatively affect device performance. The glassy lead iodide based cells showed a poor average efficiency of 0.47% compared to the average 11.94% efficiency of the cloudy lead iodide based cells.[229] Efficiency also improved by increasing the temperature of the slot die coated MAI solution to 70 °C. Above this temperature, the solvent started to evaporate.

Following the introduction of formamidinium into PSCs by spin-coating, the formamidinium PSCs were also produced by blade coating with an efficiency of 15.23% over an area of 1.2 cm^2.[232] In this work, Chang et al. prepared devices with a modified hexamethonium bromide doped PCBM to reduce the work function of the PCBM to better match more stable metal contacts like gold and silver. Then lead iodide was doctor bladed onto the substrates and reacted with FAI in isopropanol.

As solvent-solvent extraction gained popularity in spin-coated devices, researchers at NREL wanted to expand the processing time of applying the secondary solvent to configure it to scalable blade coating processing. By manipulating the solvent composition, Yang et

al. extended the precursor processing time from seconds to several minutes.[202] Processing

delay times for the perovskites made with DMF were immediate whereas mixing DMF

with DMSO extended the processing time by >2 minutes, and mixing DMF with NMP

extended the processing time by >8 min. The change in processing time was related to the

time spent as a wet film. The higher vapor pressure DMF evaporated quickly while the

lower vapor pressure NMP evaporated slower and stayed in the wet film stage longer.

Although NMP would appear the best choice as a solvent, it had a relatively high viscosity

that resulted in heterogeneous traces after the blade coating. Mixing with DMF helped to

lower the viscosity of the NMP to provide uniform films. To decrease the annealing time

and enhance process throughput, an excess of MACl was added to the precursor mixture

of PbI_2 and MAI. The excess MACl shortened the annealing time from 10 minutes down

to 1 minute. The optimal amount of excess MACl was 30%. Yang et al. achieved device

efficiencies of 19.05% when deposited on PCBM modified TiO_2 with spiro-OMeTAD as

the hole transport layer and silver as the contact.[202]

2.5.3 Inkjet printing

The last technique of interest is inkjet printing. Inkjet printing is advantageous as a

material-conserving deposition technique for fast deposition of materials on various

substrates over larger areas.[233-235] Wei et al. created the first cells of higher than 10%

efficiency by inkjet printing a MAI/carbon hole transport material composite.[236] Cells were

prepared using two methods: the first method inkjet printed the carbon layer followed by a

dip in an MAI isopropanol bath; the second method inkjet printed the carbon and the MAI

together in a composite ink. The ink prepared with both the MAI and the carbon produced

a more crystalline perovskite and better interface quality between the carbon and

perovskite. This resulted in higher efficiencies (11.60%) compared to the cells prepared with separate inks (8.51%).[236]

Li et al. improved on this technology by eliminating the PbI_2 spin coating step and depositing PbI_2, MAI, and MACl in a 35 wt% solution of gamma-butyrolactone using a piezoelectric flatbet inkjet printer.[204] Gamma-butyrolactone was chosen as the solvent to prevent nozzle clogging due to solvent evaporation during printing. In contrast to spin-coating techniques where centrifugal forces are used to drive away the solvent, inkjet printed films exist in a fluid state and must be dried quickly to prevent large thickness variations in the perovskite films. When deposited at room temperature the printed films were covered with perovskite crystallites of distinct edges and corners. The film morphology changed to uniformly spread round and flattened crystal plates when annealed at 40 °C, similar to spin coated films. The optimal coverage occurred at 50 °C when smaller crystallites appeared in-between the large crystals. However, at 60 °C, abundant pinholes formed on the surface resulting in deteriorated perovskite performance. Adding MACl helped improved devices from 7.3% to 12.3%.[204] When the addition of MACl was at a 0.3 molar ratio to MAI, flower like crystal plates formed differing from the disc plates seen from iodide precursors. The flower like crystal plates smoothed to uniform films when increased to 0.6 molar ratio. When raised to 0.9 molar ratio, the films underwent dewetting and exhibited worse surface coverage in comparison to the 0.6 molar ratio films.

After this publication, efficiencies stalled using inkjet deposition. While efficiencies have not increased, techniques have been introduced to improve the inkjet deposition. Vacuum annealing was introduced by Mathies et al. as a method to create smooth dry films with complete coverage in under 5 minutes.[205] Further increase of the vacuum annealing

to 10 minutes created rough perovskite films. Another contribution to the field by Bag et al. showed improved reproducibility (standard deviation of only 0.3%) by using multi-channel printing rather than mixing the precursors prior to printing.[237]

2.6 Outlook for Flexible PSCs
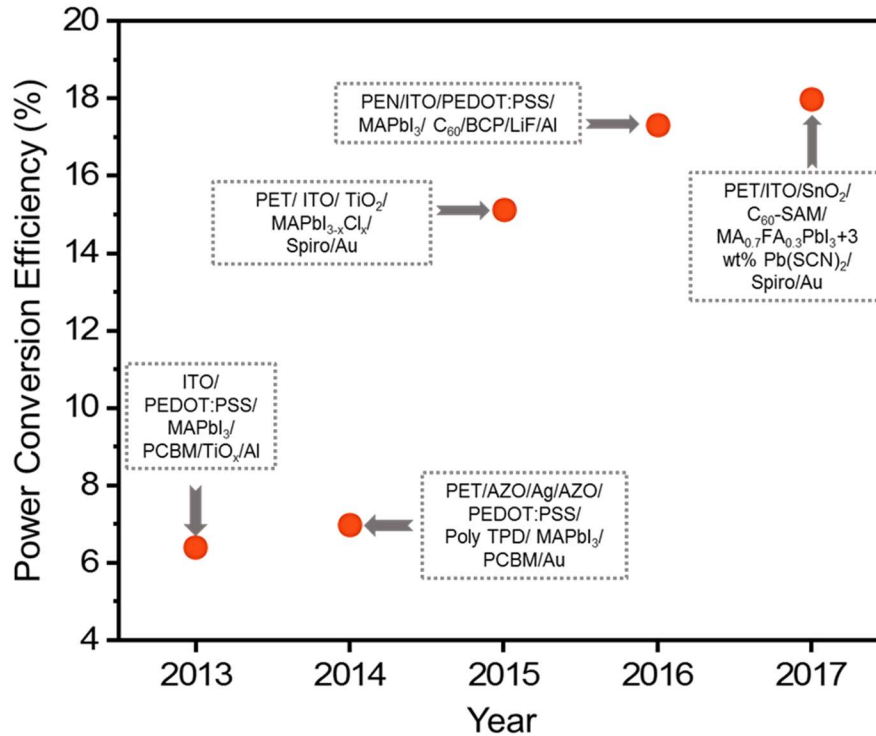
Figure 2.8. Yearly top performing flexible perovskite solar cells fabricated and their respective architectures [238-242]

While the perovskite solar cell (PSC) still has many uncertainties regarding its instability to light and moisture, the processing challenges are being resolved. Efficiencies have increased to over 19% by using scalable technologies including spray coating, doctor blading and slot die, and inkjet printing. The future of PSCs is in flexible device manufacturing. Being able to process on inexpensive materials will greatly benefit the PSC module costs as it tries to compete with the market favorite silicon technologies. Already

flexible PSCs are gaining efficiencies of over 18% **(Figure 2.8)**. The researching breakthroughs so far in the manufacturing of flexible PSCs generate exciting optimism for the future of the perovskite solar cell.

2.7 IPL Photonic Manufacturing

The energy pay-back time (EPBT) for manufacturing the market leading silicon solar cells is currently between 2 and 4 years, and continues to fall.[243-244] However, very high energy thermal processes exist within the manufacturing process, from the growth of the ingot through cell processing and the panel assembly.[245-246] The challenge exists to minimize these high energy thermal processes to bring down the cost in the manufacturing of solar energy.

A localized heating technique, Intense Pulsed Light (IPL), also known as flash light sintering and photonic sintering, has been very successful in the printed electronics industry.[247] In this application, metal nanoparticle films are deposited onto flexible substrates using well known printing techniques such as screen printing, gravure and inkjet printing.[248-252] These films are then subjected to the IPL process in which the materials often undergo both chemical and solid state modifications, resulting in conductive bulk thin films. The developed inks and range of depositions with the scalability of the IPL process yield prospects of large scale production in roll-to-roll manufacturing on flexible substrates.

The IPL technique works by using a Xenon plasma bulb to deliver high-energy light, in the broad range of 190 nm to 1100 nm, **(Figure 1.3)** in a very short duration over a large processing area, heating thin films containing photosensitive nanoparticles with measured temperatures of several hundred °C.[29-30] In this process the incident radiation

$I_0(\lambda)$ is directly related to the spectrum of light $(S(\lambda))$ a fixed property of the lamp **(Figure 1.3)** where the energy density (ED) of the light is a function of the voltage applied to arc the Xenon source. The conversion of the electrical to optical radiation is at least 30% and exceeds that of lasers, making IPL a more efficient manufacturing technique.

The absorption of the light by the film is modeled using a Beer-Lambert law, where the amount of absorption is related to absorptivity of the material (α) which varies over the wavelength range (λ) **(Figure 1.3)** and may also vary along the depth (y). The generated heat (Q) at a depth y is then computed by integrating the absorption of the light source over the wavelengths produced multiplied by the area of illumination (A) as:

$$Q(y) = A \iint I_o(\lambda) e^{-\alpha y} d\lambda dy$$

Note that the heat generated is depth dependent and the α and t of the film will determine how much of the light is absorbed. The heat generated then results in a temperature (T) response that varies by time (t) and position as described by the heat equation:

$$\rho C_p(T) \frac{\partial T}{\partial t} = \nabla(k \nabla T) + Q(y)$$

Where the material properties are the density (ρ), heat capacity (C_p) and the thermal conductivity (k). The thermal diffusivity of a material $(k/\rho C_p)$ establishes the rate at which heat will conduct and the diffusion length of a pulse can be computed as:

$$d = 2 \sqrt{\frac{k\tau}{\rho C_p}}$$

The diffusion length of metallic and semiconducting materials for PV are on the order of hundreds of microns, so the heating of thin films less than 1 micron is near

instantaneous. On the contrary, the diffusion length for a polymer substrate is tens of microns and the ratio of the diffusion length to thickness is much smaller for the substrate than the film. Consequently, the substrate is spared of the high temperatures as the heat energy introduced is quickly dissipated before being transmitted into the substrate.[31] Thus the process focuses heat only where it is necessary, which is the within the thin film and can be implemented on more fragile organic substrates such as polymers and papers.

All of the material properties (α, ρ, C_p and k) are a function of the porosity of the material and may experience variations underscored by changes to the morphology. This may not influence the response of the films to a single IPL pulse, but may become significant for prolonged exposure to multiple pulses. Correspondingly, the pulse frequency and the number of pulses are simply functions of time and influence the thermal response in the time domain, but do not figure into the instantaneous absorption. Dhage et al. successfully reacted selenium nanoparticles into a thin film of Cu(In0.7Ga0.3) (CIG) metallic alloy nanoparticle precursors using IPL within milliseconds. They were also able to melt and recrystallize CIGS particles into larger grains without structural deformation or phase transformation.[253-254]

CHAPTER 3

EXPERIMENTAL METHODS

3.1 IPL Treatment of electrodeposited CdTe

3.1.1 Electrodeposition of CdTe

CdTe films were grown by two-electrode cathodic electrochemical deposition on to TEC-8 fluorinated tin oxide glass substrates (FTO, Hartford Glass Co. Inc.). The FTO was used as the cathode and a graphite rod was used as the anode. The 6.0×4.5 cm^2 substrates were placed in a Teflon vessel holding 1400 mL aqueous solution of 0.5M CdSO$_4$ (Sigma Aldrich) and the pH was lowered to 1.44 using 1 M H$_2$SO$_4$ (Sigma Aldrich). The deposition was carried out at 85°C, and the films were deposited for 2 h. The cathodic growth voltage (V_g) applied using a Keithley 2400 source-meter was varied from 1.401 V to 1.626 V with stoichiometric films produced at 1.526V. The deposition current density was maintained at ~125 μA/cm^2, by adjusting the stirring rate and adding TeO$_2$ (Sigma Aldrich) dissolved in 1 M H$_2$SO$_4$.

3.1.2 IPL Sintering of the CdTe Films

Once the films were grown, CdTe was IPL sintered in air using a Sinteron 2000 (Xenon Corporation). The system delivered rapid pulses of light with wavelengths ranging from the UV to IR region, as mentioned previously. In this case, CdTe was treated with pulses lasting 1.0 ms. The system was set so that the lamp cycled between its "ON" and "OFF" conditions. During the ON segment, the lamp pulsed/ flashed twice, whereas no

flashes occurred during the OFF segment. Each segment lasted 1.0 s, with a 0.5 s gap between pulses. The total energy input to the films was varied by changing the energy density (ED) of each pulse from 8.6 to 25.9 J/cm^2. The number of pulses applied to the films was fixed to 100 pulses; this corresponded to a total processing time of 100 s.

3.2 CdCl₂ Treatment of CdTe Films

CdTe was IPL treated after the deposition of a thin $CdCl_2$ film. The $CdCl_2$ was spin coated on to the surface of the as-deposited film from an aqueous solution of 1.0 M $CdCl_2$ (Sigma-Aldrich). The films were then IPL processed by using energy densities of 8.63, 12.94, 17.26, 21.57, and 25.88 J/cm^2 and 100 pulses, for a total processing time of 100 s. Thus total energy input of 860, 1290, 1730, 2160, and 2590 J/cm^2 was used.

3.3 IPL Sintered Perovskite Solar Cell

3.3.1 Device Fabrication

The etching, TiO_2 deposition, and IPL sintering steps were conducted in ambient conditions outside of a glovebox. All other steps were done in a nitrogen glovebox with less than 150 ppm moisture and less than 10 ppm oxygen. IPL processing conditions were performed in a sealed container with a nitrogen atmosphere. To create positive contacts for the perovskite devices, FTO-coated slides of glass were etched using zinc powder and 2M HCl. Then the slides were cleaned by sonicating in Hellmanex alkaline detergent for 10 minutes to remove heavy debris, then DI water for 10 min to remove the detergent, followed by ethanol for 10 min to remove organics, and then again in DI water for 10 min to remove the excess ethanol. After cleaning the slides, they were dried under a stream of compressed nitrogen to avoid dust. Next, the slides were cleaned under an oxygen plasma

to get rid of any remaining residue followed by a UV treatment for 30 min to passivate the FTO surface for higher wettability of the TiO_2 layer.

The TiO_2 layer consisted of three steps: a compact layer of ~ 20 nm to prevent shorting of the devices, a mesoporous layer of 200-400 nm to facilitate in charge transfer from the perovskite to the n-type TiO_2, and then a sol-gel chemical bath deposition (CBD) to facilitate interconnections between the mesoporous TiO_2 particles. The compact TiO_2 layer was performed by spin coating a 0.15 M titanium diisopropoxide bis(acetylacetonate) "TAA" (CAS: 17927-72-9) solution dispersed in anhydrous1-butanol. The solution was spin coated onto slides at 700 rpm for 8 s, 1000 rpm at 10 s, and then 2000 rpm for 40 s. The slide was not stopped between the different spin speeds. After spin coating, the contact areas were wiped with a cotton swab wet with ethanol. Then the slides were heated on a hot plate set at a low temperature of 120 °C for 5 min to remove the solvent without causing cracks or pinholes in the film. The mesoporous TiO_2 Layer consisted of Dyesol 18NR-T TiO_2 paste diluted in a mixture of 1:4 by weight with ethanol and sonicated until it became a well-dispersed solution. The solution was spin coated at 2000 rpm for 60 s to produce 200−400 nm thickness. Again, after spin coating, the ends were cleaned of the TiO_2 paste with a cotton swab dipped in ethanol to provide device contact areas. The slide was heated on a hot plate set at 120 °C for 5 min to remove the solvent. The slides were then heated in an oven at 500 °C for 1 h to crystallize the TiO_2 particles. In the final CBD, a 90 mM solution of $TiCl_4$ (CAS: 7550-45-0) in 20% HCl was diluted to 40 mM in DI water. The slides were placed in the solution and heated in an oven at 70 °C for 30 min to fill any remaining pinholes in the film. Following the reaction, the slides were removed and rinsed

with water to clean away any unreacted solvent. Slides were heated again at 500 °C for 30 min to crystallize the thin layer of TiO_2 provided by the $TiCl_4$ solution.

The PbI_2 Layer was prepared by mixing a 498 mg/mL solution of PbI_2 (CAS: 10101-63-0) with dimethylformamide (CAS: 68-12-2), "DMF", anhydrous, using a stir bar and heated on a hot plate at 80 °C. Slides were preheated on a hot plate to 45−60 °C, as checked using an IR thermometer. Slides were moved quickly to the spin coater, and the hot solution of lead iodide was dropped onto the cell using a glass pipet until the cell was fully covered. Following the drops, the slides were spun at 4000 rpm for 20 s to get a dense coverage of 200−250 nm on top of the mesoporous TiO_2 layer. Following the spin coating, the slides were placed on the edge of hot plate until the batch was finished and then heated on a hot plate set at 100 °C for 5 min to remove the remnant solvent.

The lead iodide was then reacted with a mixture of 10 mg/mL of MAI (CAS: 14965-49-2) dissolved in anhydrous isopropanol to form $CH_3NH_3PbI_3$ perovskite. The mixture was shaken until evenly dispersed. Slides were dropped into a solution of isopropanol for 2−3 s before being dipped into a mixture of MAI and isopropanol for 90 s to slow the reaction and enable a longer nucleation period. After conversion, the slide was dipped again in isopropanol for a few seconds to clean off any unreacted MAI solution. Reference slides were heated on a hot plate set at 70 °C for 30 min to grow perovskite crystals. IPL sample conditions are explained in the body of the paper.

The hole transport material spiro-OMeTAD was also deposited via spin coating. A 72.3 mg portion of spiro-OMeTAD (CAS: 207739-72-8) was shaken in 1 mL of chlorobenzene until it dissolved. Then it was doped with 28.8 μL portion of 4-tert-butyl-pyridine (CAS: 3978-81-2), 17.5 μL of stock solution of 520 mg/mL lithium bis-

(trifluoromethylsulfonyl) imide (CAS: 90076-65-6) in anhydrous acetonitrile, and 29 µL of Dyesol cobalt dopant FK209 TFSI salt (CAS: 1447938-61-5) 300 mg/mL in anhydrous acetonitrile. The spiro-OMeTAD solution was dropped onto the perovskite slides until it covered the entire film (70 µL) and was spun at 1700 rpm for 30 s to get a thickness of 200 nm.

The contacts regions were prepared by scraping with a blade to expose the glass and FTO sides. An 80 nm layer of gold was deposited using a thermal evaporator at a rate of 1 Å/s inside a nitrogen environment.

3.3.2 Finite Element Analysis

The 1-D finite element analysis was carried out using COMSOL Multiphysics to simulate the time-dependent heat transfer of the perovskite under the IPL. The pulses were modeled using triangular waves over a duration of 2 ms to simulate a pulse from the IPL. Glass was used as the substrate with the following properties: a density of 2200 kg/m^3, a thermal conductivity of 1.1 W/m*K, a heat capacity at constant pressure of 480 J/(kg*K), and a surface emissivity of 0.94. The $CH_3NH_3PbI_3$ perovskite had the following properties: a density of 4000 kg/m3, a thermal conductivity of 0.5 W/(m*K), a heat capacity at constant pressure of 320 J/(kg*K), and a surface emissivity of 0.85. Convective, conductive, and radiative heat transfer were used in the simulation. To simulate the heat generated by the IPL, a boundary heat source was used. Xenon Corporation supplied data correlating the input and output energy of the IPL setup for different processing conditions. These ranged from 20-25% electrical energy to broadband photonic energy. As a final check to ensure the simulation was accurate, a test was performed on a silicon substrate with a k-type

thermocouple attached to the back. The plot of the heat vs. time given by the thermocouple was a match to that of the simulation.

3.4 2-D Layered Perovskite

3.4.1 Device Fabrication

The cleaning, compact TiO_2, mesoporous TiO_2, $TiCl_4$ treatment, spiro-OMeTAD, and gold deposition are the same as detailed in section 3.31. The only change is the perovskite reaction in which a mixture of 1.7 M 1:1 by molar BAI:MAI with 1.7M PbI_2 in a 1:4 V DMF:DMSO solvent was stirred overnight and deposited via spin coating. The spin coating settings were 1000 rpm for 10 s followed by 3000 rpm for 20 s, during which 100 µL of chlorobenzene was dropped as an anti-solvent. Slides were then immediately moved to a hot plate set at 100 °C and heated for 1 h.

3.5 Electrochemical Device Characterization

The linear sweep voltammetry, electrochemical impedance spectroscopy (EIS), and photoelectrochemical measurements (PEC), were performed using a BioLogic SP200/Z-01 potentiostat. The measurements were performed under the illumination of a Xenon lamp equipped with a AM 1.5 filter and the light power was adjusted by changing the distance from the source to the device.

3.5.1 Linear Sweep Voltammetry

Linear sweep voltammetry is a critical characterization tool in photovoltaics, delivering the short circuit current J_{sc}, open circuit voltage V_{oc}, fill factor FF, and the solar cell efficiency. Linear sweep voltammetry is run by a potentiostat that measures the current (A) as the potential (V) is varied linearly at predetermined step sizes.

Solar cells create photocurrent under illumination which is related to their quantum efficiency (QE) and incident spectral photon flux density $b_s(E)$. The quantum efficiency is the probability that an incident photon of energy E will deliver one electron to the external circuit. The $b_s(E)$ is the number of photons of energy in the range of E to E +dE that are incident on unit area in unit time. When the electronic charge (q) is multiplied to the integral of these two parameters we have the short circuit photocurrent density J_{sc} which is an important metric used to describe solar cell performance.

$$J_{sc} = q \int b_s(E)QE(E)dE$$

Solar cells are also characterized by their open circuit voltage (V_{oc}). This is the maximum potential difference a solar cell can have and is measured when there is zero current density of the solar cell. It can be described as:

$$V_{oc} = \frac{kT}{q} \ln(\frac{J_{sc}}{J_0} + 1)$$

in which k is the Boltzmann's constant, T is the temperature, q is the electronic charge, J_{sc} is the short circuit current density, and J_0 is a constant.

If analyzed in an electrical circuit, solar cells would feature an equivalent circuit of a current generator in parallel with an asymmetric, nonlinear resistive element such as a diode **(Figure 3.1)**. In operation, the diode provides the photovoltage necessary to drive the photocurrent proportional to the light intensity divided between the variable resistance of the diode and the load.
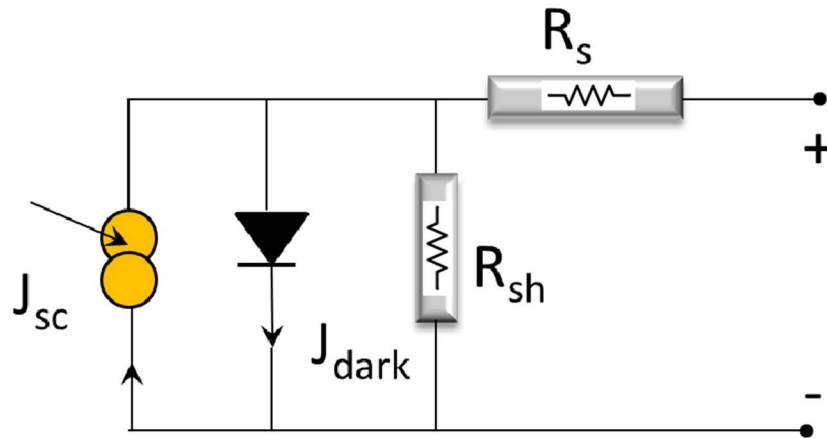
Figure 3.1. Equivalent circuit diagram depicting a solar cell

Multiplying the voltage by the current gives the power density. The maximum power point is the solar cell's maximum operating power and is used to calculate the fill factor (FF) which describes the squareness of the J-V curve and is used to describe losses in efficiency. The fill factor is defined as:

$$FF = \frac{J_m V_m}{J_{sc} V_{oc}}$$

where J_m and V_m are the current and voltage generated at the maximum power point respectively and J_{sc} and V_{oc} are the short circuit current density and open circuit voltage, respectively.

The efficiency of the solar cell is then related to the fill factor by:

$$\eta = \frac{J_{sc} V_{oc} FF}{P_S}$$

where η is the efficiency, J_{sc} is the short circuit current density, V_{oc} is the open circuit voltage, FF is the fill factor, and P_s is the incident light power density. The Standard Test Condition (STC) for solar cells is the Air Mass (AM) 1.5 spectrum with an incident power

density of 1000 W/m^2 and a temperature of 25 °C. The AM 1.5 spectrum corresponds to the sun being at an angle of elevation of 42°.

3.5.2 PEC Measurements

Photoelectrochemical (PEC) measurements were conducted in a three-electrode setup to investigate the photovoltaic properties of the CdTe films. The samples were measured in an aqueous 0.1 M Na_2S solution, using a Ag/AgCl reference and a platinum counter electrode. The potential was scanned with an eDAQ potentiostat using a scan rate of 20 mV/s. The films were illuminated from the front side using AM 1.5 simulated light from a Newport 300 W Xenon Arc lamp.

3.5.4 Impedance Spectroscopy

Impedance spectroscopy (IS) measurements were performed to help understand the internal electrical processes and suggest the shortcomings of the converted 3D perovskites. Impedance spectroscopy applies a small-amplitude modulated voltage stimulus and detects the responding modulated (alternating) current.[255] Impedance spectroscopy results are conventionally presented as a Nyquist plot, with the real component of the impedance (Z′) as the abscissa and the imaginary part (Z″) as the ordinate.[256]

3.6 UV-Vis Spectrometry

The optical properties of the films were analyzed using UV-Vis spectrometry. A Perkin Elmer Lambda 950 UV-Vis spectrometer with a 60 mm integrating sphere was used to understand the absorbance (A) and transmission (T) characteristics of the films. The two metrics are related are related accordingly:

$$A = 2 - \log_{10} \%T$$

Coupled with the thickness of the films analyzed using cross-section scanning electron microscopy (SEM) measurements or a profilometer, the absorption coefficient can be calculated:

$$\alpha = \frac{A}{t}$$

where the absorption coefficient (α) is equal to the absorbance (A) divided by the thickness (t)

3.7 Photoluminescence (PL)

The PL work was carried out using a Renishaw inVia Raman Microscope with a 632 nm (1.96 eV) He–Ne laser as the excitation source. Since the excitation source is in red, the light beam can easily penetrate through the thin films of 1.0–2.0 μm thick CdTe or perovskite layers. Therefore, the PL results reported in this dissertation represent the changes within the bulk of the thin film. The surface area of 25 μm^2 was excited by 14.8 mW laser beam. The detector used in this system is a combination of a diffraction grating and a CCD camera. The system is capable of measuring a wide range of energies. The samples were cooled to approximately 80 K using a Linkam THMS600/720 temperature controlled stage with liquid nitrogen and maintained at this temperature over the length of the PL measurements. The PL peaks in the energy range, 0.55–1.85 eV below the conduction band (CB) were explored in order to investigate any changes in the defect levels and the band-to-band electron transitions.

3.8 Microscopy Methods

An FEI Nova NanoSEM 600 scanning electron microscopy (SEM) was used to study the morphology of the surfaces with an accelerating voltage of 15 kV and a working distance of 5–6 mm. A thin layer of gold was sputtered on the surface of the nonconducting

samples before being studied by the SEM to avoid charging effects. The SEM topographical images were analyzed to find the particle diameter by using the ImageJ software. The average maximum and minimum Feret diameters were measured by excluding the particles touching the edge of the image. Cross-sectional images of the as-deposited and IPL-treated films were performed by mechanically breaking the sample and charging effects were reduced by covering the surface with a platinum and iridium coating. Optical microscopy images of films were carried out using a ZEISS Axio Imager A2m. The high contrast images were taken in the differential interference contrast mode.

3.9 X-Ray Diffraction (XRD)

The material crystallinity and phases were studied using a Bruker AXS D8 X-ray diffractometer. The equipment was operated with an X-ray source of Cu Kα ($\lambda = 0.1548$ nm), a position sensitive detector (PCD), with varying scan speeds of 0.5 to 4 s/step, and a step size of 0.02°. XRD patterns were measured using the $\theta-2\theta$ method in the 2θ range 7−90°.

CHAPTER 4

IPL OF CdTe

4.1 Introduction

The CdTe solar cell industry is under intense pressure to minimize their manufacturing costs as the price of silicon continues to drop and competition increases. The IPL represents a new leaner manufacturing technique that can process materials in seconds rather than the long high temperature (400-600°C) close-space sublimation (CSS) deposition methods used in commercial CdTe devices. Furthermore, with its ability to sinter nanoparticles, it can be used in conjunction with low temperature CdTe deposition techniques that produce nanoparticles. In addition, it would apply the heat directly to the surface with minimal heating of the substrate, limiting the diffusion of substrate materials mentioned earlier in chapter 2.

4.2 Growth Voltage effects of Electrodeposition

Before applying the IPL, the electrodeposition parameters were studied to understand the growth of p-type CdTe vs n-type CdTe films. Whereas CSS commonly produces p-type conductivity because of Cd deficiencies in the film, low temperature techniques tend to create n-type CdTe with an excess of Cd.[257] The unique advantage of using low temperature electrodeposition is its ability to control the p or n type doping of the film by growth voltage (V_g) rather than temperature.[258] Altering the V_g results in changes to the Cd:Te ratio. At high V_g, excess Cd is present in the film, yielding n-type films. Meanwhile lower V_g values produce p-type films due to excess Te in the film. When

the Cd:Te ratio is 1:1 the film is considered to be stoichiometric and intrinsic. **Figure 4.1a** shows the XRD patterns of as-deposited CdTe grown at 1.451, 1.526, and 1.601 V. The films demonstrate a good match to the (111), (220), (311), and (400) crystalline planes of cubic CdTe (ICDD 01-015-0770). All the films demonstrated preferential orientation towards the (111) crystal plane. **Figure 4.1b** shows the intensity of the (111) reflection of CdTe vs. the V_g. As explained in Chapter 3, the intrinsic point where the material is stoichiometric and had the highest intensity for the (111) reflection was observed at 1.526 V.
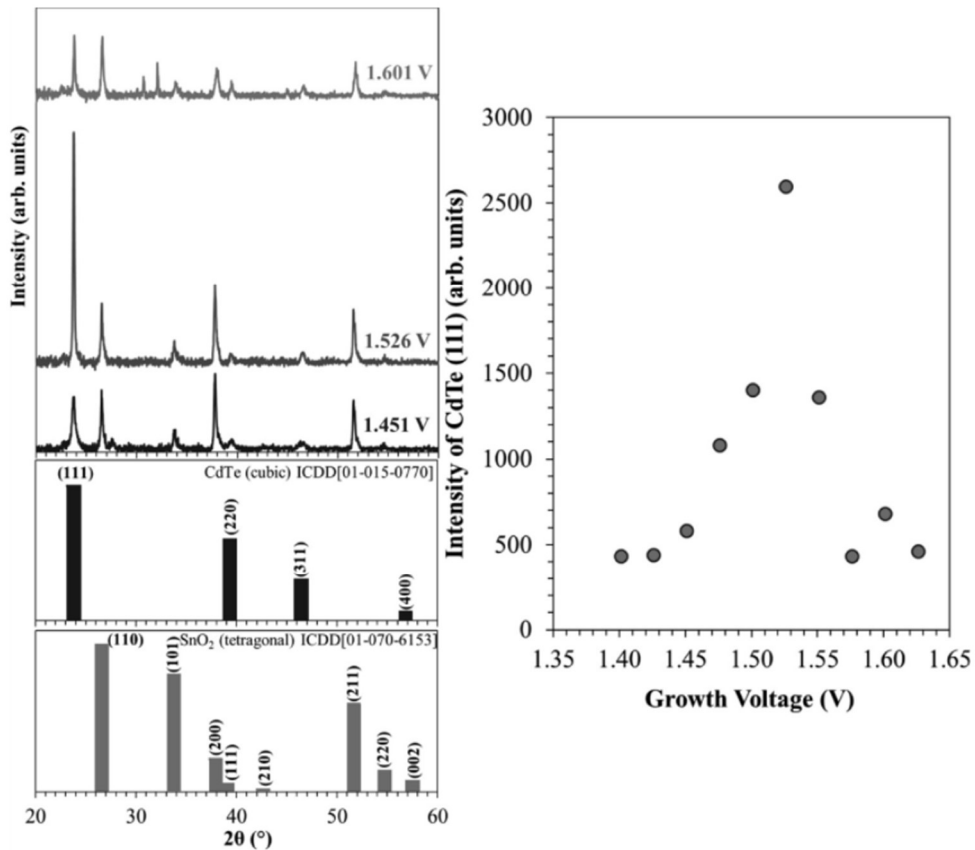
Figure 4.1. (a) XRD patterns of as-deposited CdTe at 1.451, 1.526, and 1.601 V. (b) Intensity of as-deposited CdTe (111) reflection vs. growth voltage, V_g. The XRD patterns were normalized to the SnO_2 reflection at 26.7° of the FTO substrate.

4.3 IPL Influence on CdTe Material Properties

The conductivity type of CdTe can change with thermal heat treatments as unreacted Cd and Te in the film form CdTe. Like in CSS, high temperatures can also form Cd vacancies, due to the higher vapor pressure of Cd compared to Te.[259] In addition, changes in the film orientation and morphology are also expected depending on the processing conditions. **Figure 4.2** and **Figure 4.3** show the XRD spectra of the as-deposited and IPL treated CdTe and a plot of the (111)IPL/(111)as-deposited ratio vs. the total energy input during IPL treatment, respectively. The number of pulses applied to the films was kept constant at 100, whereas the total energy input to the films was varied by changing the energy density (ED) of the light pulses.
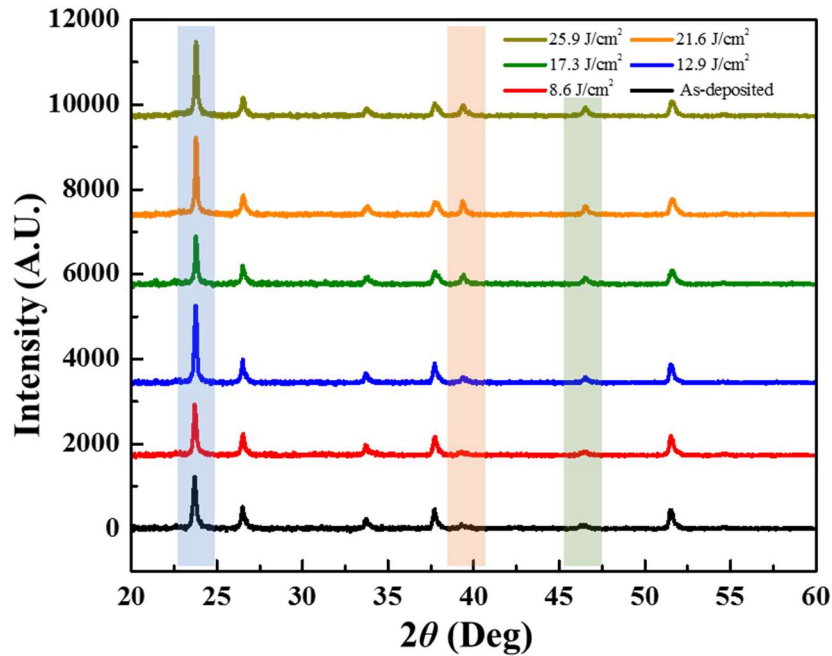
Figure 4.2. XRD spectra of the as-deposited and IPL treated films. The 111 reflection of CdTe is highlighted in blue, the 220 reflection of CdTe is highlighted in orange, and the

311 reflection of CdTe is highlighted in green. All remaining reflections are from the fluorinated-tin oxide (FTO) glass substrates.
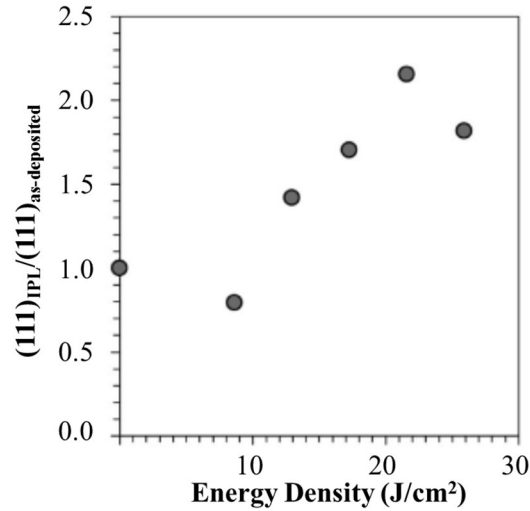
Figure 4.3. (111)IPL/(111)as-deposited ratio of CdTe vs. total energy input during the IPL treatment. The films were treated using 100 pulses of light with an energy density of 8.6, 12.9, 17.3, 21.6, and 25.9 J/cm^2.

The results showed that when pulses with an ED of 8.6 J/cm^2 were applied to the film the crystallinity of the films decreased slightly, indicating the temperature rise generated by the pulses was sufficient to begin the rearrangement of atoms in the film. As the ED of the pulses was increased, the film showed an increase in the intensity of the (111) reflection. The crystallinity of the CdTe increased, indicated by a decrease to the full width at half maximum (FWHM) values for the reflections treated with an ED of 21.6 J/cm^2. Increasing the ED of the pulses past 21.6 J/cm^2 resulted in a decline in the crystallinity. The decrease in crystallinity was an indication that the temperature in the films became high enough to initiate the loss of Cd or CdTe from the film. The IPL also created changes in the lattice parameter a of the films with the as-deposited films (6.479 Å) having the

highest lattice parameter, decreasing to 6.476 Å for pulses with an ED of 21.6 J/cm^2, and decreasing further to 6.472 Å for pulses with an ED of 25.9 J/cm^2. This reduction in a with increasing energy input indicates a relaxation of the stress within the lattice.

4.4 Optical Properties of IPL Treated CdTe

The lattice mismatch between FTO and CdTe prevented electrodeposited films from growing greater than 1 μm in thickness. This was detrimental to the solar harvesting of the CdTe films and showed in the transmittance spectra obtained with UV−Vis spectrometry **(Figure 4.4)**. There was a large amount of transmittance in the visible region of the 400-600 nm CdTe films. Device quality CdTe films are typically greater than 1 μm in thickness, in order for the films to efficiently absorb sun light. As mentioned earlier, this is one of the reasons CdS is effective in CdTe devices as it provides a buffer layer for the lattice mismatch. The optical bandgap (E_g) of the films was found by generating Tauc plots of $(\alpha h\nu)^2$ vs. $h\nu$ from the transmittance spectra. The as-deposited films showed a band gap of 1.47 eV which is customary for CdTe, and the band gap of the film sintered with 25.9 J/cm^2 pulses from the IPL decreased slightly to 1.46 eV. A benefit of the IPL sintered samples was a decrease in their transmittance in the visible light region. This could advance efforts of creating thinner CdTe devices with reduced material costs.
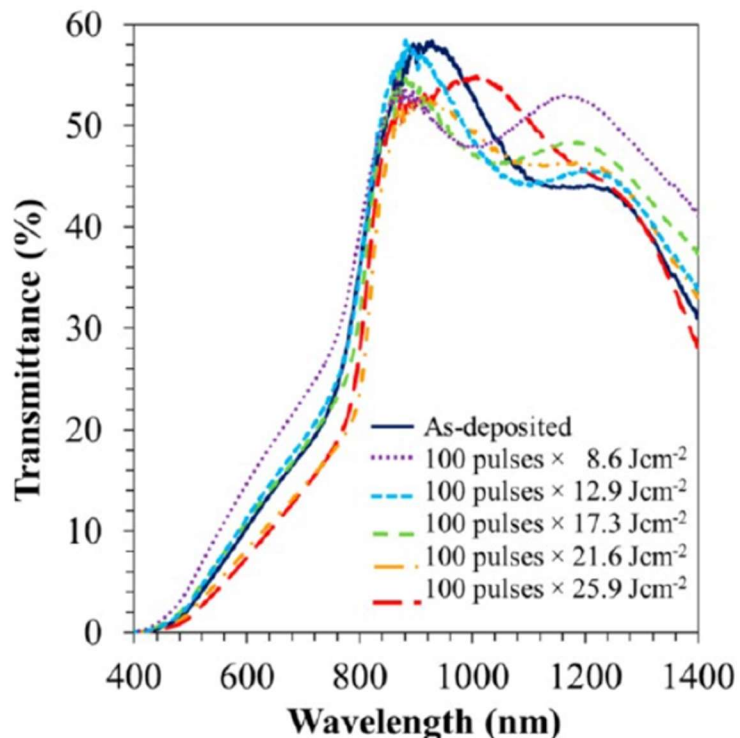
Figure 4.4. UV−Vis transmittance spectra of CdTe IPL treated without $CdCl_2$. The films were treated with a total energy input of 0 (i.e. as-deposited), 8.6, 12.9, 17.3, 21.6, and 25.9 J/cm^2.

4.5 Morphology Changes

Figure 4.5(a−c, g−i) shows the SEM topographical images of as-deposited and IPL-treated CdTe. As expected, the low temperature nature of the electrochemical deposition resulted in granular nanoparticle films. Upon IPL treatment, the surface of the particles appeared to become smoother and as the ED of the pulses was increased to 12.9 J/cm^2 particle growth and melting became more observable **(Figure 4.5c)**. Increasing the pulse output further to 17.3 J/cm^2, resulted in significant particle growth, as the smaller particles coalesced into particles with cross sections as large as 400 nm **(Figure 4.5g)**. Further increasing the ED to 21.6 J/cm^2 and 25.9 J/cm^2 produced an almost continuous

surface **(Figure 4.5h)** and the formation of particles as large as 1 μm **(Figure 4.5i)**, respectively. An increased surface roughness was observed in the IPL processed CdTe films. This also occurs when CdTe is thermally processed using a laser light source. This surface roughening phenomenon was found to be due to the loss of Cd during the heating process; resulting in a highly enriched Te surface.[260] This was confirmed in the XRD spectra, as the IPL-treated films with increased surface roughness displayed a decrease in the (111) reflection indicating the loss of material from the surface.
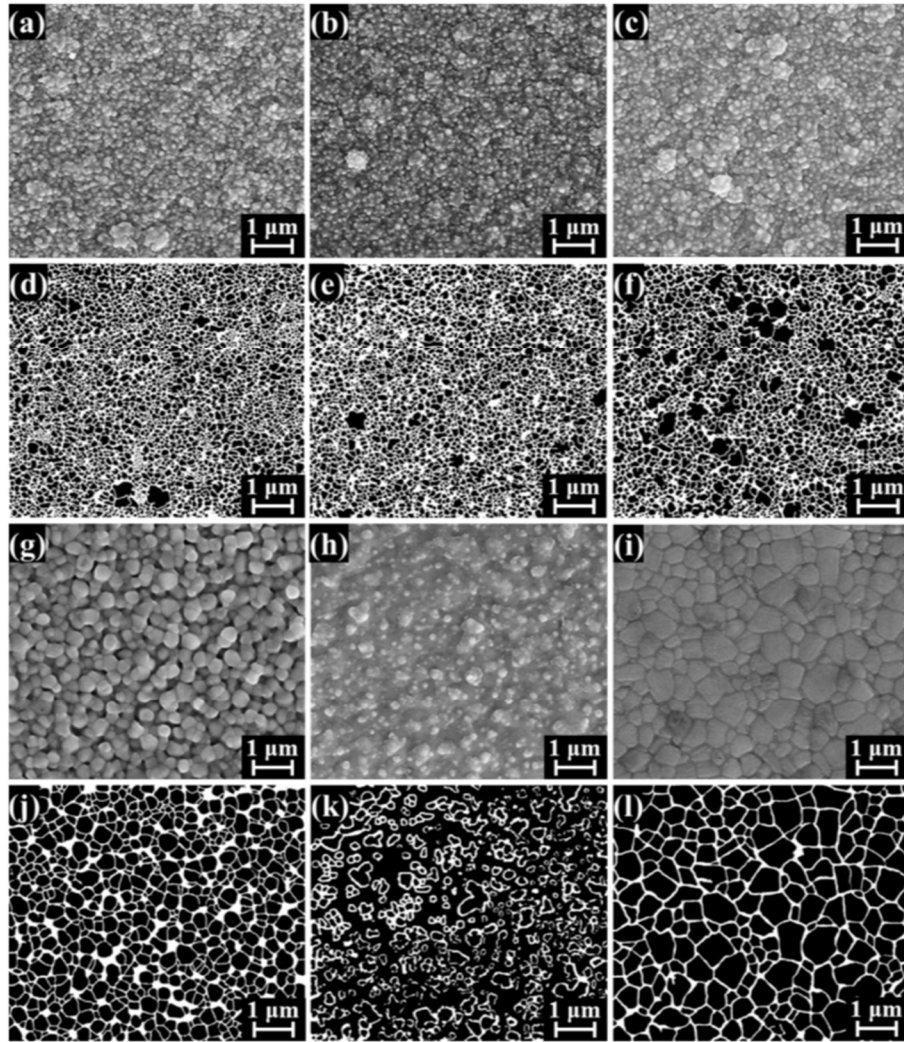
Figure 4.5. SEM and black and white topographical images of IPL-treated CdTe. The films were treated using 100 pulses of light with an energy density of (a, d) 0 (i.e., as-deposited), (b, e) 8.6, (c, f) 12.9, (g, j) 17.3, (h, k) 21.6, and (i, l) 25.9 J/cm^2.

A continuous film of CdTe processed by IPL after low temperature electrodeposition **(Figure 4.5h)** would be an are an important development for thin film solar cells. It would alleviate the formation of pin-holes in the structure and decrease grain boundary recombination sites. The presence of a continuous surface layer and reduction in pin-holes will help reduce the previously mentioned short circuiting and reproducibility problems experienced by ultrathin CdTe devices of thicknesses less than 1 μm. To observe

the reproducibility of this feature, experiments were repeated using 21.6 J/cm^2 pulses, but in this case, the number of pulses was varied from 80 to 90 and 110 pulses. The films topographical views are shown in the SEM images in **Figure 4.6**. The images confirm the reproducibility of this feature and its repeatability over a wide process window. These results demonstrate the potential for the IPL technology to be used to process large-area semiconductor thin films in short time frames suitable for manufacturing.
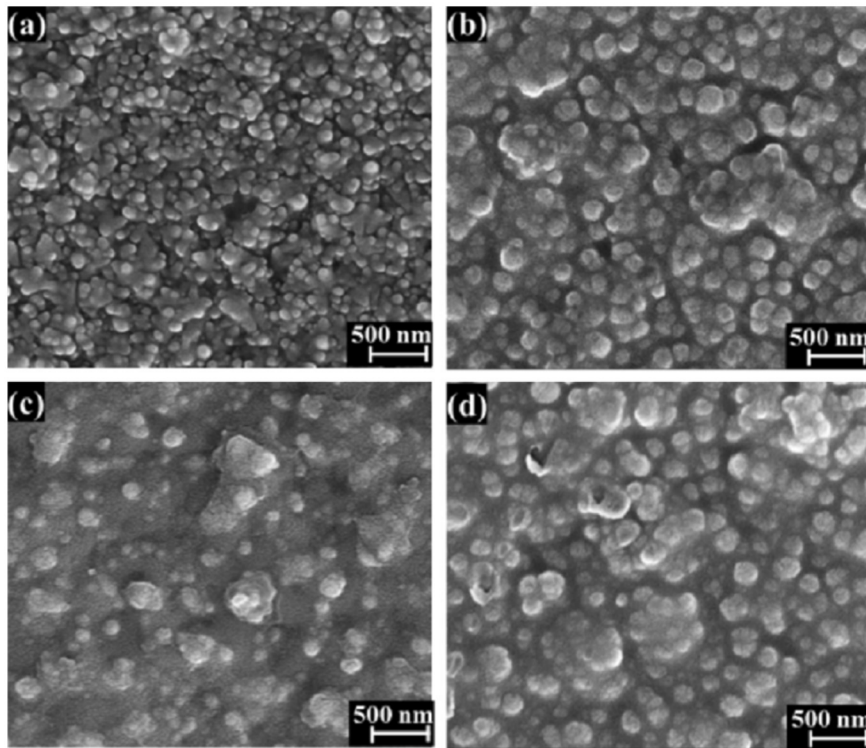
Figure 4.6. SEM topographical images of CdTe IPL treated using pulses of energy densities with 21.6 J/cm^2. The number of pulses applied was (a) 80, (b) 90, (c) 100 and (d) 110.

One of the concerns of using the IPL process, was the possible delamination of the films from the substrate during the densification. However, tape pull experiments did not show any decrease in the adhesion of the films to the substrate as none of the films could be removed. **Figure 4.7** shows the cross-sectional image of the CdTe-FTO substrate

interface after IPL treatment using 100 pulses with an ED of 21.6 J/cm^2. The image corroborates the assertion that delamination of the film does not occur because of stresses induced by the IPL treatment. Instead, the cross-section of the films showed a densification of the film at the air interface due to melting. The densification proceeded vertically down the film to the glass substrate with more defined CdTe particles located near the glass substrate. This demonstrated that the pulses of light induced a temperature gradient in the vertical direction of the film, and not in the lateral direction; with higher temperatures occurring closer to the surface and inducing melting.
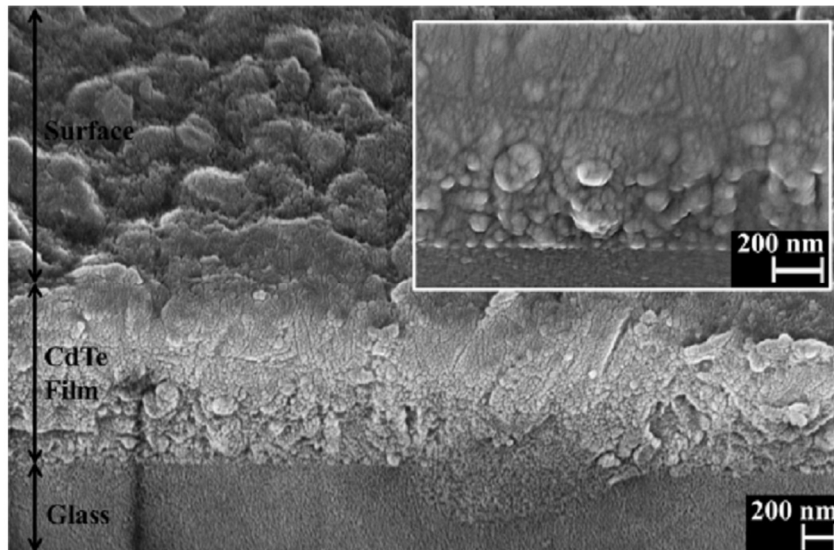
Figure 4.7. Cross-sectional SEM image of CdTe IPL treated using 100 pulses with an energy density of 21.6 J/cm^2 at a tilt of 45°. The inset shows a close up of the glass−CdTe interface.

4.7 CdTe Crystal Growth

During thermal processing, recrystallization is initially dominant followed by particle growth. However, recrystallization is inextricably linked to both the particle size and stress in the film. This is why CdTe films grown at high temperatures with CSS do not

always demonstrate changes to their large grains after treatment.[261] The low-temperature growth of electrochemical deposition, on the other hand, produces small particles under stress that are susceptible to thermal treatment. The average maximum and minimum Feret diameter calculated from the SEM images, with respect to the energy input during the IPL process is shown in **Figure 4.8**. During the IPL treatment, pulses with low ED's less than or equal to 12.9 J/cm^2 generated sufficient energy for the recrystallization process to begin **(Figure 4.5c)**. Under these conditions, a small degree of particle growth was also observed, where the smaller particles underwent solid state surface diffusion. The results showed that when the energy input exceeded 12.9 J/cm^2, a sharp increase in the particle size was observed as the particles began to melt **(Figure 4.5g)**. CdTe in its bulk form is known to have a melting point of approximately 1100 °C. Therefore, the reduced melting temperature of the small particle sized as-deposited films coupled with the high temperature rise induced by the IPL was paramount to the success of the melting and particle growth observed during IPL treatment.
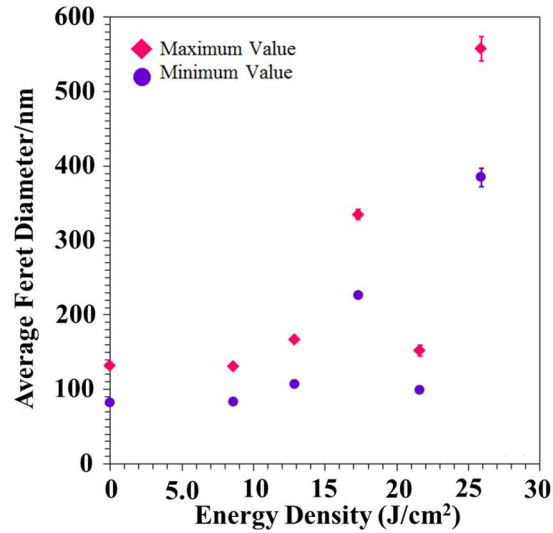
Figure 4.8. Average maximum and minimum Feret diameters vs. the total energy input during IPL treatment. Feret diameters were measured using the black and white images shown in Figure 4.4. The error bars were calculated using the standard error.

4.8 Recombination Sites Analysis

As mentioned in chapter 3, photoluminescence (PL) is a technique that can be used to analyze mid gap recombination sites. This characterization technique was used to compare the as-deposited films to the IPL treated films. **Figure 4.9** shows the room-temperature photoluminescence (PL) spectra for the as-deposited and IPL treated electro-chemically deposited CdTe films in the energy range of 1.0 to 1.9 eV. The signal observed for the as-deposited layer had a broad peak with a low intensity, indicating the presence of a large number of shallow donor and acceptor type defects in the material. These donor to acceptor like transitions produce photons less than the E_g which gives the broader signal seen in the PL spectra. For emissions greater than the E_g this is attributed to the existence of nanosized particles showing quantum confinement effects. As a result, the band to band

90

emissions showing the E_g are low, and both higher and lower energy photons than the E_g are emitted producing a weak and broad signal.

As the layers were treated with IPL pulse ED's increasing from 8.6 to 21.6 J/cm^2, the band-to-band emissions increased. The width of the peak (i.e., FWHM) was also reduced, showing the best results at treatments with 21.6 J/cm^2 **(Figure 4.9 inset)**. Photon emissions below the E_g were reduced, suggesting the reduction of donor and acceptor like defects in the material. Meanwhile, photons emitted with energies greater than the E_g decreased due to the coalescence of nano-sized particles into large grains, thereby reducing the quantum effects. Therefore, optimum IPL pulse ED for CdTe appeared to be close to 21.6 J/cm^2. Treatment with higher energy pulses (25.9 J/cm^2) displayed a reduction in band to band emissions reducing the peak intensity and a slight shift to higher energies. This indicated deterioration of the optical/electrical properties of the CdTe films.
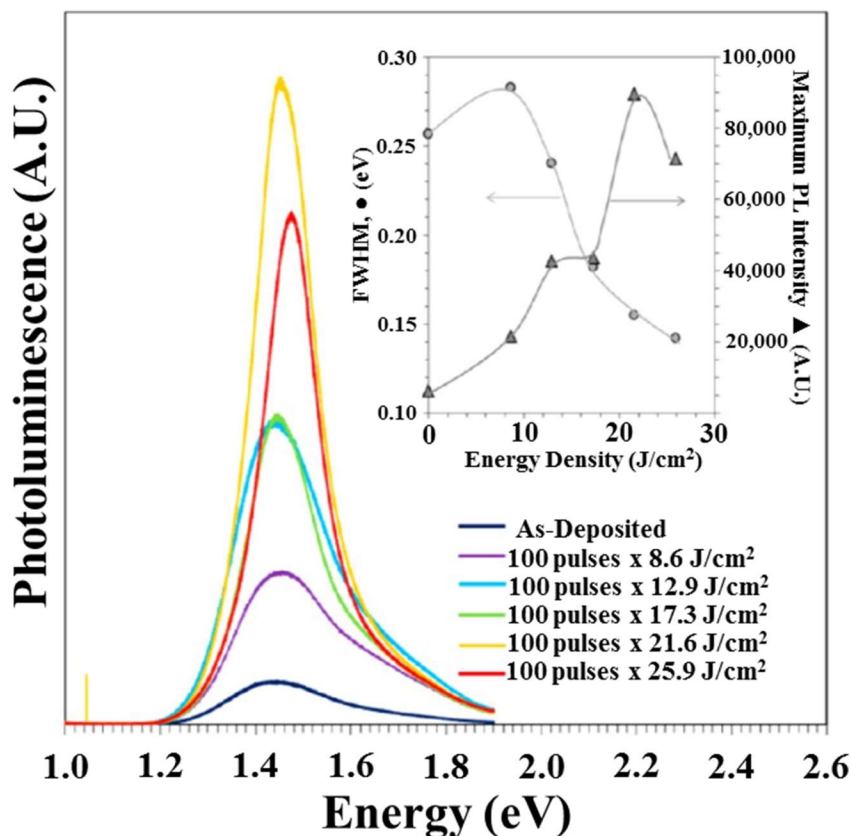
Figure 4.9. Room-temperature photoluminescence (PL) of the as-deposited and IPL treated films excited with a 632 nm laser. The inset shows the effect of the total energy input during the IPL treatment on the full width at half maximum (FWHM) of the PL peaks and the maximum intensity of the peaks.

4.9 Solar Energy Capabilities

Photoelectrochemical (PEC) measurements were conducted in order to elucidate the effect of the IPL treatment on the CdTe films. **Figure 4.10** shows the current density vs. potential (J−V) characteristics of an as-deposited and IPL treated film using 100 pulses with an ED of 21.6 J/cm². The J−V curves were measured under chopped illumination conditions to show the film under dark and light conditions during the linear voltammetry measurement. Both the as-deposited and IPL treated samples displayed cathodic

photocurrent confirming the p-type behavior of the films. As expected, the increased grain size improved crystallinity and reduced defect density of the IPL treated film resulting in a significant increase in photocurrent. The shape of the photocurrent transient was similar for both films, with an initial spike in photocurrent which rapidly decayed to steady state values. In many materials these spikes have been attributed to surface recombination as a result of the charging and discharging of surface states.[262-263]
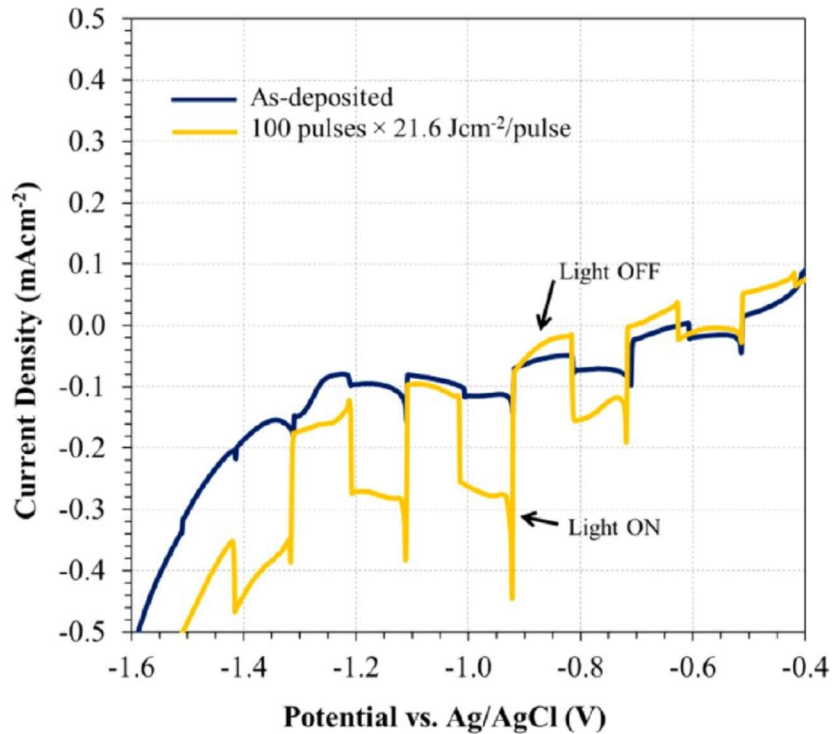
Figure 4.10. Chopped J−V measurements of the as-deposited and IPL treated CdTe films using 100 pulses with an energy density of 21.6 J/cm^2. The films were illuminated from the front side using AM 1.5 simulated light in an aqueous 0.1 M Na$_2$S solution using platinum as the counter electrode.

4.10 Conclusions

This was the first reported intense pulsed light treatment of CdTe thin films. The low temperature electrodeposition growth resulted in films consisting of nanoparticles,

with reduced melting point temperatures. In combination with the high temperature rise produced by the pulses of light, the lower melting temperature resulted in pores/voids being filled as well as enhanced grain growth. As a result, pin-holes and grain boundary recombination were diminished. Subsequently the fill factors of PV devices created using this technology are likely to be significantly increased. Unlike many conventional heating techniques, IPL irradiates the entire surface of the film and a temperature gradient is only expected in the vertical direction corresponding to the film depth, and not in the lateral direction. This phenomenon was demonstrated by film densification closer to surface. This also resulted in the surface particles showing significant lateral growth producing grains as large as 1 μm in less than 2 minutes, in addition to a reduction in gaps between particles. The fast processing times under atmospheric conditions without evidence of oxidation, demonstrated the suitability of the IPL to be used to thermally process semiconductors for PV devices.

CHAPTER 5

CdCl$_2$ TREATMENT OF CdTe SOLAR CELLS

5.1 Introduction

Despite creating low-temperature processed pin-hole free films using the IPL technology, another CdTe solar cell manufacturing problem remained unresolved: the high temperature processing involved in the CdCl$_2$ treatment. This is a technique that although not well understood by the community, is necessary in activating the junction in CdTe solar cells to produce high efficiencies devices.[52] An opportunity exists to perform this manufacturing step faster and with reduced costs associated with no longer operating a chlorine environment in high temperature furnaces.

5.2 IPL Processed CdCl$_2$ Grain Reorientation

One of the most common and simplest methods to apply CdCl$_2$ before heat treatment is to apply a saturated solution of CdCl$_2$ on the surface of the CdTe film to create a thick film. As discussed previously, the efficiency of the IPL process is based on the material's ability to absorb light. CdCl$_2$ is known to absorb UV light, therefore much of the energy required to heat the CdTe film will be absorbed by this layer.[264] This will result in the sintering of the CdCl$_2$, reducing the thermal treatment in the CdTe layer. Therefore, to counteract this effect, a thin coat of CdCl$_2$ was spin coated on to the surface prior to IPL. **Figure 5.0(i)** shows the effect of the total energy input during the IPL process on the (111)IPL/(111)as-deposited ratio. Meanwhile, **Table 5.1** Compares the 220 and 311 reflections of CdTe to 111 plane before and after CdCl$_2$ treatment.

Table 5.1 Comparison of the 220 and 311 reflections of CdTe to 111 plane before and after

CdCl$_2$ treatment

IPL Intensity (J/cm^2)	(220/111 IPL Treated)/ (220/111 As-Deposited)	(311/111 IPL Treated)/ (311/111 As-Deposited)
8.6	1.05	1.24
12.9	1.08	1.36
17.3	1.03	0.95
21.6	1.05	0.80
25.9	0.82	1.07
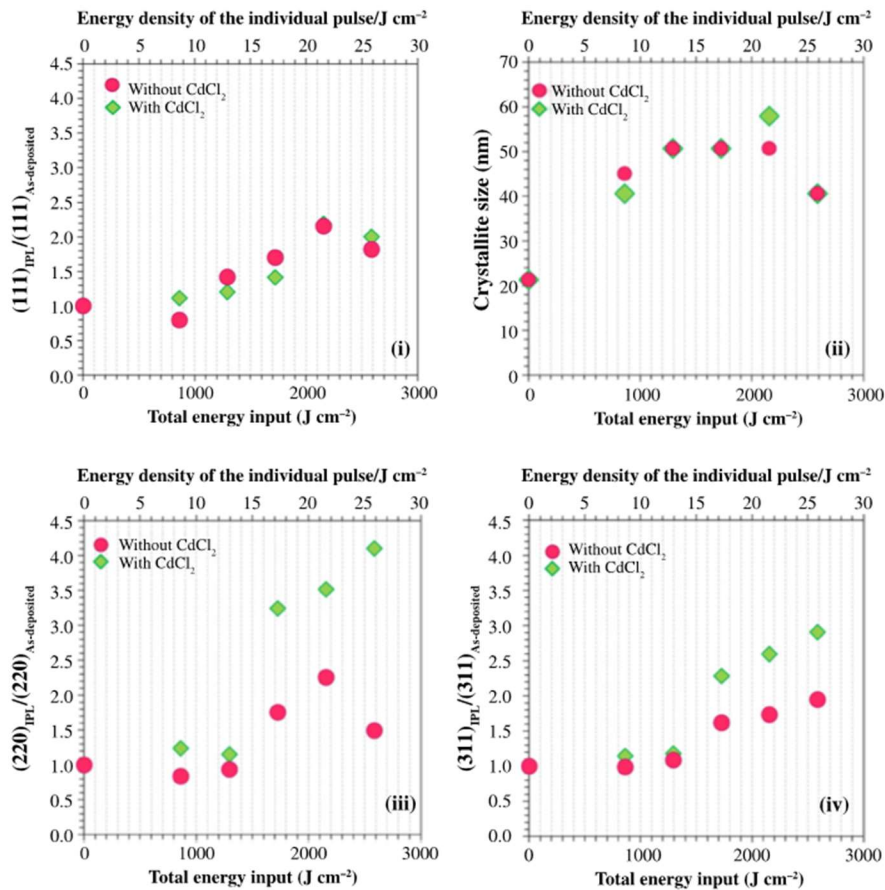
Fig. 5.1. (i) (111)IPL/(111)as-deposited ratio of CdTe (grown at 1.526 V) vs total energy from the IPL treatment. (ii) crystallite size vs total energy from the IPL treatment. (iii) (220)IPL/(220)as-deposited ratio and (iv) (311)IPL/(311)as-depsoited ratio. The results are shown for the CdTe IPL treated (•) without CdCl$_2$ and CdCl$_2$ and (◆) with CdCl$_2$. The

scale above the graph shows the energy density of each pulse. The scale below each graph

shows the total energy input after multiplying each pulse by its energy density.

$CdCl_2$ is believed to work as a ''fluxing'' agent on the surface of the particles,

leading to a reduction in the processing temperature needed to induce physical changes.[265]

In the IPL process, the pulse ED was not shifted to lower values to promote maximum

recrystallization when $CdCl_2$ was used. However, it was observed that while a pulse ED of

8.6 J/cm^2 induced disorder in the untreated films, the $CdCl_2$ treatment caused the

(111)IPL/(111)as-deposited ratio to remain above 1. This indicated the catalytic effect of

$CdCl_2$ in the re-crystallization process. $CdCl_2$ treatment has been known to induce a loss

of orientation in the (111) crystalline plane and induce random orientation showing other

increased CdTe related peaks. The CdTe films treated with $CdCl_2$ retained their preferential

orientation to the (111) crystalline plane until 100 pulses with an ED of 21.6 J/cm^2 was

used. After this point, the collapse of the (111) peak is shown by XRD results **(Figure**

5.1(i)). **Figure 5.1(ii)** shows the effect of energy input on the crystallite size for the $CdCl_2$

treated samples. A maximum crystallite size of 58 nm was found for the films treated with

a pulse ED of 21.6 J/cm^2.

Interestingly, the changes in the (220) and (311) orientations were drastically

different when $CdCl_2$ treatment was used (Figures 5.0(iii), (iv)). Without $CdCl_2$ on the

surface, the loss of Cd from CdTe takes place, resulting in a reduction to the intensity of

(111) and (220) peaks and minimal change to (311) peaks. The presence of $CdCl_2$ on the

surface prevents loss of Cd from CdTe layer, and acts as a fluxing agent or catalytic source,

causing reorientation. In the presence of $CdCl_2$, rapid growth of (220) and (311) peaks

occurred when the (111) peak started to collapse. At this point, the grains lost their

preferred orientation and showed a random nature. The grain boundaries entered a melt phase, resulting in a movement of the CdTe grains to a random structure as the film cooled. During this time grains can also coalesce easily across the liquid margins forming larger grains.

5.3 Morphology Changes

The reorientation of large grains resulting from IPL treatment should lead to a higher surface roughness. This is evident in **Figure 5.2** showing the SEM topographical changes of the CdTe thin films exposed to $CdCl_2$ after 100 pulses of ED 17.6, 21.6, and 25.9 J/cm^2. These films produced particles similar in shape, but larger in size compared to the uncoated films; however, the films appeared to be rougher. This structural reorganization often precedes a rise in grain size followed by a reorientation to the preferential (111) as more energy is delivered to the thin film.
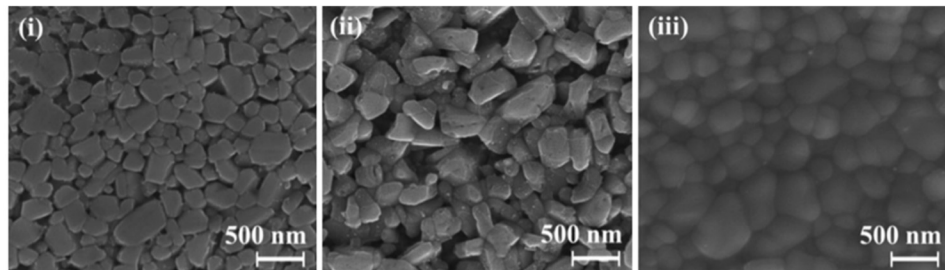
Fig. 5.2. SEM topographical images of IPL processed CdTe films treated with $CdCl_2$ for 100 pulses at varying ED of (i) 17.6 J/cm^2, (ii) 21.6 J/cm^2, and (iii) 25.9 J/cm^2

Figure 5.3 shows optical microscope images of the uncoated and $CdCl_2$-treated films. When 100 pulses of light with an ED of 12.9 J/cm^2 were applied, no structural changes were observed. Upon application of pulses with an ED of 25.9 J/cm^2, significant macroscopic structures were observable in the films treated with $CdCl_2$. The structures in the film appeared to have a centralized point, which propagated out to make islands greater

than 200 nm in width **(Figure 5.3(vi))**. This phenomenon, termed ''explosive crystallization'' has been observed in the laser and IPL treatment of amorphous silicon.[266-267] Exposure to the irradiation source causes the amorphous region to melt and recrystallize. If the latent heat released during crystallization is large enough, adjacent amorphous regions will also melt and recrystallize. In this manner, crystallization in the film accelerates until an autocatalytic process occurs. The propagation front will cease when the rate of heat dissipation (influenced by the thermal conductivity of the material and irradiation time) exceeds the latent heat released during crystallization process.[268] In the CdTe films, it would appear that these explosive fronts originate from areas of densely coated $CdCl_2$ on the surface. However, this requires further investigation to confirm. Increasing the ED of the pulses further, resulted in the propagation waves being less observable. However, the large discrete islands remained. In addition, delamination of the films appears to have been observed.
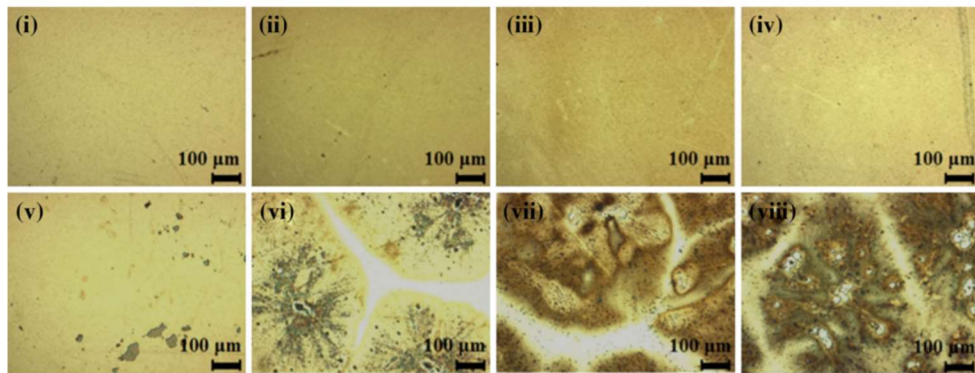
Fig. 5.3. Optical microscope images of CdTe IPL treated (i, ii, iii, iv) without $CdCl_2$, (v, vi, vii, viii) with $CdCl_2$ on the film. The films were treated with an energy density of (i, v) 12.9, (ii, vi) 17.3, (iii, vii) 21.6, and (iv, viii) 25.9 J/cm^2

5.4 CdCl$_2$ Treatment Using Different Electrodeposition Precursors

The enhancements seen in device efficiencies using the CdCl$_2$ treatment have inspired the development of new electrodeposition precursors. To assess the potential of the different precursors, photoluminescence (PL) was utilized to investigate the mid band gap recombination centers before and after CdCl$_2$ treatment. When the CdTe surface is excited by laser light during PL measurements, electrons are continuously pumped from the valence band to the conduction band. Electrons captured by electron traps are incapable of making the full transition from the conduction band back to the valence band and therefore emit photons with different energies that create additional PL peaks along with the peak associated with the E$_g$. The PL spectra recorded at 80 K for the thin film CdTe layers (labeled S1–S4) grown from different precursors are shown in **Figure 5.4**. Five main PL peaks exist with the trap states labeled T1–T4 and the band gap labeled E$_g$. This is summarized in **Table 5.1** with the energy values corresponding to the maxima of these peaks together with their approximate energy spread. The peak positions at 80 K can be converted into room temperature values when necessary, using the rate of change of E$_g$:

$$(dE_g/dT) = -4.2 \times 10^{-4} \text{ eV/K}$$
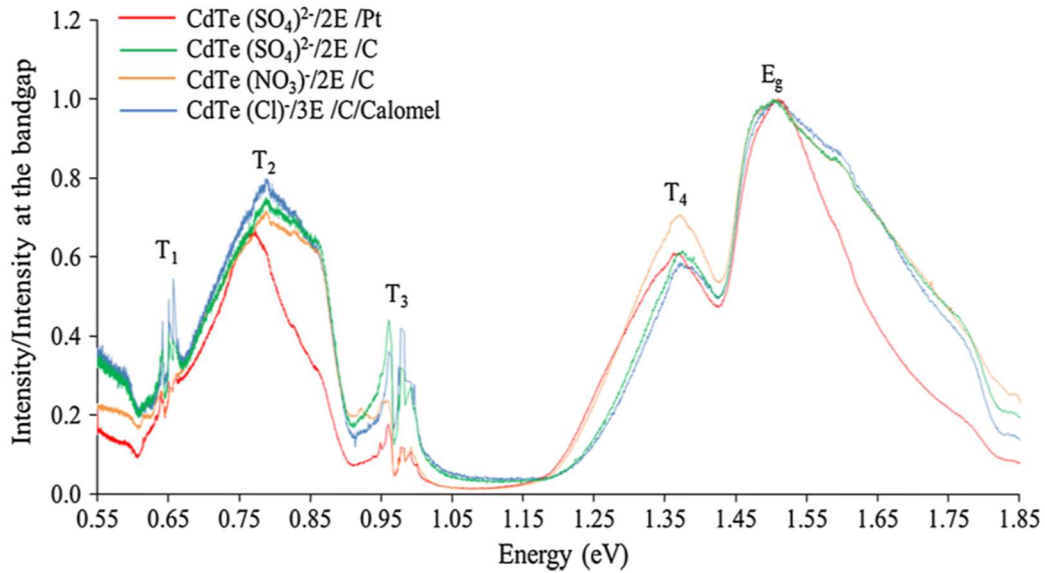
Figure 5.4. Typical photoluminescence spectra recorded at 80 K for four as-deposited CdTe layers using different Cd-precursors (Cd- sulfate, nitrate and chloride). The intensity of peaks are normalized to that of the bandgap emission peak, E_g

The maxima of the peaks appeared at 0.66, 0.79, 0.97, 1.37 and 1.50 eV at 80 K, indicating at least four deep defect bands situated in the explored energy range, below the conduction band minimum. The peak at 1.50 eV contained the E_g of CdTe and was broader due to various energy transitions on both sides of the E_g of the material. The emissions greater than E_g may arise due to the presence of a sulfur-rich $CdS_xTe_{(1-x)}$ alloy at the CdS/CdTe interface, or due to quantum effects. As previously mentioned, electroplated CdTe material consists of grains in the nano-scale that can exhibit quantum effects in electron transitions creating photons with energy greater than the bandgap. Conversely, emissions with energies less than E_g can arise due to donor-to-acceptor type transitions, involving shallow energy levels, within the bandgap. They can also come from Te-rich $CdSxTe_{(1-x)}$ alloys present on the CdTe side of CdS/CdTe interface that have lower E_g than that of CdTe due to ''bandgap bowing effect''.[269]

Table 5.1 Summary of electron trap levels (T1–T4) and the energy bandgap peak (E_g) observed at 80 K for the four as-deposited CdTe layers. 2E and 3E stands for 2-electrode and conventional 3-electrode systems respectively. Pt and C show the materials used for anodes. Growth conditions of the samples are as follows: S1: 1.0 M $CdSO_4$, low con. of TeO_2, pH = 2.00, temp. = 85 °C, growth voltage = 2.238 V; S2: 1.0 M $CdSO_4$, low con. of TeO_2, pH = 2.00, temp. = 85 °C, growth voltage = 1.576 V; S3: 1.0 M $CdNO_3$, low con. of TeO_2, pH = 2.00, temp. = 85 °C, growth voltage = 1.253 V; S4: 1.0 M $CdCl_2$, low con. of TeO_2, pH = 2.00, temp. = 70 °C, growth voltage = 0.693 V

Sample ID	Material	$T_1 \pm 0.02$ (eV)	$T_2 \pm 0.15$ (eV)	$T_3 \pm 0.03$ (eV)	$T_4 \pm 0.08$ (eV)	E_g peak (eV)
S1	CdTe (SO_4^{2-})/2E/Pt	0.66	0.77	0.97	1.36	1.51
S2	CdTe (SO_4^{2-})/2E/C	0.66	0.79	0.97	1.37	1.50
S3	CdTe (NO_3^-)/2E/C	0.66	0.79	0.98	1.37	1.50
S4	CdTe (Cl^-)/3E/C	0.66	0.79	0.98	1.37	1.50

The trap levels T1, T3 and T4 were narrow, but the electron traps at 0.79 eV (T2) were spread over $\pm$ 0.15 eV. This is problematic as T2 is situated right in the middle of the bandgap, meaning these defects are very effective in the recombination process and cause detrimental effects in PV performance. These defects have been so disastrous in device efficiencies, that they have been nicknamed ''killer centers'' in II–VI semiconductors.[270] A good solar energy material should be free of these mid-gap killer centers. Although the defect level T4 also has a broader distribution, the probability of recombination of charge carriers through this level is very low due to its closeness to the valence band.

5.4.1 CdSO₄ Precursor Recombination Sites after CdCl₂ Treatment

Figure 5.5 shows the PL spectra recorded for the CdTe layer (S1) electroplated using the $CdSO_4$ precursor 2-electrode system with a Pt anode. The three spectra correspond to the as-deposited and $CdCl_2$ treated CdTe in two steps. The observed peak details are summarized in **Table 5.2**, and a few major changes were clear from these results.

The two defect levels at T1 and T3 completely disappeared during the $CdCl_2$ treatment. The broad distribution of T2 narrowed and the T4 level reduced, indicating the drastic removal of defects. The broad peak E_g consisted of several transitions, but sharpened after $CdCl_2$ treatment producing 1.47 eV for the E_g of the material. This indicated the elimination of higher energy emissions of small crystallites after growing into large CdTe grains.
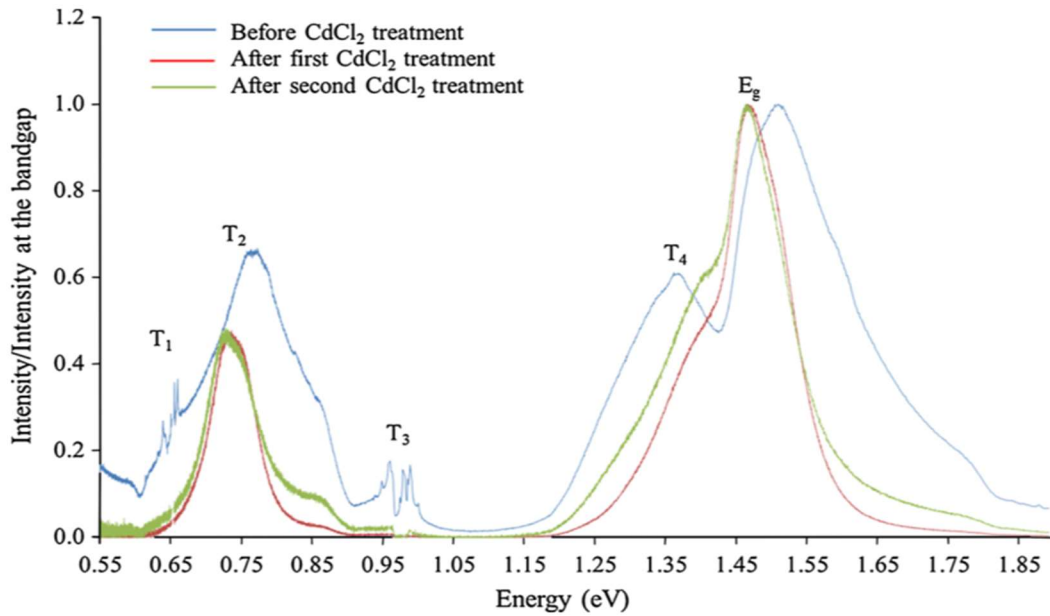
Figure 5.5. Photoluminescence spectra for as-deposited, first $CdCl_2$ treated and second $CdCl_2$-treated CdTe layers, electroplated using $CdSO_4$ precursor in 2-electrode system with Pt anode (S1)

Table 5.2 Summary of electron traps at 80 K for CdTe layers electroplated from $CdSO_4$ precursor using 2-electrode system with Pt anode (S1)

Energy (eV)	T_1	T_2	T_3	T_4	E_g
As deposited	0.66	0.77	0.97	1.36	1.51
$CdCl_2$—step 1	–	0.73	–	1.39	1.47
$CdCl_2$—step 2	–	0.73	–	1.39	1.47

Figure 5.6 and **Table 5.3** show the PL spectra and details of the defects for the CdTe layer (S2) grown from $CdSO_4$ precursor using the 2-electrode system with graphite (C) anode. The same four defect levels were observed, and the disappearance of T1 was clear after $CdCl_2$ treatment. Reduction of T3 was evident but the defects were not completely removed. Although the intensities of T2 and T4 peaks reduced, their distribution did not decrease. Unlike the CdTe made with the $CdSO_4$ precursor and 2-electrode system with the Pt anode, the layers were still full of defects even after $CdCl_2$ treatment.
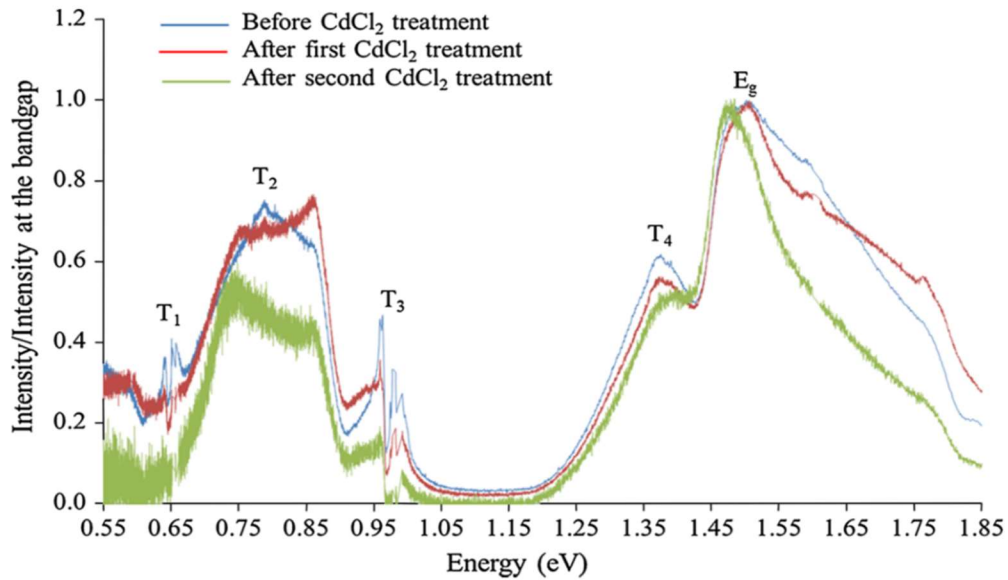
Figure 5.6. Photoluminescence spectra for as-deposited, first $CdCl_2$ treated and second $CdCl_2$-treated CdTe layers electroplated using $CdSO_4$ precursor in 2-electrode system with graphite anode (S2)

Table 5.3 Summary of electron traps at 80 K for CdTe layers electrodeposited from $CdSO_4$ precursor using 2-electrode system with graphite (C) anode (S2)

Energy (eV)	T_1	T_2	T_3	T_4	E_g
CdTe—As deposited	0.66	0.79	0.97	1.37	1.50
CdTe–$CdCl_2$—step 1	–	0.76	0.97	1.37	1.50
CdTe–$CdCl_2$—step 2	–	0.74	0.97	1.38	1.48

5.4.2 Cd(NO₃)₂ Precursor Recombination Sites after CdCl₂ Treatment

Figure 5.7 and **Table 5.4** present the PL spectra and the peak details for the CdTe layers (S3) grown with $Cd(NO_3)_2$ precursor, using a 2-electrode system with graphite anode. The most striking observation was that the peak positions were in general very similar to those grown using the $CdSO_4$ precursor. After $CdCl_2$ treatment, T1 completely disappeared and, T3 peak still remained. Although the intensity of T2 reduced considerably, the distribution remained the same. Intensity of T4 first reduced after the first $CdCl_2$ treatment and then increased after the second $CdCl_2$ treatment. The E_g peak sharpened and moved closer to 1.48 eV after $CdCl_2$ treatment, reducing the high energy PL emissions.
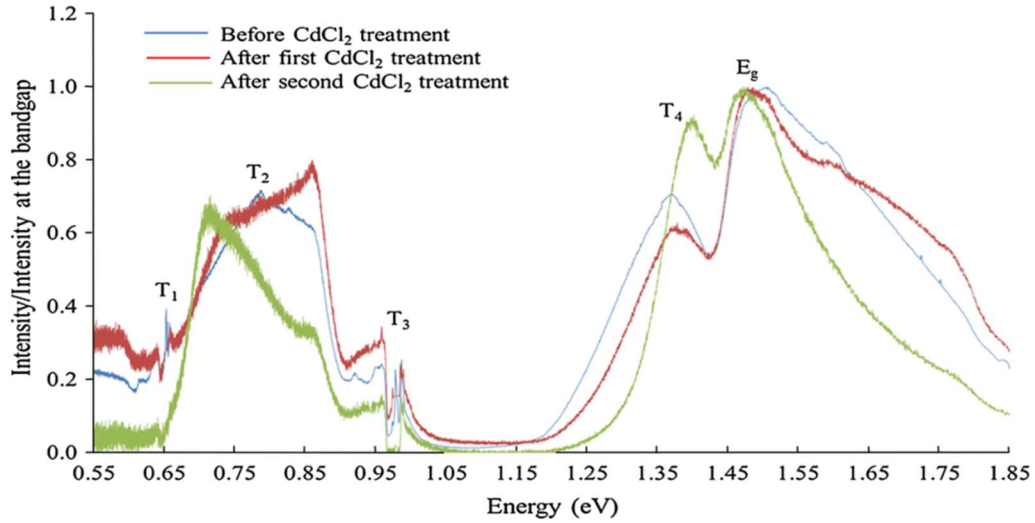
Figure 5.7. Photoluminescence spectra for as-deposited, first $CdCl_2$-treated and second $CdCl_2$-treated CdTe layers electroplated, using $Cd(NO_3)_2$ precursor in 2-electrode system with graphite anode (S3)

Table 5.4 Details of PL peaks at 80 K for CdTe layers electroplated using $Cd(NO_3)_2$ precursor and 2-electrode system with graphite anode (S3)

Energy (eV)	T_1	T_2	T_3	T_4	E_g
CdTe—As deposited	0.66	0.79	0.98	1.37	1.50
CdTe–$CdCl_2$—step 1	0.66	0.86	0.99	1.38	1.48
CdTe–$CdCl_2$—step 2	–	0.71	0.99	1.40	1.48

5.4.3 $CdCl_2$ Precursor Recombination Sites after $CdCl_2$ Treatment

Figure 5.8 and **Table 5.5** showed similar results for CdTe layers (S4) grown using the $CdCl_2$ precursor, in a 3-electrode system with a graphite anode. All five peaks in the as-deposited layer were identical in energy position compared to those of CdTe grown from the other precursors, but showed drastic changes after $CdCl_2$ treatment. The T1 and T3 defect levels were completely eliminated during the $CdCl_2$ treatment and the T2 energy

106

distribution reduced considerably from 0.34 to 0.09 eV. Another drastic reduction of the intensity of T4 and sharpening of the E_g peak were excellent results to observe. In particular, the drastic reduction of the mid-gap killer centers at T2 is good news for photovoltaic devices. Electrodepositing using the $CdCl_2$ precursor provided a built-in $CdCl_2$ treatment while the materials were grown. Therefore, the effect of the $CdCl_2$ treatment should be the highest in this material and indeed the changes at the band-to-band transitions were drastic and noteworthy. Formation of highly crystalline CdTe with low defects, in the presence of Cl$^-$ was clear from these results. It seems that Cl$^-$ ions are acting as a fluxing agent for the growth of CdTe with large crystals and low defect density. Nano-scale crystals coalesced to form a few micron size grains after $CdCl_2$ treatment.
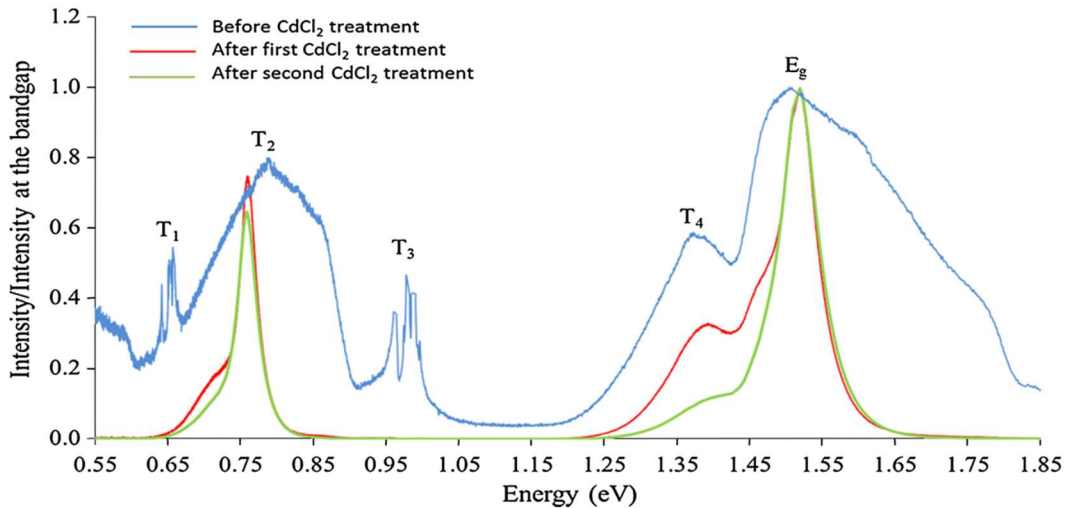
Figure 5.8. Photoluminescence spectra for as-deposited, first $CdCl_2$-treated and second $CdCl_2$-treated CdTe layers (S4) electroplated using $CdCl_2$ precursor and 3-electrode system with graphite anode and saturated calomel reference electrode

Table 5.5 Details of PL peaks at 80 K for CdTe layers (S4) electrodeposited using $CdCl_2$ precursor and 3-electrode system with graphite anode and saturated calomel reference electrode

Energy (eV)	T_1	T_2	T_3	T_4	E_g
As deposited	0.66	0.79	0.98	1.37	1.50
$CdCl_2$—step 1	–	0.76	–	1.39	1.51
$CdCl_2$—step 2	–	0.76	–	1.39	1.51

5.4.4 Summary of CdTe made with different precursors after CdCl₂ Treatment

A summary of the PL studies on all four CdTe layers is given in **Table 5.6**. Trap levels for both the as-deposited and $CdCl_2$ treated (after second stage) samples are shown for comparison. Four trap levels were observed for all the CdTe layers in the explored energy range. When heat treated in the presence of $CdCl_2$, T1 and T3 completely reduced in some samples, while others showed a considerable reduction. T2 was the main defects band present in the middle of the bandgap and was distributed over a wide energy range of 0.30 eV. Because of its broad distribution, it could include a large number of PL peaks arising from closely situated defect levels forming a broad PL band. These are the most detrimental defects for PV action, with the highest probability of recombination process. T4 appeared at (1.36–1.40) eV, with varying intensity after $CdCl_2$ treatment. $CdCl_2$ treatment effectively removes radiative defects clearing the bandgap of CdTe.

Table 5.6 Summary of observed PL peaks at 80 K for four different CdTe layers electrodeposited from three different Cd-precursors (Cd- sulfate, nitrate and chloride)

Growth details	Material condition	T_1 (eV)	T_2 (eV)	T_3 (eV)	T_4 (eV)	E_g (eV)
S1—CdTe–$(SO_4{}^{2-})$/2E/Pt	As-deposited	0.66	0.77	0.97	1.36	1.51
	CdCl$_2$ treated	–	0.73	–	1.39	1.47
S2—CdTe–$(SO_4{}^{2-})$/2E/C	As-deposited	0.66	0.79	0.97	1.37	1.50
	CdCl$_2$ treated	–	0.74	0.97	1.38	1.48
S3—CdTe–$(NO_3{}^-)$/2E/C	As-deposited	0.66	0.79	0.98	1.37	1.50
	CdCl$_2$ treated	–	0.71	0.99	1.40	1.48
S4—CdTe–(Cl^-)/3E/C	As-deposited	0.66	0.79	0.98	1.37	1.50
	CdCl$_2$ treated	–	0.76	–	1.39	1.51

These results are comparable to bulk CdTe wafers. The defect level positions in bulk CdTe have been observed by many techniques such as Schottky barrier measurements, Deep Level Transient Spectroscopy, Ballistic Electron Emission Microscopy and PL.[270-271] The three defect levels reported for bulk CdTe; 0.65, 0.73 and 0.96 eV below the CB coincide with T1, T2 and T3 levels observed for electrodeposited CdTe. Although the T4 seems to be introduced and enhanced by CdCl$_2$ heat treatment. After CdCl$_2$ treatment, the E_g of the CdTe layer corresponded to (1.36–1.42) eV at room temperature, which was also similar to that of bulk CdTe.

5.5 Working Mechanism of CdCl$_2$ Treatment

Following the success of using the CdCl$_2$ treatment on CdTe made with different precursors, the question still remained as to why the CdCl$_2$ treatment works. Understanding this mechanism would advance the manufacturing capabilities of the CdTe solar cell. To begin to understand this treatment, bulk purchased CdTe wafers were processed using the CdCl$_2$ treatment and PL measurements were carried out to examine the trap states. **Figure 5.9** shows the PL spectra recorded for the CdTe wafer before and after the CdCl$_2$ treatment. The as-received material showed two sharp peaks corresponding to the 0.76 eV (T2) mid-

gap defects and the 1.52 eV (E_g) peak of the material. These were identical to the two peaks, T2 and E_g observed for thin films of CdTe. After $CdCl_2$ treatment, the T2 level shows slight broadening and an additional peak at 1.39 eV (T4) appears, showing that these changes are induced by the $CdCl_2$ treatment on the surface layer.
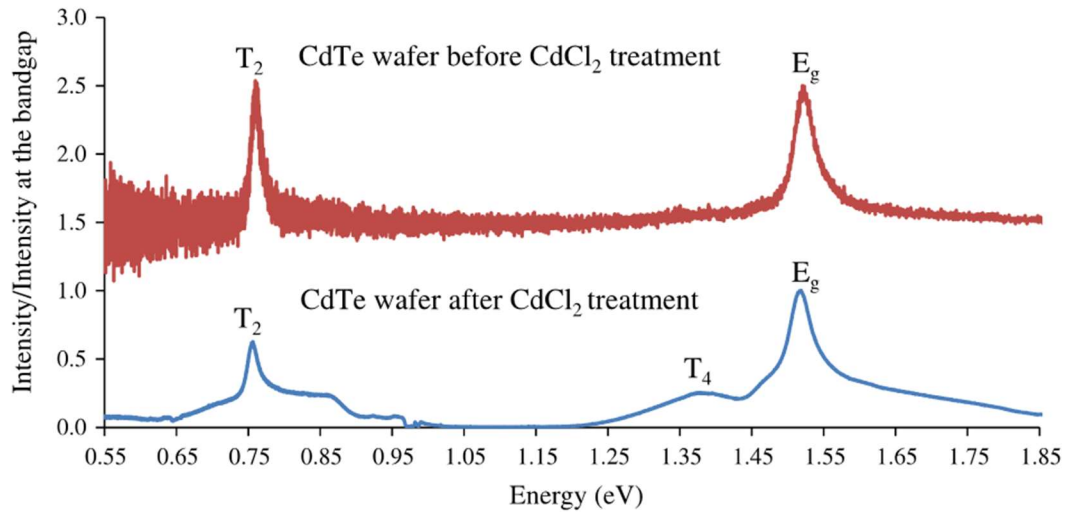
Figure 5.9. Photoluminescence spectra recorded before and after $CdCl_2$ treatment, for bulk CdTe wafers purchased from University Wafers Company. These wafers were produced using a melt-growth technique

A review by Fernandez on PL and cathodoluminescence (CL) also summarized the increase of this particular level upon $CdCl_2$ treatment. Hernandez-Fenollosa et al. showed from their PL studies, that the 1.36 eV level rapidly increased during HCl treatment in the presence of oxygen.[272] This information is extremely important in understanding what happens during this key processing step. The conclusion is that this additional defect level, T4 emerges due to Cd-richness or the incorporation of Cl in CdTe in the presence of oxygen. This PL observation is also very similar to the CL work reported by Mazzamuto et al.[273] These authors reported the development of this peak at 1.39 eV occurred when the Freon ($CHFC_{l2}$) gas pressure in the heating chamber was gradually increased during the

heat treatment of close space sublimation (CSS) grown CdTe thin films. Since there was no additional Cd involved in this treatment, Cd-richness can be ruled out with confidence. This provides us a firm conclusion of the origin of this defect at 1.39 eV (T4), below the CB edge. It shows that Cl interacts with the CdTe lattice, forming a defect level at 1.39 eV which is very close to the valence band. This level therefore, can act as a shallow acceptor in CdTe, increasing the acceptor concentration within the material. It also helps to better explain Cl as a dopant in CdTe solar cells. At the ppm level, when Cl displaces Te atoms in the lattice, it is a well-known donor in CdTe.[270] However, when the Cl concentration is high as in the case of CdCl$_2$ treatment, and interacts with the CdTe layer, it produces an acceptor like defect at 1.39 eV (T4), acting as a p-type dopant in CdTe. The presence of oxygen seems to catalyse this interaction.[272] These results show that defects present in CdTe are common for several different CdTe materials produced with different conditions. The heat treatment in the presence of CdCl$_2$ turns the material into electronic grade layers with only two or three deep defect levels present in them. Earlier work by Dharmadasa et al. used XPS to identify the T2 trap state as being dominant for Te-rich layers while the T3 and T4 were dominant for Cd-rich CdTe layers.[274]

In Te-rich surfaces, defects (T2) in the mid-bandgap are dominant, and in Cd-rich surfaces, defects in lower half of the bandgap (T3 and T4) are dominant. Results summarized in **Table 5.6** clearly show that CdCl$_2$ treatment removes the trap levels at T1 and T3, and drastically reduces the wide distribution of T2 to a narrow distribution level. These are the defect levels situated towards the middle of the bandgap and are related to the Te-richness of CdTe materials. Of the two elements, Cd and Te in CdTe, Te is the easiest element to discharge first and deposit during electroplating (E^o for Te is +0.593 V,

and E^o for Cd is -0.403 V with respect to hydrogen reference electrode). Therefore, Te can be precipitated within the layer or form a thin layer of Cd_xTeO_y on the surface.[275-278] Hence, most of the as-deposited CdTe layers have Te-rich nature and therefore T1 and T2 trap levels are dominant. However, when these layers are heat treated in the presence of $CdCl_2$ on the surface, excess Te converts into useful CdTe phase improving the composition towards stoichiometric CdTe layers.[279]

$$\text{Excess Te} + CdCl_2 \rightarrow CdTe + 2(Cl^-)$$
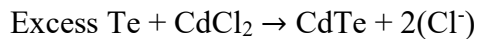
The presence of Cl^- in this process also helps in recrystallization and doping of the CdTe. In fact, the $CdCl_2$ treatment converts Te-richness of the initial CdTe layer into Cd-richness, and also reduces defects at T1 and T2. This produces a CdTe layer with a fairly clean band gap without defects in the mid-gap. The same process increases the band-to-band transitions of electrons, as a result of removal of mid-gap defect levels producing a better solar energy material.

5.6 Conclusions

Chapter 5 documents the structural transition taking place in electrodeposited CdTe layers throughout the IPL initiated $CdCl_2$ treatment. During IPL treatment without $CdCl_2$, grains grow gradually keeping the (111) preferred orientation. At a threshold total energy input, variant on the ED, XRD peaks reduced in intensity indicating deterioration of crystallinity most probably due to loss of Cd from the CdTe film. In the presence of $CdCl_2$, however, the situation was different. At early stages of IPL treatment, crystallinity improved, keeping the (111) preferred orientation. At a total energy input threshold, the layer became randomly oriented, but crystal grains grow continuously. These grains are

randomly oriented showing all three CdTe peaks with comparable intensities. The PL results presented in this chapter helped draw the following important conclusions:

(1) All four CdTe layers electroplated using sulfate, nitrate and chloride of cadmium, precursors exhibit four electron traps (T1, T2, T3 and T4) situated at similar energy positions.

(2) After $CdCl_2$ treatment, T1, T2 and T3 are completely annealed-out or show considerable reduction in concentration. This reduction was a positive effect for device performance.

(3) $CdCl_2$ treatment drastically reduced the mid-gap killer centers situated at the T2 level. Wide defects distribution (*0.30 eV) reduced to a narrow defect band (*0.09 eV) and the intensity also reduced by considerable amounts. This will have a drastic and positive effect on improvement of solar cell performance by reducing recombination of photogenerated charge carriers.

(4) The two defect levels T1 and T2, situated in the mid-gap are closely related to Te-richness in CdTe layers. The $CdCl_2$ treatment converts the Te-richness towards Cd-richness, reducing precipitated Te, and drastically removing mid-gap defects.

(5) Out of all four CdTe layers studied in this work, the material grown using the $CdCl_2$ precursor seems to produce a better material with a cleaner bandgap. This material is comparable to bulk CdTe wafers in terms of defect levels.

CHAPTER 6

IPL SINTERING OF METHYLAMMONIUM LEAD TRIIODIDE PEROVSKITE

6.1 Introduction

As previously mentioned, the PSC is in need of a faster thermal heat processing technique that can grow crystal grains without sacrificing the integrity of the film. Perovskite layers are typically heated on a hot plate to thermally anneal the layer to reduce grain boundaries and enlarge crystal size. The resulting films are in the tetragonal crystal structure of $CH_3NH_3PbI_3$ perovskites.[138] Poor film surface coverage is common in this formation.[26] The gaps within the perovskite film cause lower shunt resistance and lower short circuit current densities when the hole-transport layer is in direct contact with the electron-transport layer.[26, 280] This has spurred research attempts to densify the morphology of the perovskite layer to prevent shunting pathways and improve the fill factor and reproducibility of perovskite solar cells.[281] Research has shown that increasing the annealing temperature leads to an increase in the efficiency of the perovskite solar cell until 150 °C. At this temperature, the perovskite begins to decompose into PbI_2.[86]

The advantageous short time scale of IPL processing would be ideal for manufacturing perovskite solar cells without degradation and possibly allow for higher temperature processing in short bursts. The two areas of concern with the IPL method are the high heats that will result in the films and the exposure to UV, both with the potential to destroy the $CH_3NH_3PbI_3$ thin films. In this chapter, the effects of the IPL on the

CH$_3$NH$_3$PbI$_3$ perovskite layer **(Figure 6.1)** will be discussed as a new thermal processing

technique that can be applied to the roll-to-roll manufacturing of PSCs.
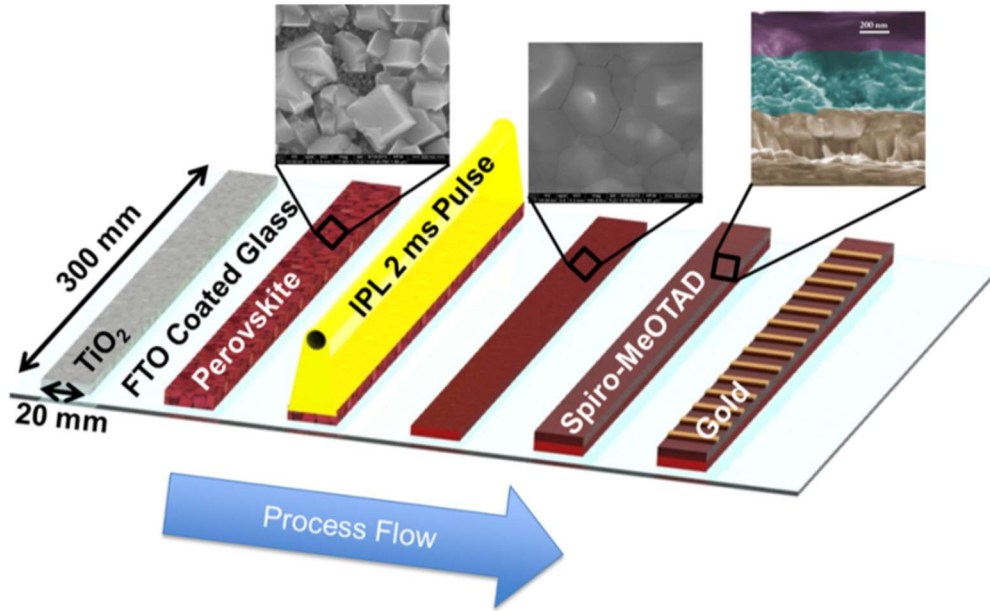
Figure 6.1. Scale-up for a perovskite solar cell based on roll-to-roll processing detailing

each part of production: the as-deposited perovskite, the sintered perovskite, and a cross

section of the completed device. The IPL sintering mechanism is deployed to create a faster

continuous assembly line.

6.2 Sintering of CH$_3$NH$_3$PbI$_3$ Perovskite

Perovskite solar cell devices were fabricated using a sequential approach detailed

in chapter 3. The device consisted of a 50 nm TiO$_2$ hole-blocking layer, a 150−250 nm

mesoporous TiO$_2$ electron-transport layer with CH$_3$NH$_3$PbI$_3$ perovskite crystals filling the

pores, a 150 nm layer of hole-transport layer spiro-OMeTAD, and an 80 nm layer of gold

on top of the hole-transport material to make a contact. The device structure is shown in

Figure 6.2.
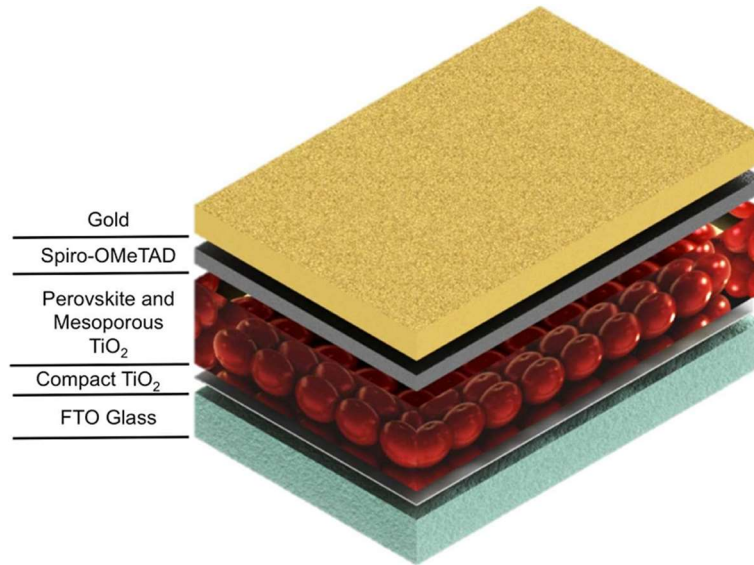
Figure 6.2. Device architecture of the perovskite solar cell (glass/FTO/bl-TiO$_2$/mp-TiO$_2$-perovskite nanocomposite layer/Spiro-OMeTAD/Gold).

Intense pulsed light was applied to as-deposited perovskite films using varying energy densities at 2 ms pulse times. The SEM images of the IPL-treated films in **Figure 6.3** showed that higher energy pulses increased the crystallite size and started to sinter the films. This was the first reported sintering of CH$_3$NH$_3$PbI$_3$ perovskite. **Figure 6.3** shows the transition of cubical particles into large dense particles. Very little change appears in the surface morphology at 1000 J/pulse **(Figure 6.3b)**. At 1250 and 1500 J/pulse (**Figure 6.3c,d**, respectively), the films began to consolidate, and the surface coverage improved. At 1750 J/pulse **(Figure 6.3e)**, necking of the particles was shown, and the perovskite began to sinter together. Necking between contacting particles is an obvious aspect of sintering as mentioned in chapter 1. Volume conservation and surface energy minimization drive this initial stage of sintering. Surface transport processes produce neck growth without a change in particle spacing (no shrinkage or densification) due to mass flow originating and terminating at the particle surface. Within the surface transport processing

domain, surface diffusion and evaporation-condensation are the two most important contributors. Surface diffusion dominates in the low-temperature sintering regime whereas evaporation-condensation dominates in the sintering of low-stability metals like lead and lead-based compounds. This suggests that evaporation condensation is controlling the initial sintering stage shown in **Figure 6.3e**.
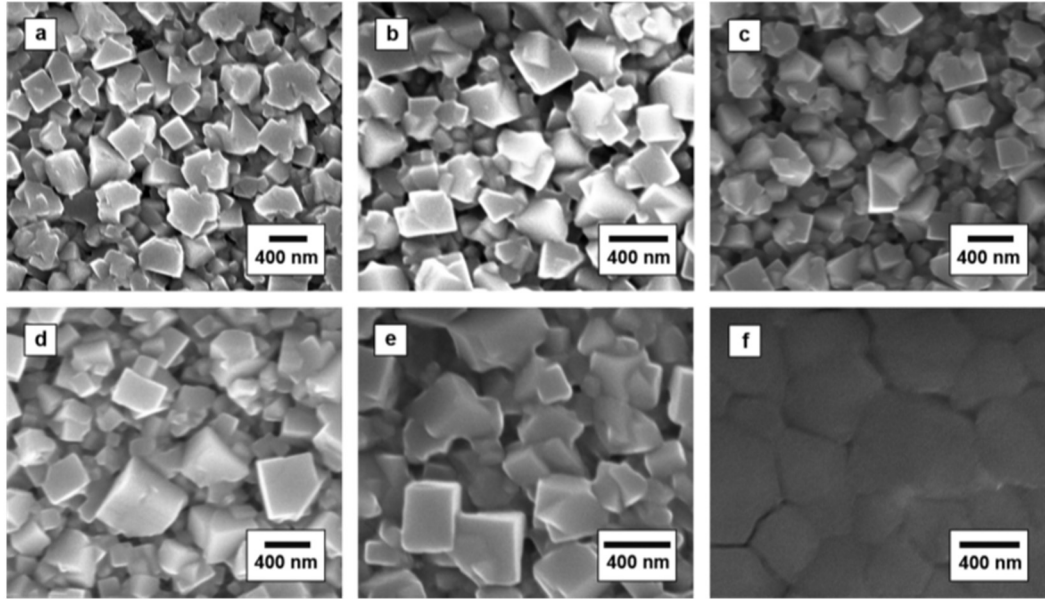
Figure 6.3. Top view SEM images of perovskite films (a) without IPL exposure, and after a 2 ms pulse of IPL exposure at (b) 1000, (c) 1250, (d) 1500, (e) 1750, and (f) 2000 J/pulse.

Evaporation-condensation sintering leads to the repositioning of atoms located on the particle surface without densification. Evaporation occurs from a surface and transports across the pore space, leading to condensation on a nearby surface. The net result over time is a reduction in the total surface area as bonds grow between touching particles. During this time, there is no change in the distance between the particle centers. Halides like the iodide found in the perovskites studied in this chapter have been added to tungsten, steels, and titanium dioxide to initiate evaporation-condensation sintering.[282-283] This was also seen in the sintering of zirconium oxide in which sintering in air was dominated by bulk

transport processes giving densification, while sintering in an environment with hydrochloric acid shifted the dominant sintering mechanism to evaporation-condensation.[284] Neck growth occurs in evaporation-condensation sintering until the surface energy, dihedral angle, and grain boundary energy attain a force equilibrium defined as[282]:

$$\gamma_{SS} = 2\gamma_{SV}\cos\frac{\varphi}{2}$$

Where γ_{SS} is the grain boundary energy, γ_{SV} is the solid-vapor surface energy, and φ is the dihedral angle.

The most radical change to the surface morphology was seen at 2000 J/pulse **(Figure 6.3f)**, in which the perovskite crystals increased in size and sintered together to form a dense layer. Prior to this research, densification of this magnitude was only achieved by using an extra solvent extraction treatment like diethyl ether or using a less scalable chemical vapor deposition process.[27, 285] This is the first time a rapid heat treatment has been shown to deliver such a radical change to surface coverage. Previously, Snaith et al. researched the effect of using a flash annealing step from 100 to 130 °C with a hot plate. They were able to create large crystal sizes and increased current density. However, the surface coverage was negatively impacted by the transition.[286]

For densification to occur, the mass must originate from the interior of the particle and deposit at the necking area. Bulk transport processes enabling this include volume diffusion, grain boundary diffusion, plastic flow, and viscous flow. Viscous flow is primarily reserved for amorphous materials such as polymers and glasses, so this can be ignored. Plastic flow may also be ignored as it becomes inactive when the shear stress declines and falls below the flow stress of the material during necking growth. Of the two

118

remaining processes, volume diffusion is unlikely as it is a slow process and the sintering of the perovskites occurred in 2 ms. This leaves grain boundary diffusion as the likely mechanism existing during the densification process.

In grain boundary diffusion, mass is removed along the grain boundary and redeposited at the sinter bond. The interparticle grain boundaries, and internal grain boundaries in the particles act as vacancy annihilation sites by processes of slip and rotation. As the sintering progresses, transport takes place between the pores via the grain boundaries, leading to pore coarsening. This occurs when the grain boundary is an inefficient vacancy sink late in the sintering process and the solid structure becomes so strong that it resists further densification.[287]

6.3 Heat Transport Within the Perovskite Layer

The key to this transformation is the rapid heat treatment at short incremental pulses. Dharmadasa et al. showed that it was feasible to heat CdS to temperatures >700 °C during a single pulse.[288] Using a similar energy density and the same equipment, it is conceivable for the perovskite to experience similar if not greater temperatures. $CH_3NH_3PbI_3$ perovskite ($E_g \sim 1.6$ eV) is known for its high light absorption properties and

absorbs more of the visible spectrum than the larger band gap semiconductor CdS ($E_g \sim$

2.42 eV). With a lower band gap, $CH_3NH_3PbI_3$ perovskite will absorb more light from the IPL spectrum than cadmium sulfide, causing a larger number of phonons to be generated and dissipated throughout the material as heat. The IPL enables the perovskite to enter high temperatures significantly exceeding 150 °C without having the time to degrade.

The thermal diffusivity (D) of a thin film is the ratio of the thermal conductivity (κ = 0.005 W/cm K), to the volumetric heat capacity ($\rho C_p = 1.28$ J/(cm^{3}K)) and is a measure

of how fast heat will move through a film. For the $CH_3NH_3PbI_3$ thin film, this is 0.0039

cm^2/s.[289] At a pulse duration of 2 ms, the diffusion length $(2(Dt)0.5)$ of the film is 56 μm,

which is significantly larger than the 300 nm thickness of the film. This would suggest a

very fast thermal diffusion through the film. The response of the film on the glass substrate

to the IPL pulse was accomplished using the finite element analysis (FEA) method.

An FEA model was used to understand the temperature profile of the film as

exposed to the varying energy densities used in this study. The $CH_3NH_3PbI_3$ thin films

absorbed 92% of the energy delivered by the pulses as measured using UV−vis

spectrometry. The pulses from the lower energy input of 1000 J increased the temperature

of the films to a maximum of nearly 400 °C and falling to under 150 °C in less than 5 ms.

The higher energy input of 2000 J reached a temperature slightly higher than 750 °C, and

the temperature of the film remained above 150 °C for almost 20 ms **(Figure 6.4)**. Although

all of the energy intensities managed to lift the temperature of the film over the maximum

of 150 °C, only the higher temperatures at prolonged duration managed to sinter the

$CH_3NH_3PbI_3$.
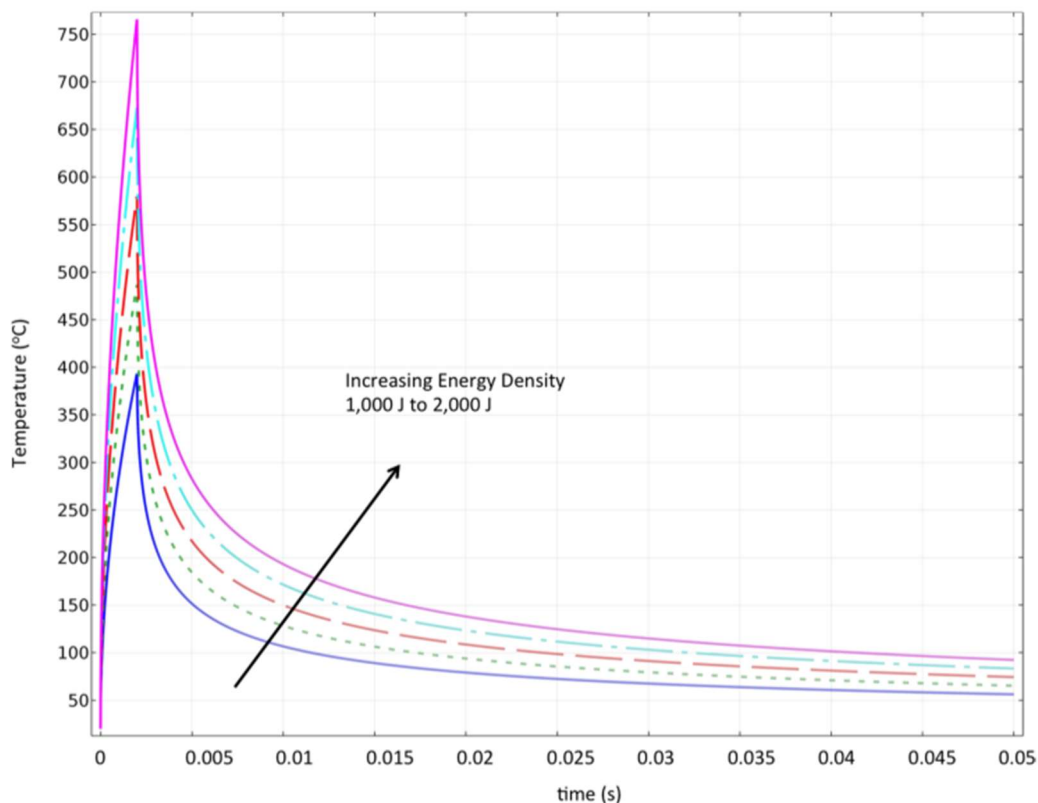
Figure 6.4. Temperature profiles as calculated using COMSOL finite element analysis of the $CH_3NH_3PbI_3$ thin film over time after being subjected to pulse intensities of 1000, 1250, 1500, 1750, and 2000 J.

6.4 Changes in the Crystal Structure of the $CH_3NH_3PbI_3$ after IPL

It is critical that the perovskite structure remains intact for the duration of the rapid high-temperature pulses to enable high-efficiency devices. To verify that no structural changes were occurring, XRD patterns were used to analyze the crystal structures of $CH_3NH_3PbI_3$ deposited on a glass slide and processed via the hot plate annealing as well as by the IPL process. **Figure 6.5** shows a side-by-side comparison of the XRD pattern of the perovskite solar cells under the two annealing methods. The IPL samples have a higher degree of crystallinity shown by their more intense peaks and more importantly have the same pattern as the hot plate annealed samples. The IPL-sintered samples do not show

121

peaks signifying a decomposition to lead iodide. Furthermore, the diffraction peaks from the (110) planes of the tetragonal I4/mcm phase (β phase) of $CH_3NH_3PbI_3$ were observed at $2\theta = 14.08°$ (d ≈ 6.26 Å), along with peaks at $2\theta = 28.36°$, 42.60°, and 58.82° due to the (220), (330), and (440) diffractions, respectively.[290] Photoluminescence of the as-deposited perovskite and IPL-processed perovskite in the inset of **Figure 6.6** also provided evidence of the perovskite structure remaining intact after sintering, and these yielded a band gap of 1.62 eV which is in agreement with previously reported values.[291]
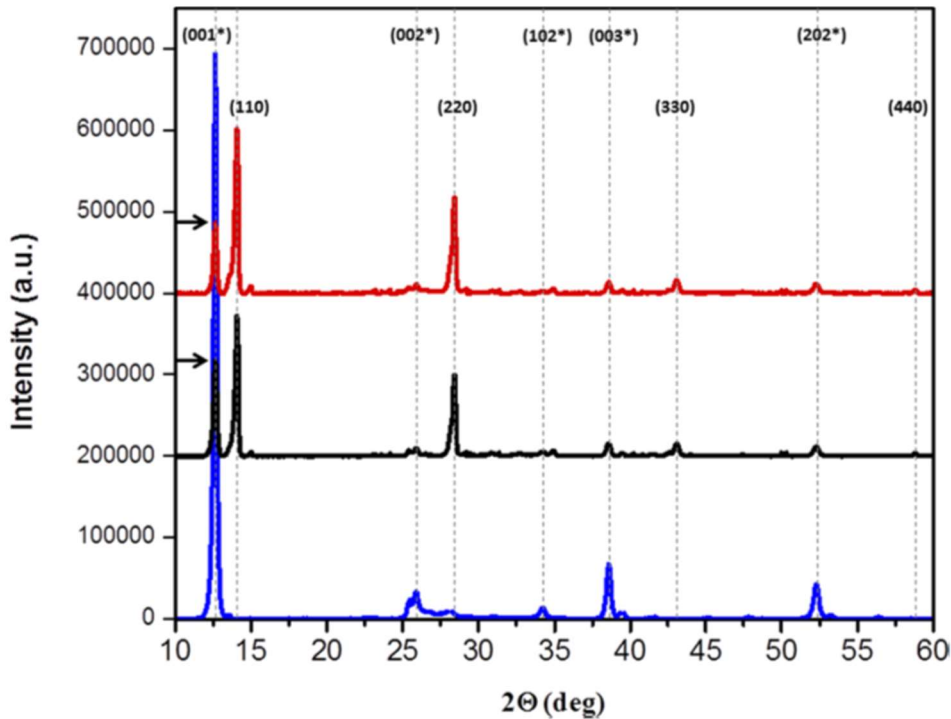
Figure 6.5. X-ray diffraction of hot-plate-annealed perovskite (black), IPL-sintered perovskite (red), and lead iodide (blue). Indices with * indicate lead iodide peaks, and the others are $CH_3NH_3PbI_3$. Arrows represent height of (001) lead iodide peak in hot-plate-annealed and IPL-sintered perovskite samples.
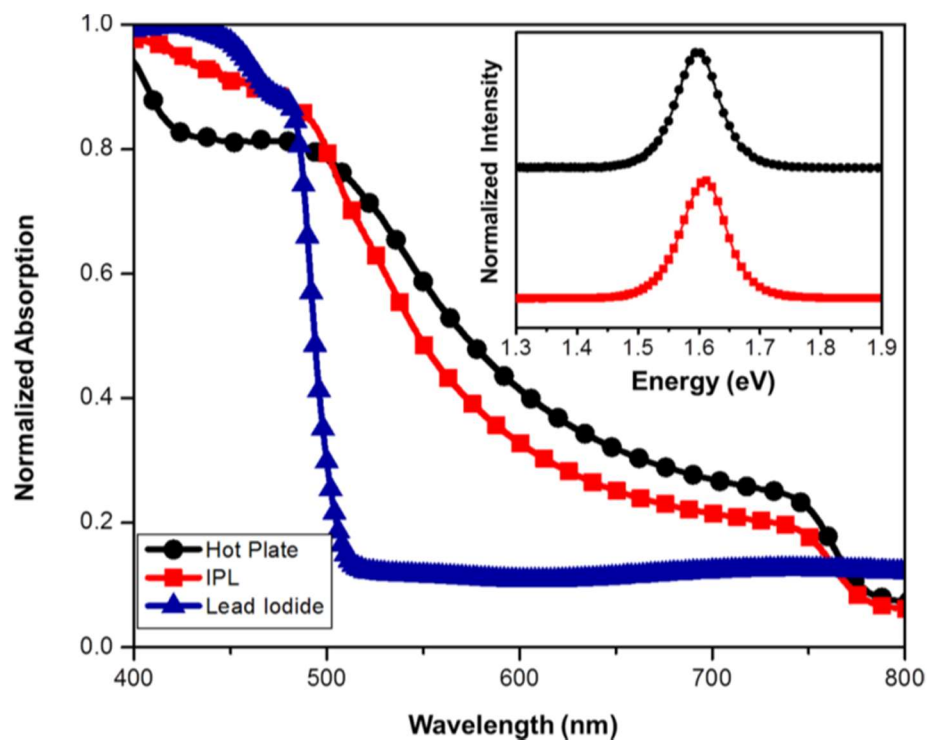
Figure 6.6. UV−Vis comparison of hot plate annealed perovskite, IPL- sintered perovskite, and lead iodide. Inset image is the photoluminescence of hot plate annealed perovskite and IPL-sintered perovskite.

6.5 Enhanced Electron Transport from Superior Pore Filling of Mesoporous ETM

To create the larger and less porous morphologies, the IPL process sintered the particles together and filled in any voids in the film. This was evident from the cross-sectional SEM images **(Figure 6.7)** that detailed a thinning of the perovskite layer during the IPL process. The pictures also illustrated that the IPL-sintered samples had a smoother surface compared to the sample annealed on a hot plate and greater pore filling of the $CH_3NH_3PbI_3$ into the TiO_2 mesoporous layer. It should also be noted that the pore filling of the hot-plate-processed samples was limited, which is detrimental to cell performance. The smoother surface of the spiro-OMeTAD should make a better contact with the evaporated gold cathode and improve the performance of the solar cell by decreasing series

resistance. Greater pore filling has been shown to be an important factor to control the completeness of perovskite coverage on the TiO_2 nanoparticles and reduce recombination rates.[292] Lower recombination rates improve the charge transport rates and collection efficiencies of the solar cells. UV−Vis spectroscopy data shown in **Figure 6.6** provides further evidence of a thinning of the perovskite layer. The IPL-treated samples are less absorptive compared to the hot plate treated samples. More importantly, the UV−Vis data supports the assertion that PbI_2, a known byproduct of the decomposition of $CH_3NH_3PbI_3$, was not being created during the IPL process. PbI_2 UV−Vis spectra show a significant decrease in absorption at 500 nm, which was not seen in the IPL-treated perovskite samples.
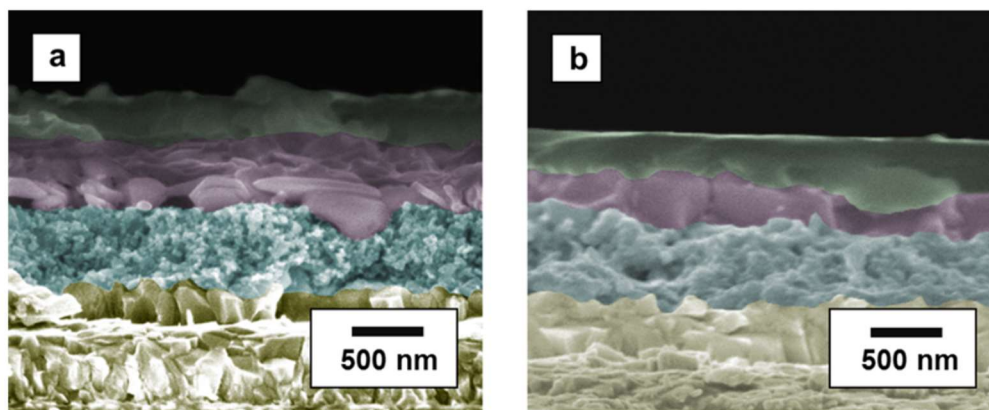
Figure 6.7. SEM cross-sectional images of perovskite after (a) hot plate annealing and (b) IPL sintering. The colors green, magenta, cyan, and yellow correspond to spiro-OMeTAD, perovskite, TiO_2, and FTO, respectively.

6.6 Electronic Properties of IPL Processed PSCs

With XRD and SEM evidence suggesting higher crystalline perovskite film formation using the IPL, the optoelectronic properties suggest that the IPL should have an improved performance over the thermally annealed cells. IPL processed PSCs were

fabricated and tested using an AM 1.5 solar simulator. The JV curve in **Figure 6.8** depicts the best performance of the IPL solar cells created. A comparison of the average performances of the IPL-processed and hot-plate- processed solar cells from the same batch is shown in **Table 6.1**. The IPL-processed solar cells have a higher current density, open circuit voltage, and fill factor than the PSCs annealed using the conventional hot plate method. Additionally, the IPL samples have less variability.
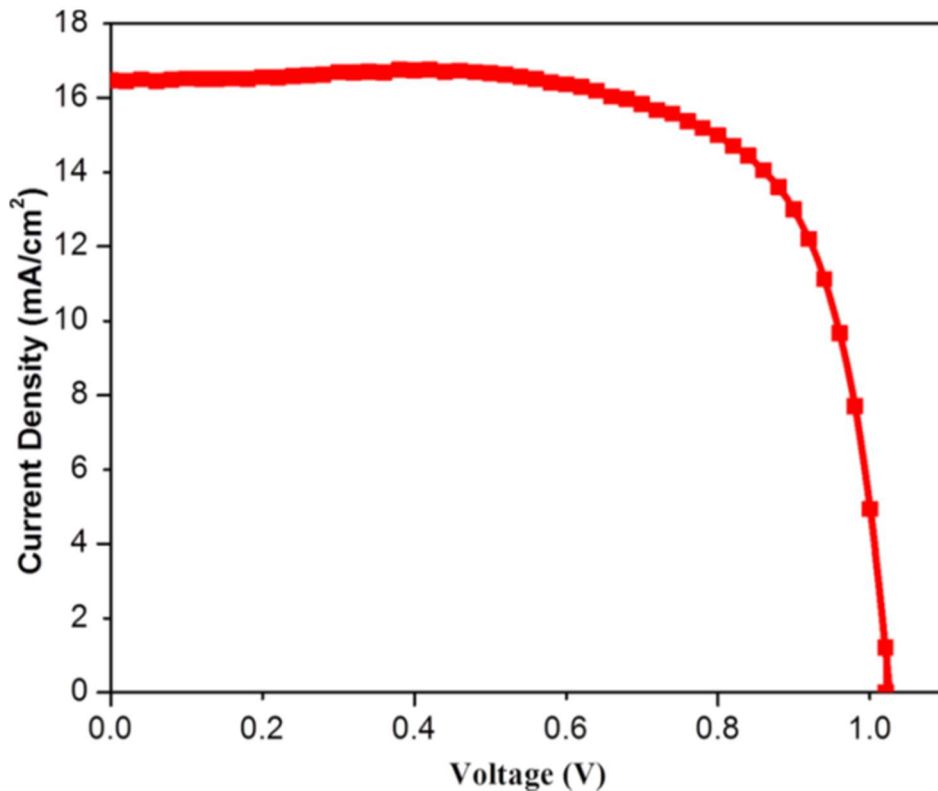
Figure 6.8. J−V curve of IPL-sintered perovskite solar cell under AM 1.5, 1 Sun intensity illumination.

The higher current density values in the IPL-sintered PSCs are likely due to the improved perovskite layer morphology and pore filling. Better coverage of the perovskite layer prevents the leakage of current through the cell and increases the shunt resistance, which in turn increases the current density. A more surprising result is the decrease in series

resistance as seen by the difference in V_{oc}. As mentioned previously, the decrease is likely due to the smoothing of the perovskite film and the creation of a more intimate, less resistive series contact with the gold cathode.

Table 6.1 Summary of Average Performance Parameters of the Solar Cells ± 1 Standard Deviation

heat treatment	J_{sc} (mA/cm^2)	V_{oc} (V)	fill factor	PCE (%)
hot plate	13.05 ± 3.55	0.96 ± 0.031	0.66 ± 0.068	8.21 ± 2.38
IPL	16.55 ± 1.77	1.02 ± 0.032	0.69 ± 0.062	11.5 ± 0.62

All of the solar cells tested in this work produced lower current densities than the highest efficiency perovskite solar cells reported in the literature. This reduced performance is primarily attributed to low-performing spiro-OMeTAD as the hole-transport layer. Four point probe measurements of the spiro-OMeTAD indicated a conductivity of 2.75×10^{-5} S/cm, which is 2 orders of magnitude lower than that of the spiro-OMeTAD used in the highest efficiency perovskite solar cells.[293]

6.7 Conclusion

In summary, photoactive perovskite layers were successfully sintered with a novel IPL treatment with efficiencies exceeding 12%. The processing time was reduced to 2 ms, which is significantly faster than those from previous reports. Additionally, the average performance of the IPL-processed samples showed an improvement compared to the hot-plate-processed samples, although the hot plate samples are not comparable to the state-of-the-art sequential deposited perovskite solar cells.[23] It is important to note that all samples were produced within the same batch maintaining consistent processing with the exception of the thermal treatment. IPL enabled the sintering with 2 ms flashes from a Xe lamp, creating temperatures significantly exceeding the steady-state degradation temperature of 150 °C. The perovskite particles displayed necking and then formed larger crystal grains

after successfully covering the TiO_2 mesoporous layer. XRD, UV−Vis, and PL all verified that the crystal structure was maintained during the morphological change. This advance creates an exciting new method to quickly create dense layers of perovskite, eliminates the rate-limiting annealing step detrimental to industry adoption, and shows the first known occurrence of sintering in $CH_3NH_3PbI_3$ perovskite particles.

CHAPTER 7

2D LAYERED PEROVSKITE TRANSFORMATION INTO A 3D STRUCTURE

7.1 Introduction

The layered 2D perovskites $(BA)_2(MA)Pb_2I_7$ and BA_2PbI_4 (BA meaning n-butylammonium, and MA meaning methylammonium) preferentially grow parallel to their substrate. This is common among 2D perovskite materials deposited on flat substrates, a trend that has also been observed in the case of single-layer halide perovskites.[294] The unit layers are stacked together by a combination of Coulombic and hydrophobic forces to maintain structural integrity and can be thought of as multiple-quantum-well structures in which the semiconducting inorganic layers act as "wells" and the insulating organic layers act as "barriers".[143, 295-297] Therefore, it is regarded that the alkylammonium cations usually try to confine the growth of perovskite within the planer layer, while the small MA ions, on the other hand, try to expand the perovskite growth outside the layer. As the inorganic layer becomes thicker (n increasing), more MA ions are incorporated into the perovskite sheets, thus the impact of MA ions outweighs that of the alkylammonium ions, leading to the variation of preferred growth direction.[143]

7.2 Photonic Heat Transferred Enabled Mechanism of Transition from 2D to 3D Structure

In addition to being more electrically insulating, the long-chain organic layers also have lower thermal decomposition temperatures, 316 ˚C for the temperature at 50% decomposition (D1/2), as compared to the 701 ˚C (D1/2) of the lead iodide octahedras

responsible for the charge conduction in 3D perovskites **(Figure 7.1)**. This large discrepancy of thermal conductivity and decomposition temperature in the constituents of the perovskite structure enables the possibility of using a fast photonic heating technique to target the long-chain inorganic cations. IPL processing powered by Xenon plasma lamps can operate in the millisecond time frame and can provide light with a wide range of wavelengths (from the UV to infra-red region) in a short pulse. Unlike traditional heating processes, heating of the samples is initiated through the absorption of light. This creates localized heating within the material.[298]
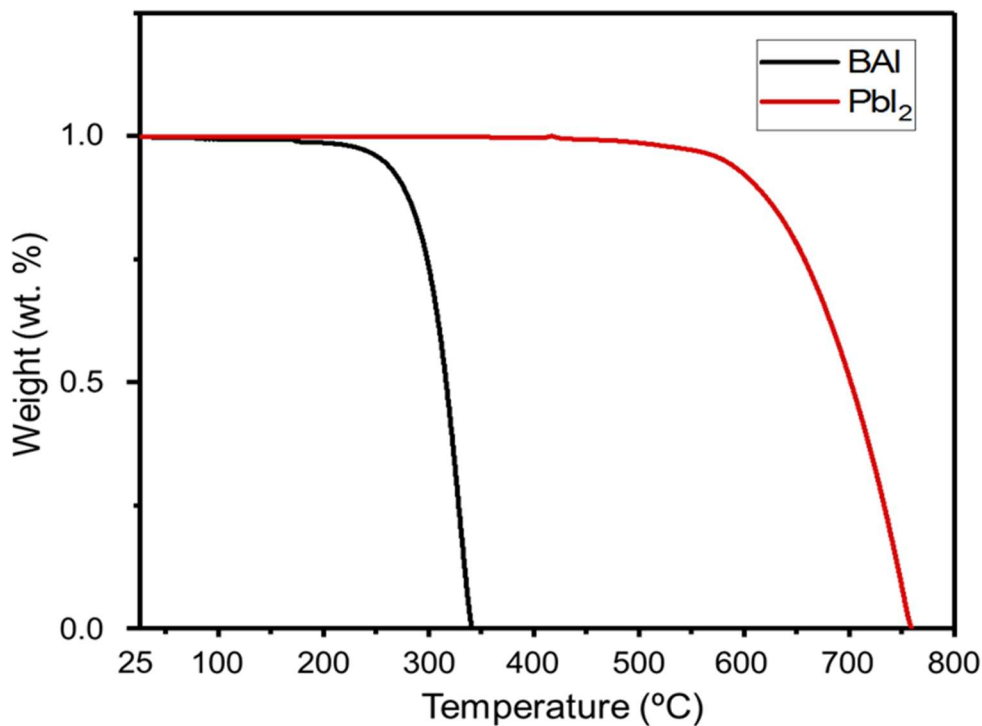
Figure 7.1. Thermal gravimetric analysis of n-butylammonium iodide (BAI) and lead iodide (PbI$_2$)

The suggested mechanism shown in **Figure 7.2** begins by using the IPL technique to transfer an energy exceeding the bandgap of the perovskite to induce a heating within the 2D structure. Next, the phonon induced heating resonates within the poorly conducting

long chain organic cation positions until they begin to decompose. When this occurs, the 3D lead iodide octahedra layers previously separated by the long chain organic cations will begin to collapse and increase the n value in the $CH_3(CH_2)_3NH_3)_2(CH_3NH_3)_{n-1}Pb_nI_{3n+1}$ 2D perovskite. Increases in the n value of the MA and BA containing 2D perovskites reduces the band gap of the material.[299] As more energy is supplied to the 2D material, more of the long chain organic cations will disappear until the structure becomes a 3D perovskite.
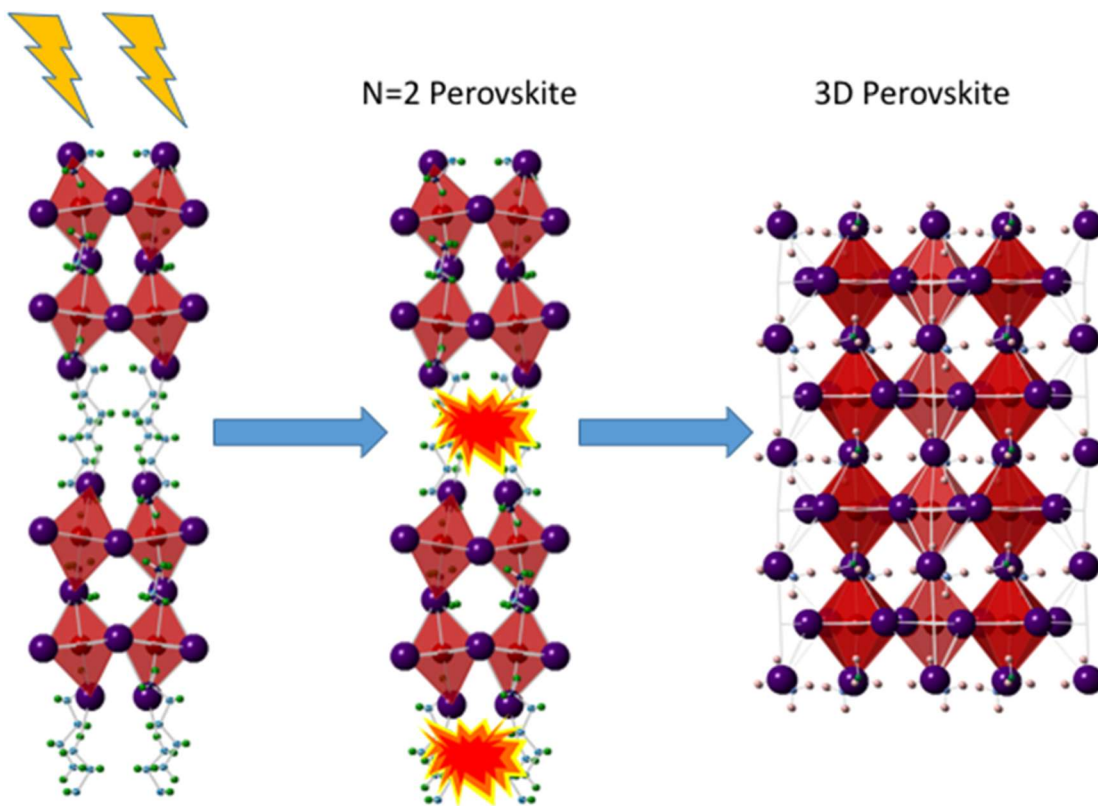
Figure 7.2. Mechanism of 2D to 3D perovskite transformation

7.3 Optical Confirmation of 2D to 3D Perovskite Transformation

To test this mechanism, samples were created using the popular 1-step anti-solvent approach.[300] Stoichiometric amounts of BAI, MAI, and PbI_2 were dissolved in a mixture of dimethylformamide (DMF) and dimethylsulfoxide (DMSO) as detailed in the experimental section to synthesize $CH_3(CH_2)_3NH_3)_2(CH_3NH_3)_2Pb_3I_{10}$. This mixture was

chosen as previous publications have shown that this layered perovskite yields devices with respectable photovoltaic performance.16 The UV-Vis and PL data for the as-deposited samples are shown in **Figures 7.3 and 7.4**. Two distinguishable slopes can be seen in the absorbance graphs: the first at higher wavelengths between 800-850 nm (~1.6 eV) belongs to the 3D perovskite commonly seen in solar cell devices, while the second at lower wavelengths 500-600 nm (~ 2.0 eV) is associated with layered 2D perovskites. This mixture of 2D and 3D perovskite structures is more apparent when viewing PL spectra, in which two peaks are visible rather than the single customary peak in 3D perovskite solar cell devices.
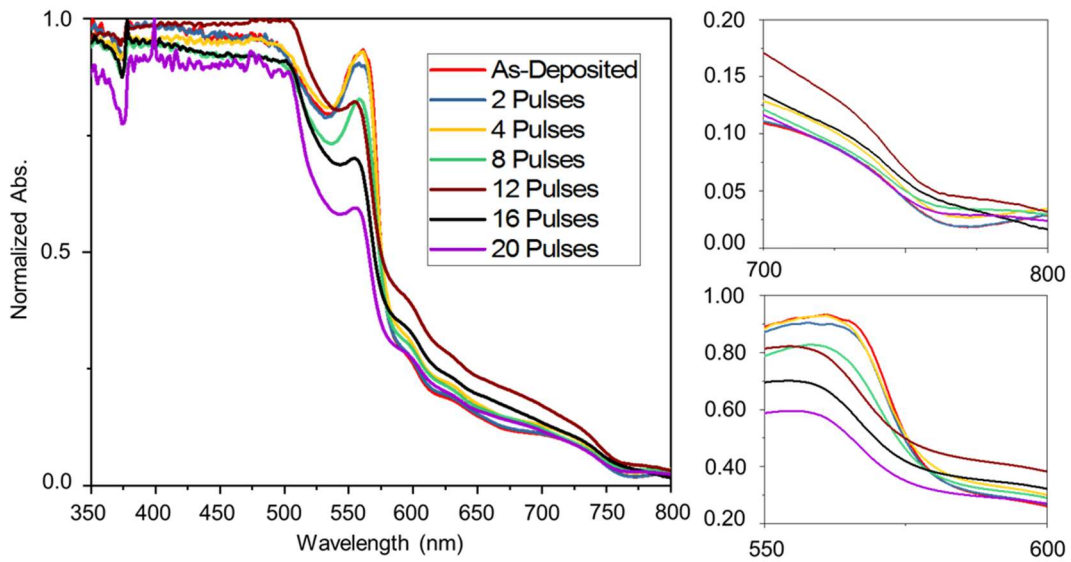
Figure 7.3. UV-Visible Spectra of 2000 J/Pulse IPL treated 2D perovskites
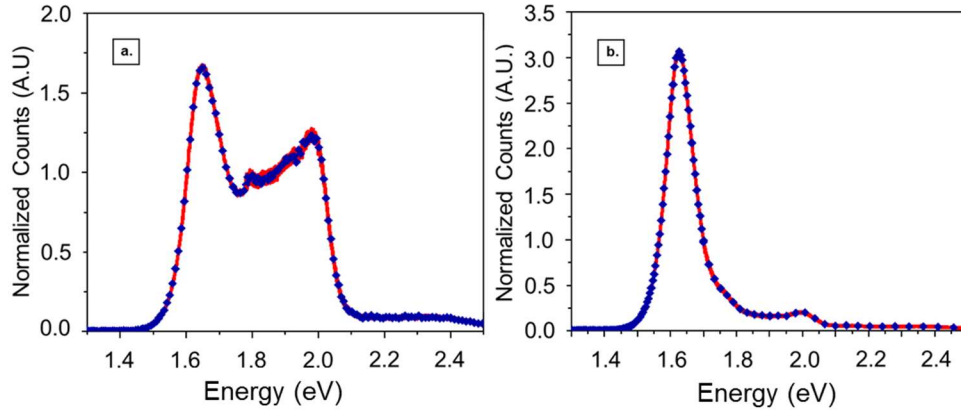
Figure 7.4. Photoluminescence Spectra of (a.) before and (b.) after 12 pulses of 2000 J/Pulse IPL

After exposure to the IPL, the two peaks previously shown are suppressed to one peak **(Figure 7.4)**. As more pulses are applied, the 2D perovskite slope in the absorbance spectra begins to flatten; meanwhile the 3D slope becomes more intense. This is indicative of an increase in the number of 3D perovskites in-between each long chain organic cation spacer. To illustrate this difference more definitively, Urbach energies (E_U) for the 3D and 2D band gaps were calculated **(Figure 7.5)**. Urbach energy can be utilized to access the sub-bandgap defects that originate in the grain boundaries of semiconductors.[301] The general consensus is that the E_U is related to the dynamic phonon disorder and static structural disorder that may arise from lattice point defects, dislocations, strain, deviation from ideal stoichiometry, as well as the effect of the grain surface.[302-303] The relationship between E_U and the absorption coefficient (α) is as follows[304]:

$$\alpha = \alpha_0 \exp\left(\frac{h\nu}{E_U}\right) \tag{1}$$

$$\ln\alpha = \ln\alpha_0 + (h\nu/E_U) \tag{2}$$

where α_0 is a constant, hv is the incident photon energy and E_U is the band tail width (Urbach energy) of the localized states in the optical energy gap.

Before the IPL treatment, the 2D bandgap was the dominant bandgap with an EU that was 8x smaller than the 3D EU. However, after 12 pulses, the 3D bandgap has become the dominant bandgap with an EU that was 1.5x smaller than the 2D EU.
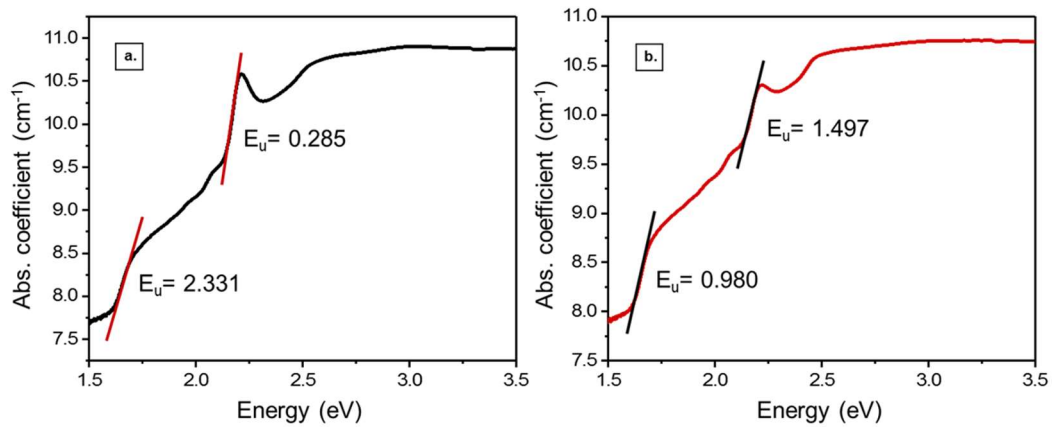
Figure 7.5. Absorption spectra of (a.) before and after (b.) 12 pulses of 2000 J/Pulse IPL with calculated Urbach energies (E_u) for 2D and 3D perovskite bandgaps.

7.4 Crystal Changes During Transformation

X-ray diffraction (XRD) spectra can also be used to confirm the transformation to a 3D perovskite. As the 2D perovskite layers grow thicker and become an increasingly 3D structure, an additional low angle reflection is added for each perovskite layer.[305] Although the precursor perovskite solution was mixed with the stoichiometric ratio of 1:1 M MAI:BAI and the intention of creating the $CH_3(CH_2)_3NH_3)_2(CH_3NH_3)_2Pb_3I_{10}$ (n=3) perovskite; the most intense reflections at 9.02°, and 13.5 °, and 27.16 ° indicate the miller indices for the (040), (060), and (0120) planes of the (n=2) perovskite **(Figure 7.6)**. Other

minor reflections for the as-deposited sample indicate the (110) and (310) indices of the 3D perovskite at 14.07°, and 28.37° respectively. Lack of control for resulting 2D layered perovskites has been documented by others (Liu et al.)[299] and remains an obstacle for the adoption of 1-step processing of 2D layered perovskites.
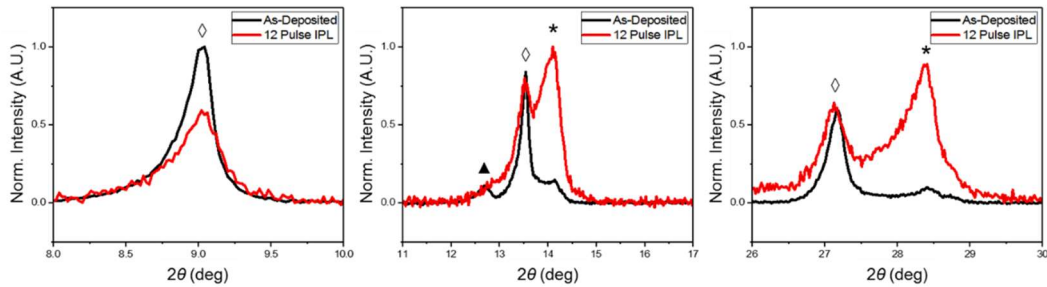
Figure 7.6. XRD spectra of as-deposited and 12 Pulse IPL (3.0 kV = 2000 J/Pulse) treated samples. Symbols: *, ◊, and ▲ represent the 3D perovskite $CH_3NH_3PbI_3$, the 2D n=2 perovskite $(BA)_2(MA)Pb_2I_7$, and lead iodide respectively.

Yang et al. recognized the influence of the solvent used in the crystallization of 2D perovskite crystals to obtain single and few-layer free-standing phenylethylammonium lead halide nanosheets, that is, $(PEA)_2PbX_4$ (PEA = $C_8H_9NH_3$, X = Cl, Br, I), at room temperature.[306] Using this knowledge, the ratio of DMF to DMSO solvent was varied in an attempt to solve the heterogeneous nature of the as-deposited 2D structures and produce more homogeneous as-deposited 2D perovskites of a single n integer. The PL of samples created in a predominantly DMSO solution (4:1 DMSO to DMF) **(Figure 7.7)** were more homogenous in nature; containing less of the 3D perovskite bandgap PL. This would be advantageous in preparing devices, however the morphology was severely impacted by the change in solvent ratio. Top view SEM images **(Figure 7.8)** detail the appearance of pinholes covering the perovskite formed in the predominantly DMSO solution. Pinholes

are incredibly detrimental to device efficiency; therefore the rest of the work was conducted on the perovskites formed under the higher concentration of DMF to DMSO.
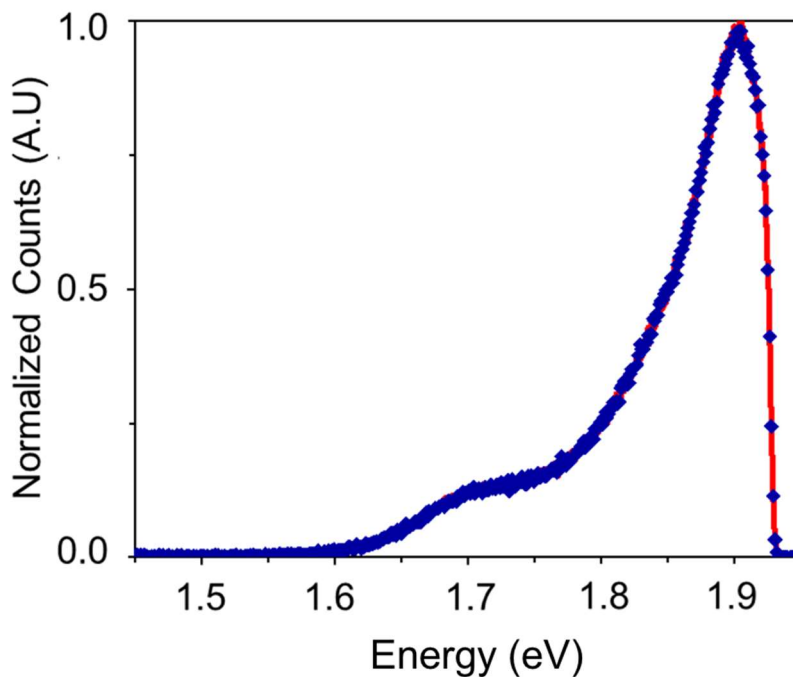
Figure 7.7. 2D perovskite grown using 4:1 ratio of DMSO to DMF

Using the results from the UV-Vis testing, the 12 pulse IPL treated sample was chosen to compare to the as-deposited sample, noting its distinguishable shift in optical absorption. The XRD spectra **(Figure 7.6)** from the IPL treated sample does confirm a change in the crystallography of the perovskite sample. After IPL treatment, the (040 at 8.91˚) (n=2) perovskite reflection substantially decreased in intensity, while the (110 at 14.08˚) and (310 at 28.36˚) 3D perovskite reflections increased considerably. Although the 3D perovskite peaks became the most intense reflections, the remnant minor (n=2) (040 at 8.91˚), (060 at 13.5˚), and (0120 at 27.16˚) reflections will still be detrimental in devices as they will become large recombination centers.
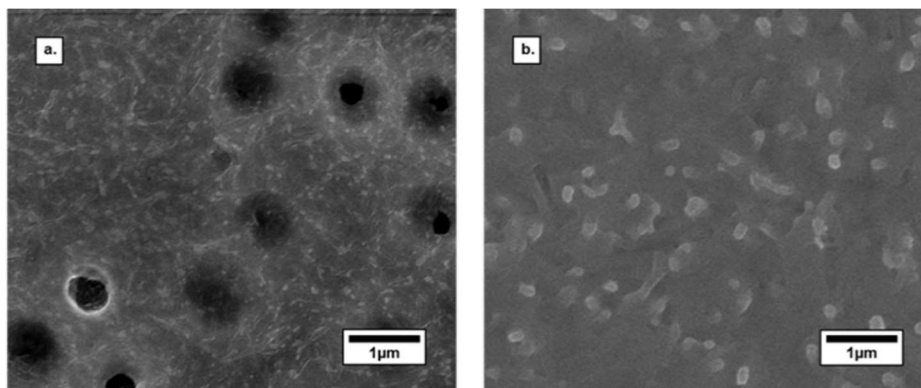
Figure 7.8. Top View SEM images of 2D perovskite deposited with (a.) 4:1 ratio of DMSO to DMF and (b.) 4:1 ratio of DMF to DMSO solvents

7.5 Electrical Performance Enhancement of 2D to 3D Perovskite Transformation

The large recombination centers were evident in the power conversion efficiencies of the devices made with this material. Perovskite devices were assembled on FTO glass slides using TiO_2 as the electron transport material, and spiro-OMeTAD as the hole transport material as shown in the cross-sectional SEM image **(Figure 7.9)**. The devices suffered from poor Fill Factor and efficiency; likely from the aforementioned variety of 2D layered structures in the samples and lack of homogeneity needed to create high efficiency cells.
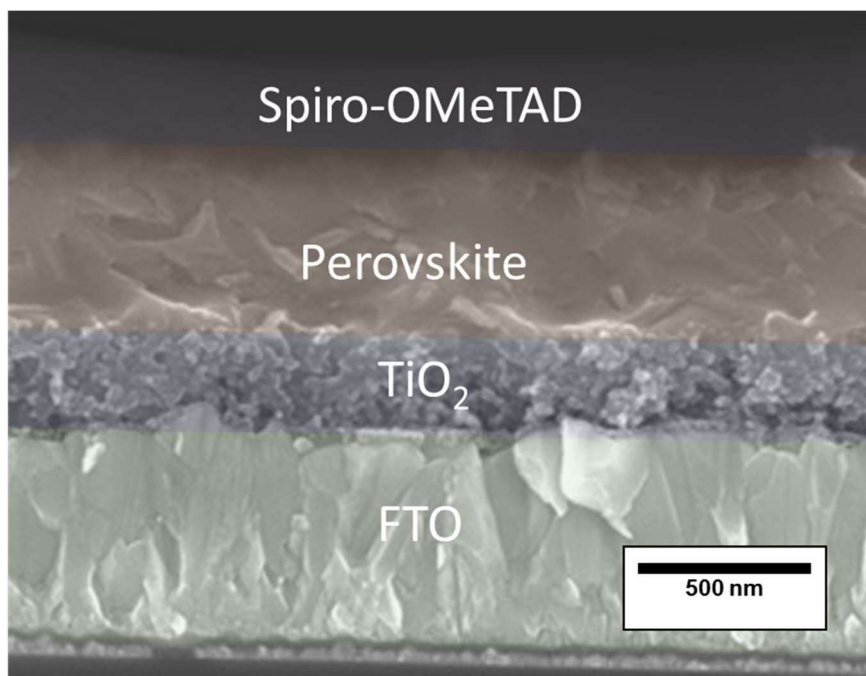
Figure 7.9. Cross-Sectional SEM image of perovskite devices excluding the 80 nm gold contacts

Despite the lower efficiencies, it is worth noting that the IPL treated cells showed an increase in efficiency, Fill Factor FF, short circuit current J_{sc}, and open circuit voltage V_{oc}, compared to the as-deposited solar cells **(Table 7.1)**. The average IPL treated cells were 4.8x more efficient than the as-deposited 2D cells. This is expected, as the highest occupied molecular orbital (HOMO) of the n=2 perovskite is 4.88 eV vs. vacuum; higher than the HOMO level of the hole transport material spiro-OMeTAD by 0.34 eV **(Figure 7.10)**.[143, 307] At this position, hole transport is unlikely due to recombination, as holes more efficiently travel up the band diagram rather than down in energies. Meanwhile, the 3D perovskites have a lower shifted HOMO level that is better suited for spiro-OMeTAD. The 3D perovskites lowest unoccupied molecular orbital (LUMO) is also better matched with the electron transport material TiO_2 (0.32 eV difference) in comparison to the n=2 perovskites (1.37 eV difference) as electrons flow downhill to lesser potential energies.

Given the band edges of both perovskite materials, it is reasonable for the IPL treated samples to have improved performance despite the noticeable n=2 perovskite impurities.

Table 7.1 Efficiency, Fill Factor FF, short circuit current J_{sc}, and open circuit voltage V_{oc} of IPL treated 2D PSCs compared to as-deposited 2D PSCs

	J_{sc} (mA/cm^2)	V_{oc} (V)	Fill Factor	Efficiency (%)
As-Deposited	0.661	0.357	0.298	0.071
IPL Treated	0.742	0.850	0.487	0.342
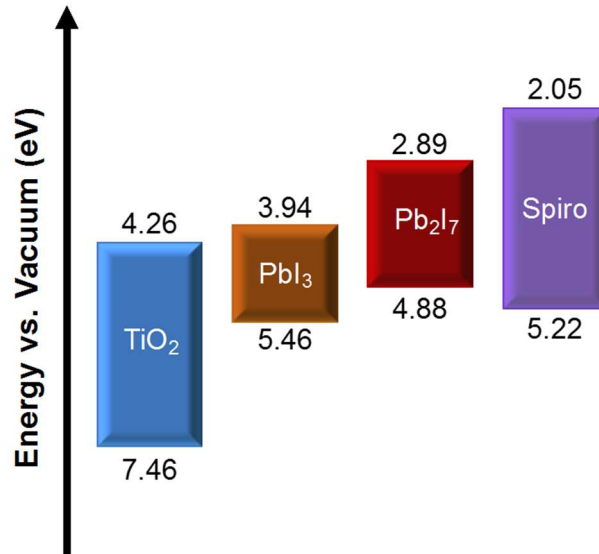
Figure 7.10. Energy band diagram of perovskite devices with PbI$_7$ representing the as-deposited 2D material and PbI$_3$ representing the IPL processed 3D perovskite

Impedance spectroscopy (IS) measurements were performed to help understand the internal electrical processes and suggest the shortcomings of the converted 3D perovskites. Impedance spectroscopy applies a small-amplitude modulated voltage stimulus and detects the responding modulated (alternating) current.[255] Although there is still plenty of interpretation of the physical significance of this data; the highest efficiency perovskite solar cells to date have a signature of two RC element semicircles while under AM 1.5G

at 100 mW/cm^2 light intensity. The semicircle in the higher frequency spectrum is attributed predominantly to the impedance arising from the electronic transport while the semicircle in the low frequency spectrum is attributed to the impedance arising either from charge or mass transfer at the interface or Warburg ion diffusion.[256]

Impedance spectroscopy results are conventionally presented as a Nyquist plot **(Figure 7.11)**, with the real component of the impedance (Z′) as the abscissa and the imaginary part (Z″) as the ordinate.[308] Comparing the as-deposited and IPL treated samples at lower forward bias, the IPL treated samples indicated a transport resistance visible as a 45˚ straight line characteristic of a transmission line. The transmission line merging with the semicircle at lower frequencies has been known to represent recombination resistance and or Warburg diffusion impedance for the diffusion of ions.[309] It is likely ion/Warburg diffusion is taking place as the presence of a linear region instead of just a semicircle indicates a double-layer capacitance.[310]
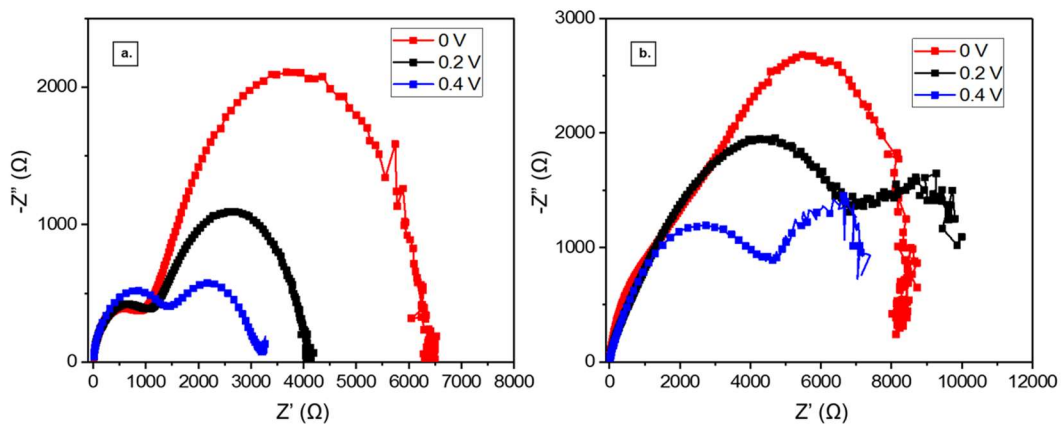
Figure 7.11. Impedance Spectroscopy Data of (a.) as-deposited and (b.) 12 pulse at 2000 J/Pulse IPL treated perovskite devices

The appearance of a change in the IS spectra is indicative of a change in the alkylammonium cation in the perovskite structure. The ionic diffusion coefficient for alkylammonium cations in perovskites increases with decreasing size of the ions. Because the change in the spectra is occurring in the slower time regime, it is unlikely this can be attributed with iodide transport since the iodide mobility is <1 μs and would be observed in the first semicircle, as noted by others.[310-311] This signifies that the change in the IS spectra is due to the elimination of the larger n-butylammonium cation, which is now dominated by shorter chain groups like the methylammonium cation.

7.6 Conclusion

The fast photonic processing of the IPL enabled the first conversion of a stable 2D perovskite structure into a 3D structure. This caused an E_g shift from 2.0 eV to 1.6eV and shows the capabilities of E_g tuning enabled by the IPL. While this work is the first documentation of E_g tuning enabled by a photonic effect, it presents a possible inexpensive manufacturing technique that could use one material to create several different colors for the future development of pixel-based LED displays.

CHAPTER 8

CONCLUSION

CdTe thin films grown by low temperature electrodeposition were treated for the first time with IPL. The low temperature electrodeposition growth resulted in films consisting of nanoparticles, with reduced melting point temperatures. In combination with the high temperature rise produced by the pulses of light, the lower melting temperature resulted in pores/voids being filled as well as enhanced grain growth. As a result, pin-holes and grain boundary recombination were diminished. Subsequently the fill factors of PV devices created using this technology are likely to be significantly increased.

The popular $CdCl_2$ treatment for CdTe devices successfully improved crystallinity in the CdTe films with after IPL treatment. At lower energy densities of the IPL treatment, crystallinity improved, keeping the (111) preferred orientation. Meanwhile, as the energy increased, the layer became randomly oriented, but crystal grains grew continuously. These grains were randomly oriented showing all three CdTe peaks with comparable intensities.

Low temperature PL helped reveal the mystery behind the mechanism of the $CdCl_2$ treatment and helped draw the following important conclusions:

(1) All four CdTe layers electroplated using sulfate, nitrate and chloride of cadmium, precursors exhibited four electron traps (T1, T2, T3 and T4) situated at similar energy positions.

(2) After CdCl$_2$ treatment, T1, T2 and T3 are completely annealed-out or showed considerable reduction in concentration. This reduction was a positive effect for device performance.

(3) CdCl$_2$ treatment drastically reduced the mid-gap killer centers situated at the T2 level. Wide defects distribution (*0.30 eV) reduced to a narrow defect band (*0.09 eV) and the intensity also reduced by considerable amounts. This will have a drastic and positive effect on improvement of solar cell performance by reducing recombination of photogenerated charge carriers.

(4) The two defect levels T1 and T2, situated in the mid-gap are closely related to Te-richness in CdTe layers. The CdCl$_2$ treatment converts the Te-richness towards Cd-richness, reducing precipitated Te, and drastically removing mid-gap defects.

(5) Out of the four CdTe layers studied in this work, the material grown using the CdCl$_2$ precursor seems to produce a better material with a cleaner bandgap. This material is comparable to bulk CdTe wafers in terms of defect levels.

Photoactive perovskite CH$_3$NH$_3$PbI$_3$ layers were successfully sintered with a novel IPL treatment with efficiencies exceeding 12%. The processing time was reduced to 2 ms, which was significantly faster than those from previous reports. Additionally, the average performance of the IPL-processed samples showed an improvement compared to the hot-plate-processed samples. The perovskite particles displayed necking and then formed larger crystal grains after successfully covering the TiO$_2$ mesoporous layer. XRD, UV−Vis, and PL all verified that the crystal structure was maintained during the morphological change. This advance creates an exciting new method to quickly create dense layers of

perovskite, eliminating the rate-limiting annealing step detrimental to industry adoption, and shows the first known occurrence of sintering in $CH_3NH_3PbI_3$ perovskite particles.

Lastly, the fast photonic processing of the IPL enabled the first conversion of a stable 2D perovskite structure into a 3D structure. This caused an E_g shift from 2.0 eV to 1.6eV and showed the capabilities of E_g tuning enabled by the IPL. While this work is the first documentation of E_g tuning enabled by a photonic effect, it presents a possible inexpensive manufacturing technique that could use one material to create several different colors for the future development of pixel-based LED displays.

CHAPTER 9

RECOMMENDATIONS

CdTe:

The IPL process has been used to create CdTe on FTO. However, because of the lattice mismatch between these two materials, it could only be grown in the nanometer range and was not conducive to creating high efficiency devices. Future studies could deposit thicker and higher efficiency CdTe devices by first depositing CdS to eliminate the lattice mismatch between CdTe and FTO. Another interesting problem that could be solved by this study is the diffusion of substrate particles into the CdS and CdTe layers. This is detrimental to device performance and is inherent in the high temperature CSS depositions used by the industry. Unlike CSS, the IPL is a surface treatment and should be able to avoid these diffusion problems inherent in CSS techniques.

High heat treatments like CSS are used to create CdTe solar cells in the industry and inherently produce p-type CdTe. While electrodeposition can grow CdTe n-type or p-type by adjusting growth voltage, this process is cumbersome and varies depending on the operator of the electrochemical bath. An opportunity exists to apply a high heat treatment to the surface of the n-type electrodeposited CdTe thin films using the IPL to change the surface electrical properties of the CdTe from n-type to p-type to create the graded band gap architecture shown in chapter 2.

The last recommendation for CdTe solar device research is using the IPL as a surface doping technique. High efficiency electrodeposited CdTe devices use an

alloy of copper and gold when making contacts. The copper is used to effectively pin the fermi level of the CdTe to enhance device performance. Copper needs to be the minority metal in this alloy, otherwise the CdTe can become overdoped and lose efficiency. The IPL could be used to study the effects of the diffusion of copper on the electrical properties of CdTe devices. With its high range of settings, the copper diffusion process could be optimized and better understood to create higher efficiency devices.

Perovskites:

To date, little research has been accomplished on doping organometal perovskites. It is understandable as the material is highly temperature sensitive, eliminating most heat induced doping treatments, and fragile to physical treatments like sputtering. This is why researchers seldom use sputtering as a method to deposit contacts on PSCs. Because of this lack of research in doping organometal perovskites, devices have all contained heterojunctions. Heterojunctions have an unavoidable loss in efficiency from lattice mismatch, so it would be preferable to create a homojunction PSC. The IPL has shown the ability to rearrange the atoms within perovskite thin films and future efforts could use the IPL to dope the material, sparking next generation homojunction PSCs.

Additionally, research attempts have been made to utilize metal-containing compounds as potential hole transport materials. These attempts used sole-gel reactions, and or higher temperature sintering to create a uniform layer of the metal-containing compound. As a result, the metal-containing transport materials must be deposited on the transparent electrode prior to the perovskite deposition. Although these materials match the HOMO layer of the PSC with an energy difference of (0.06-0.2 eV), they do not match the FTO work function as nicely with an energy difference of (0.7-0.9 eV). This represents

a bottleneck in hole-transport between the metal-containing compound and the FTO substrate and will limit efficiencies. A PSC utilizing IPL sintered cuprous oxide as a hole transport material could be used to create lower cost alternatives to the conventionally used Spiro-OMeTAD. The use of Cu_2O would be a breakthrough in perovskite design as it would replace Spiro-OMeTAD with a material that is close to 1/100 of the cost. Currently this has not been implemented using scalable wet chemistry in the conventional PSC architecture due to the porous structure resulting from depositing nanoparticles on the perovskite material. The particles cannot be sintered using conventional techniques because of the PSC's low degradation temperature. A porous hole transport layer is highly undesirable as it enables the possibility of shorting the metal electrode to the perovskite contact and disables the efficiency benefits of a hole-transport layer. The IPL could be used to overcome this limitation by sintering the top layer of cuprous oxide nanoparticles with short bursts of energy while limiting the heat transfer that would otherwise degrade the perovskite.

REFERENCES

1.   Scenario, N.; East, M.; Cedex, P., World energy outlook 2014 factsheet. *Paris: International Energy Agency* **2015**.

2.   Petroleum, B., BP Statistical Review of World Energy June 2015"bp. com/statisticalreview. *Accessed: September* **2015**.

3.   Fröhlich, C.; Lean, J., Solar radiative output and its variability: evidence and mechanisms. *Astronomy and Astrophysics Review* **2004**, *12* (4), 273-320.

4.   Jacobsen, M. Z.; Delucchi, M. A., Providing All Global Energy with Wind, Water, and Solar Power, Part 1: Technologies, Energy Resources, Quantities and Areas of Infrastructure, and Materials. *ENERGY POL'Y* **2011**, *39*, 1154.

5.   Pidwirny, M. *Surface area of our planet covered by oceans and continents, University of British Columbia, Okanagan*; Retrieved 2007-11-26: 2006.

6.   Jean, J.; Brown, P. R.; Jaffe, R. L.; Buonassisi, T.; Bulović, V., Pathways for solar photovoltaics. *Energy & Environmental Science* **2015**, *8* (4), 1200-1219.

7.   Association, E. E. P. I., Global market outlook for photovoltaics 2014-2018. *Brussels, Belgium* **2014**, *60*.

8.   Louwen, A.; Van Sark, W.; Schropp, R.; Faaij, A., A cost roadmap for silicon heterojunction solar cells. *Solar Energy Materials and Solar Cells* **2016**, *147*, 295-314.

9.   Hsu, D. D.; O'Donoughue, P.; Fthenakis, V.; Heath, G. A.; Kim, H. C.; Sawyer, P.; Choi, J. K.; Turney, D. E., Life cycle greenhouse gas emissions of crystalline silicon photovoltaic electricity generation. *Journal of Industrial Ecology* **2012**, *16* (s1), S122-S135.

10.   Kim, H. C.; Fthenakis, V.; Choi, J. K.; Turney, D. E., Life cycle greenhouse gas emissions of thin-film photovoltaic electricity generation. *Journal of Industrial Ecology* **2012**, *16* (s1), S110-S121.

11.   Fraunhofer, I., Photovoltaics report. *Disponible sur:* http://www/. *ise. fraunhofer. de/en/downloads-englisch/pdf-files-englisch/photovoltaics-report-slides. pdf/view, rapport publié en* **2014**.

12.   Ojo, A.; Olusola, I.; Dharmadasa, I., Effect of the inclusion of galium in normal cadmium chloride treatment on electrical properties of CdS/CdTe solar cell. *Materials Chemistry and Physics* **2017**.

13.   Dharmadasa, I. M.; Ojo, A. A.; Salim, H. I.; Dharmadasa, R., Next generation solar cells based on graded bandgap device structures utilising rod-type nano-materials. *Energies* **2015**, *8* (6), 5440-5458.

14.   Wu, X., High-efficiency polycrystalline CdTe thin-film solar cells. *Solar energy* **2004**, *77* (6), 803-814.

15.   National Renewable Energy Laboratory, Best Research-Cell Efficiencies chart. http://www.nrel.gov/ncpv/images/efficiency_chart.jpg. (accessed May 9, 2017).

16.   Loi, M. A.; Hummelen, J. C., Hybrid Solar Cells - Perovskites Under the Sun. *Nat. Mater.* **2013**, *12* (12), 1087-1089.

17.   Eperon, G. E.; Stranks, S. D.; Menelaou, C.; Johnston, M. B.; Herz, L. M.; Snaith, H. J., Formamidinium Lead Trihalide: a Broadly Tunable Perovskite for Efficient Planar Heterojunction Solar Cells. *Energy Environ. Sci.* **2014,** *7* (3), 982-988.

18.   Noel, N. K.; Stranks, S. D.; Abate, A.; Wehrenfennig, C.; Guarnera, S.; Haghighirad, A.-A.; Sadhanala, A.; Eperon, G. E.; Pathak, S. K.; Johnston, M. B.; Petrozza, A.; Herz, L. M.; Snaith, H. J., Lead-free organic-inorganic tin halide perovskites for photovoltaic applications. *Energy & Environmental Science* **2014,** *7* (9), 3061-3068.

19.   Hao, F.; Stoumpos, C. C.; Cao, D. H.; Chang, R. P.; Kanatzidis, M. G., Lead-free solid-state organic-inorganic halide perovskite solar cells. *Nature Photonics* **2014,** *8* (6), 489-494.

20.   Noh, J. H.; Im, S. H.; Heo, J. H.; Mandal, T. N.; Seok, S. I., Chemical management for colorful, efficient, and stable inorganic–organic hybrid nanostructured solar cells. *Nano letters* **2013,** *13* (4), 1764-1769.

21.   Xiao, S.; Xu, S., High-Efficiency Silicon Solar Cells—Materials and Devices Physics. *Critical Reviews in Solid State and Materials Sciences* **2014,** *39* (4), 277-317.

22.   You, J.; Yang, Y.; Hong, Z.; Song, T.-B.; Meng, L.; Liu, Y.; Jiang, C.; Zhou, H.; Chang, W.-H.; Li, G., Moisture assisted perovskite film growth for high performance solar cells. *Applied Physics Letters* **2014,** *105* (18), 183902.

23.   Burschka, J.; Pellet, N.; Moon, S.-J.; Humphry-Baker, R.; Gao, P.; Nazeeruddin, M. K.; Graetzel, M., Sequential Deposition as a Route to High-Performance Perovskite-sensitized Solar Cells. *Nature (London, U. K.)* **2013,** *499* (7458), 316-319.

24.   Yantara, N.; Sabba, D.; Yanan, F.; Kadro, J. M.; Moehl, T.; Boix, P. P.; Mhaisalkar, S.; Gratzel, M.; Gratzel, C., Loading of Mesoporous Titania Films by CH3NH3PbI3 Perovskite, Single Step vs. Sequential Deposition. *Chem. Commun. (Cambridge, U. K.)* **2015,** *51* (22), 4603-4606.

25.   Lavery, B. W.; Kumari, S.; Konermann, H.; Draper, G.; Spurgeon, J. M.; Druffel, T. L., Intense Pulsed Light Sintering of CH3NH3PbI3 Solar Cells. *ACS applied materials & interfaces* **2016**.

26.   Eperon, G. E.; Burlakov, V. M.; Docampo, P.; Goriely, A.; Snaith, H. J., Morphological Control for High Performance, Solution-Processed Planar Heterojunction Perovskite Solar Cells. *Advanced Functional Materials* **2014,** *24* (1), 151-157.

27.   Zhou, Y.; Yang, M.; Wu, W.; Vasiliev, A. L.; Zhu, K.; Padture, N. P., Room-temperature Crystallization of Hybrid-Perovskite Thin Films via Solvent-solvent Extraction for High-performance Solar Cells. *Journal of Materials Chemistry A* **2015,** *3* (15), 8178-8184.

28.   Ahn, N.; Son, D.-Y.; Jang, I.-H.; Kang, S. M.; Choi, M.; Park, N.-G., Highly Reproducible Perovskite Solar Cells with Average Efficiency of 18.3% and Best Efficiency of 19.7% Fabricated via Lewis Base Adduct of Lead(II) Iodide. *J. Am. Chem. Soc.* **2015,** *137* (27), 8696-8699.

29.   Abbel, R.; van Lammeren, T.; Hendriks, R.; Ploegmakers, J.; Rubingh, E. J.; Meinders, E. R.; Groen, W. A., Photonic Flash Sintering of Silver Nanoparticle Inks: a Fast and Convenient Method for the Preparation of Highly Conductive Structures on Foil. *MRS Commun.* **2012,** *2* (4), 145-150.

30.   Park, S.-H.; Chung, W.-H.; Kim, H.-S., Temperature changes of copper nanoparticle ink during flash light sintering. *J. Mater. Process. Technol* **2014,** *214* (11), 2730-2738.

31.   Wünscher, S.; Abbel, R.; Perelaer, J.; Schubert, U. S., Progress of alternative sintering approaches of inkjet-printed metal inks and their application for manufacturing of flexible electronic devices. *Journal of Materials Chemistry C* **2014,** *2* (48), 10232-10261.

32.   Shen, M.; Jia, W.; You, Y.; Hu, Y.; Li, F.; Tian, S.; Li, J.; Jin, Y.; Han, D., Luminescent properties of CdTe quantum dots synthesized using 3-mercaptopropionic acid reduction of tellurium dioxide directly. *Nanoscale research letters* **2013,** *8* (1), 253.

33.   Zhu, Y.; Wang, L.; Huang, G.; Chai, Y.; Zhai, X.; Huang, W., Luminescent and photocatalytic properties of hollow SnO 2 nanospheres. *Materials Science and Engineering: B* **2013,** *178* (10), 725-729.

34.   Buffat, P.; Borel, J. P., Size effect on the melting temperature of gold particles. *Physical review A* **1976,** *13* (6), 2287.

35.   Sattler, K. D., *Handbook of nanophysics: nanoparticles and quantum dots*. CRC press: 2010.

36.   Khairutdinov, R. F., Chemistry of semiconductor nanoparticles. *Russian chemical reviews* **1998,** *67* (2), 109-122.

37.   Perelaer, J.; Schubert, U. S., Novel approaches for low temperature sintering of inkjet-printed inorganic nanoparticles for roll-to-roll (R2R) applications. *Journal of Materials Research* **2013,** *28* (04), 564-573.

38.   Bordia, R. K.; Kang, S. J. L.; Olevsky, E. A., Current understanding and future research directions at the onset of the next century of sintering science and technology. *Journal of the American Ceramic Society* **2017**.

39.   German, R. M., Sintering theory and practice. *Solar-Terrestrial Physics (Solnechno-zemnaya fizika)* **1996**, 568.

40.   Becquerel, A.-E., Mémoire sur les effets électriques produits sous l'influence des rayons solaires. *Comptes rendus* **1839,** *9* (567), 1839.

41.   Adams, W. G.; Day, R., The action of light on selenium. *Philosophical Transactions of the Royal Society of London* **1877,** *167*, 313-349.

42.   Rogers, K.; Painter, J.; Healy, M.; Lane, D.; Ozsan, M., The crystal structure of CdS–CdTe thin film heterojunction solar cells. *Thin Solid Films* **1999,** *339* (1), 299-304.

43.   Loginov, Y.; Durose, K.; Al-Allak, H.; Galloway, S.; Oktik, S.; Brinkman, A.; Richter, H.; Bonnet, D., Transmission electron microscopy of CdTeCdS based solar cells. *Journal of crystal growth* **1996,** *161* (1-4), 159-163.

44.   Romeo, A.; Terheggen, M.; Abou-Ras, D.; Bätzner, D.; Haug, F. J.; Kälin, M.; Rudmann, D.; Tiwari, A., Development of thin-film Cu (In, Ga) Se2 and CdTe solar cells. *Progress in Photovoltaics: Research and Applications* **2004,** *12* (2-3), 93-111.

45.   Morales-Acevedo, A., Physical basis for the design of CdS/CdTe thin film solar cells. *Solar energy materials and solar cells* **2006,** *90* (6), 678-685.

46.   Chu, T. L.; Chu, S. S., Thin film II–VI photovoltaics. *Solid-State Electronics* **1995,** *38* (3), 533-549.

47.   Romeo, N.; Bosio, A.; Romeo, A., An innovative process suitable to produce high-efficiency CdTe/CdS thin-film modules. *Solar Energy Materials and Solar Cells* **2010,** *94* (1), 2-7.

48.   Loferski, J. J., Theoretical considerations governing the choice of the optimum semiconductor for photovoltaic solar energy conversion. *Journal of Applied Physics* **1956,** *27* (7), 777-784.

49.   Kumar, S. G.; Rao, K. K., Physics and chemistry of CdTe/CdS thin film heterojunction photovoltaic devices: fundamental and critical aspects. *Energy & Environmental Science* **2014,** *7* (1), 45-102.

50.   Aberle, A. G., Thin-film solar cells. *Thin solid films* **2009,** *517* (17), 4706-4710.

51.   Gupta, A.; Parikh, V.; Compaan, A. D., High efficiency ultra-thin sputtered CdTe solar cells. *Solar Energy Materials and Solar Cells* **2006,** *90* (15), 2263-2271.

52.   Bosio, A.; Rosa, G.; Menossi, D.; Romeo, N., How the Chlorine Treatment and the Stoichiometry Influences the Grain Boundary Passivation in Polycrystalline CdTe Thin Films. *Energies* **2016,** *9* (4), 254.

53.   Molva, F.; Chamonal, J.; Pautrat, J., Shallow acceptors in cadmium telluride. *physica status solidi (b)* **1982,** *109* (2), 635-644.

54.   Zhao, Y.; Zhu, K., Organic–inorganic hybrid lead halide perovskites for optoelectronic and electronic applications. *Chemical Society Reviews* **2016,** *45* (3), 655-689.

55.   Poglitsch, A.; Weber, D., Dynamic disorder in methylammoniumtrihalogenoplumbates (II) observed by millimeter-wave spectroscopy. *The Journal of chemical physics* **1987,** *87* (11), 6373-6378.

56.   Mitzi, D.; Feild, C.; Harrison, W.; Guloy, A., Conducting tin halides with a layered organic-based perovskite structure. *Nature* **1994,** *369* (6480), 467-469.

57.   Liang, K.; Mitzi, D. B.; Prikas, M. T., Synthesis and characterization of organic−inorganic perovskite thin films prepared using a versatile two-step dipping technique. *Chemistry of materials* **1998,** *10* (1), 403-411.

58.   Kojima, A.; Teshima, K.; Shirai, Y.; Miyasaka, T., Organometal halide perovskites as visible-light sensitizers for photovoltaic cells. *Journal of the American Chemical Society* **2009,** *131* (17), 6050-6051.

59.   Lee, M. M.; Teuscher, J.; Miyasaka, T.; Murakami, T. N.; Snaith, H. J., Efficient hybrid solar cells based on meso-superstructured organometal halide perovskites. *Science* **2012,** *338* (6107), 643-647.

60.   Li, Y.; Zhao, Y.; Chen, Q.; Yang, Y.; Liu, Y.; Hong, Z.; Liu, Z.; Hsieh, Y.-T.; Meng, L.; Li, Y., Multifunctional fullerene derivative for interface engineering in perovskite solar cells. *Journal of the American Chemical Society* **2015,** *137* (49), 15540-15547.

61.   Saliba, M.; Matsui, T.; Domanski, K.; Seo, J.-Y.; Ummadisingu, A.; Zakeeruddin, S. M.; Correa-Baena, J.-P.; Tress, W. R.; Abate, A.; Hagfeldt, A., Incorporation of rubidium cations into perovskite solar cells improves photovoltaic performance. *Science* **2016,** *354* (6309), 206-209.

62.   Anaraki, E. H.; Kermanpur, A.; Steier, L.; Domanski, K.; Matsui, T.; Tress, W.; Saliba, M.; Abate, A.; Grätzel, M.; Hagfeldt, A., Highly efficient and stable planar perovskite solar cells by solution-processed tin oxide. *Energy & Environmental Science* **2016,** *9* (10), 3128-3134.

63.   Liu, D.; Kelly, T. L., Perovskite solar cells with a planar heterojunction structure prepared using room-temperature solution processing techniques. *Nature photonics* **2014,** *8* (2), 133-138.

150

64.   Mahmood, K.; Swain, B. S.; Amassian, A., 16.1% Efficient Hysteresis-Free Mesostructured Perovskite Solar Cells Based on Synergistically Improved ZnO Nanorod Arrays. *Adv. Energy Mater.* **2015,** *5* (17), n/a.

65.   Heo, J. H.; Han, H. J.; Kim, D.; Ahn, T. K.; Im, S. H., Hysteresis-less inverted CH 3 NH 3 PbI 3 planar perovskite hybrid solar cells with 18.1% power conversion efficiency. *Energy & Environmental Science* **2015,** *8* (5), 1602-1608.

66.   Domanski, K.; Correa-Baena, J.-P.; Mine, N.; Nazeeruddin, M. K.; Abate, A.; Saliba, M.; Tress, W.; Hagfeldt, A.; Grätzel, M., Not all that glitters is gold: Metal-migration-induced degradation in perovskite solar cells. *ACS nano* **2016,** *10* (6), 6306-6314.

67.   Dong, Q.; Liu, F.; Wong, M. K.; Tam, H. W.; Djurišić, A. B.; Ng, A.; Surya, C.; Chan, W. K.; Ng, A. M. C., Encapsulation of Perovskite Solar Cells for High Humidity Conditions. *ChemSusChem* **2016,** *9* (18), 2597-2603.

68.   Zhu, Z.; Bai, Y.; Liu, X.; Chueh, C. C.; Yang, S.; Jen, A. K. Y., Enhanced Efficiency and Stability of Inverted Perovskite Solar Cells Using Highly Crystalline SnO2 Nanocrystals as the Robust Electron-Transporting Layer. *Advanced Materials* **2016,** *28* (30), 6478-6484.

69.   Leijtens, T.; Eperon, G. E.; Pathak, S.; Abate, A.; Lee, M. M.; Snaith, H. J., Overcoming ultraviolet light instability of sensitized TiO2 with meso-superstructured organometal tri-halide perovskite solar cells. *Nat. Commun.* **2013,** *4*, 3885/1-3885/8.

70.   Wojciechowski, K.; Stranks, S. D.; Abate, A.; Sadoughi, G.; Sadhanala, A.; Kopidakis, N.; Rumbles, G.; Li, C.-Z.; Friend, R. H.; Jen, A. K.-Y., Heterojunction modification for highly efficient organic–inorganic perovskite solar cells. *Acs Nano* **2014,** *8* (12), 12701-12709.

71.   Wojciechowski, K.; Leijtens, T.; Siprova, S.; Schlueter, C.; Hörantner, M. T.; Wang, J. T.-W.; Li, C.-Z.; Jen, A. K.-Y.; Lee, T.-L.; Snaith, H. J., C60 as an efficient n-type compact layer in perovskite solar cells. *The journal of physical chemistry letters* **2015,** *6* (12), 2399-2405.

72.   Zhang, Y.; Liu, M.; Eperon, G. E.; Leijtens, T. C.; McMeekin, D.; Saliba, M.; Zhang, W.; de Bastiani, M.; Petrozza, A.; Herz, L. M., Charge selective contacts, mobile ions and anomalous hysteresis in organic–inorganic perovskite solar cells. *Materials Horizons* **2015,** *2* (3), 315-322.

73.   Correa Baena, J. P.; Steier, L.; Tress, W.; Saliba, M.; Neutzner, S.; Matsui, T.; Giordano, F.; Jacobsson, T. J.; Srimath Kandada, A. R.; Zakeeruddin, S. M.; Petrozza, A.; Abate, A.; Nazeeruddin, M. K.; Gratzel, M.; Hagfeldt, A., Highly efficient planar perovskite solar cells through band alignment engineering. *Energy & Environmental Science* **2015,** *8* (10), 2928-2934.

74.   Li, Y.; Zhu, J.; Huang, Y.; Liu, F.; Lv, M.; Chen, S.; Hu, L.; Tang, J.; Yao, J.; Dai, S., Mesoporous SnO2 nanoparticle films as electron-transporting material in perovskite solar cells. *RSC Adv.* **2015,** *5* (36), 28424-28429.

75.   Ke, W.; Fang, G.; Liu, Q.; Xiong, L.; Qin, P.; Tao, H.; Wang, J.; Lei, H.; Li, B.; Wan, J.; Yang, G.; Yan, Y., Low-Temperature Solution-Processed Tin Oxide as an Alternative Electron Transporting Layer for Efficient Perovskite Solar Cells. *Journal of the American Chemical Society* **2015,** *137* (21), 6730-6733.

76.   Ke, W.; Fang, G.; Liu, Q.; Xiong, L.; Qin, P.; Tao, H.; Wang, J.; Lei, H.; Li, B.; Wan, J., Low-temperature solution-processed tin oxide as an alternative electron

transporting layer for efficient perovskite solar cells. *Journal of the American Chemical Society* **2015,** *137* (21), 6730-6733.

77.   Zhang, L.; Wu, H. B.; Lou, X. D. W., Growth of SnO 2 nanosheet arrays on various conductive substrates as integrated electrodes for lithium-ion batteries. *Materials Horizons* **2014,** *1* (1), 133-138.

78.   Jacobsson, T. J.; Correa-Baena, J.-P.; Halvani Anaraki, E.; Philippe, B.; Stranks, S. D.; Bouduban, M. E.; Tress, W.; Schenk, K.; Teuscher, J.; Moser, J.-E., Unreacted PbI2 as a double-edged sword for enhancing the performance of perovskite solar cells. *Journal of the American Chemical Society* **2016,** *138* (32), 10331-10343.

79.   Tress, W.; Marinova, N.; Inganäs, O.; Nazeeruddin, M.; Zakeeruddin, S. M.; Graetzel, M., Predicting the Open-Circuit Voltage of CH3NH3PbI3 Perovskite Solar Cells Using Electroluminescence and Photovoltaic Quantum Efficiency Spectra: the Role of Radiative and Non-Radiative Recombination. *Advanced Energy Materials* **2015,** *5* (3).

80.   Roose, B.; Baena, J.-P. C.; Gödel, K. C.; Graetzel, M.; Hagfeldt, A.; Steiner, U.; Abate, A., Mesoporous SnO 2 electron selective contact enables UV-stable perovskite solar cells. *Nano Energy* **2016,** *30*, 517-522.

81.   Edri, E.; Kirmayer, S.; Henning, A.; Mukhopadhyay, S.; Gartsman, K.; Rosenwaks, Y.; Hodes, G.; Cahen, D., Why lead methylammonium tri-iodide perovskite-based solar cells require a mesoporous electron transporting scaffold (but not necessarily a hole conductor). *Nano letters* **2014,** *14* (2), 1000-1004.

82.   Magne, C.; Moehl, T.; Urien, M.; Grätzel, M.; Pauporte, T., Effects of ZnO film growth route and nanostructure on electron transport and recombination in dye-sensitized solar cells. *Journal of Materials Chemistry A* **2013,** *1* (6), 2079-2088.

83.   Mahmood, K.; Park, S. B.; Sung, H. J., Enhanced photoluminescence, Raman spectra and field-emission behavior of indium-doped ZnO nanostructures. *Journal of Materials Chemistry C* **2013,** *1* (18), 3138-3149.

84.   Xu, F.; Sun, L., Solution-derived ZnO nanostructures for photoanodes of dye-sensitized solar cells. *Energy & Environmental Science* **2011,** *4* (3), 818-841.

85.   Dong, X.; Hu, H.; Lin, B.; Ding, J.; Yuan, N., The effect of ALD-Zno layers on the formation of CH 3 NH 3 PbI 3 with different perovskite precursors and sintering temperatures. *Chemical Communications* **2014,** *50* (92), 14405-14408.

86.   Dualeh, A.; Tétreault, N.; Moehl, T.; Gao, P.; Nazeeruddin, M. K.; Grätzel, M., Effect of Annealing Temperature on Film Morphology of Organic–Inorganic Hybrid Pervoskite Solid-State Solar Cells. *Advanced Functional Materials* **2014,** *24* (21), 3250-3258.

87.   Kayaci, F.; Vempati, S.; Donmez, I.; Biyikli, N.; Uyar, T., Role of zinc interstitials and oxygen vacancies of ZnO in photocatalysis: a bottom-up approach to control defect density. *Nanoscale* **2014,** *6* (17), 10224-10234.

88.   Mahmood, K.; Swain, B. S.; Han, G.-S.; Kim, B.-J.; Jung, H. S., Polyethylenimine-assisted growth of high-aspect-ratio nitrogen-doped ZnO (NZO) nanorod arrays and their effect on performance of dye-sensitized solar cells. *ACS applied materials & interfaces* **2014,** *6* (13), 10028-10043.

89.   Mahmood, K.; Park, S. B., Growth and conductivity enhancement of N-doped ZnO nanorod arrays. *Journal of Crystal Growth* **2012,** *347* (1), 104-112.

90.   Dkhissi, Y.; Meyer, S.; Chen, D.; Weerasinghe, H. C.; Spiccia, L.; Cheng, Y. B.; Caruso, R. A., Stability Comparison of Perovskite Solar Cells Based on Zinc Oxide and Titania on Polymer Substrates. *ChemSusChem* **2016,** *9* (7), 687-695.

91.   Yang, J.; Siempelkamp, B. D.; Liu, D.; Kelly, T. L., Investigation of CH3NH3PbI3 Degradation Rates and Mechanisms in Controlled Humidity Environments Using in Situ Techniques. *ACS Nano* **2015,** *9* (2), 1955-1963.

92.   Irwin, M. D.; Buchholz, D. B.; Hains, A. W.; Chang, R. P.; Marks, T. J., p-Type semiconducting nickel oxide as an efficiency-enhancing anode interfacial layer in polymer bulk-heterojunction solar cells. *Proceedings of the National Academy of Sciences* **2008,** *105* (8), 2783-2787.

93.   Etgar, L.; Gao, P.; Xue, Z.; Peng, Q.; Chandiran, A. K.; Liu, B.; Nazeeruddin, M. K.; Gratzel, M., Mesoscopic CH3NH3PbI3/TiO2 Heterojunction Solar Cells. *J. Am. Chem. Soc.* **2012,** *134* (42), 17396-17399.

94.   Peumans, P.; Forrest, S., Very-high-efficiency double-heterostructure copper phthalocyanine/C 60 photovoltaic cells. *Applied Physics Letters* **2001,** *79* (1), 126-128.

95.   Jeng, J. Y.; Chiang, Y. F.; Lee, M. H.; Peng, S. R.; Guo, T. F.; Chen, P.; Wen, T. C., CH3NH3PbI3 Perovskite/Fullerene Planar-Heterojunction Hybrid Solar Cells. *Advanced Materials* **2013,** *25* (27), 3727-3732.

96.   Schwanitz, K.; Weiler, U.; Hunger, R.; Mayer, T.; Jaegermann, W., Synchrotron-induced photoelectron spectroscopy of the dye-sensitized nanocrystalline TiO2/electrolyte interface: band gap states and their interaction with dye and solvent molecules. *The Journal of Physical Chemistry C* **2007,** *111* (2), 849-854.

97.   Saliba, M.; Matsui, T.; Seo, J.-Y.; Domanski, K.; Correa-Baena, J.-P.; Nazeeruddin, M. K.; Zakeeruddin, S. M.; Tress, W.; Abate, A.; Hagfeldt, A.; Gratzel, M., Cesium-containing triple cation perovskite solar cells: improved stability, reproducibility and high efficiency. *Energy Environ. Sci.* **2016**, Ahead of Print.

98.   Ergen, O.; Gilbert, S. M.; Pham, T.; Turner, S. J.; Tan, M. T. Z.; Worsley, M. A.; Zettl, A., Graded bandgap perovskite solar cells. *Nature materials* **2017,** *16* (5), 522-525.

99.   Boix, P. P.; Agarwala, S.; Koh, T. M.; Mathews, N.; Mhaisalkar, S. G., Perovskite Solar Cells: Beyond Methylammonium Lead Iodide. *J. Phys. Chem. Lett.* **2015,** *6* (5), 898-907.

100.   Cortecchia, D.; Dewi, H. A.; Yin, J.; Bruno, A.; Chen, S.; Baikie, T.; Boix, P. P.; Grätzel, M.; Mhaisalkar, S.; Soci, C.; Mathews, N., Lead-Free MA2CuClxBr4–x Hybrid Perovskites. *Inorganic Chemistry* **2016,** *55* (3), 1044-1052.

101.   Tsai, H.; Nie, W.; Blancon, J.-C.; Stoumpos, C. C.; Asadpour, R.; Harutyunyan, B.; Neukirch, A. J.; Verduzco, R.; Crochet, J. J.; Tretiak, S., High-efficiency two-dimensional Ruddlesden–Popper perovskite solar cells. *Nature* **2016,** *536* (7616), 312-316.

102.   Frost, J. M.; Butler, K. T.; Brivio, F.; Hendon, C. H.; van Schilfgaarde, M.; Walsh, A., Atomistic Origins of High-Performance in Hybrid Halide Perovskite Solar Cells. *Nano Letters* **2014,** *14* (5), 2584-2590.

103.   Huang, W.; Manser, J. S.; Kamat, P. V.; Ptasinska, S., Evolution of Chemical Composition, Morphology, and Photovoltaic Efficiency of CH3NH3PbI3 Perovskite under Ambient Conditions. *Chemistry of Materials* **2015,** *28* (1), 303-311.

104.	Manser, J. S.; Saidaminov, M. I.; Christians, J. A.; Bakr, O. M.; Kamat, P. V., Making and Breaking of Lead Halide Perovskites. *Acc. Chem. Res.* **2016,** *49* (2), 330-338.

105.	Christians, J. A.; Miranda Herrera, P. A.; Kamat, P. V., Transformation of the excited state and photovoltaic efficiency of CH3NH3PbI3 perovskite upon controlled exposure to humidified air. *J. Am. Chem. Soc.* **2015,** *137* (4), 1530-1538.

106.	Leguy, A. l. M.; Hu, Y.; Campoy-Quiles, M.; Alonso, M. I.; Weber, O. J.; Azarhoosh, P.; Van Schilfgaarde, M.; Weller, M. T.; Bein, T.; Nelson, J., Reversible hydration of CH3NH3PbI3 in films, single crystals, and solar cells. *Chemistry of Materials* **2015,** *27* (9), 3397-3407.

107.	Niu, G.; Li, W.; Meng, F.; Wang, L.; Dong, H.; Qiu, Y., Study on the stability of CH3NH3PbI3 films and the effect of post-modification by aluminum oxide in all-solid-state hybrid solar cells. *Journal of Materials Chemistry A* **2014,** *2* (3), 705-710.

108.	O'Mahony, F. T.; Lee, Y. H.; Jellett, C.; Dmitrov, S.; Bryant, D. T.; Durrant, J. R.; O'Regan, B. C.; Graetzel, M.; Nazeeruddin, M. K.; Haque, S. A., Improved environmental stability of organic lead trihalide perovskite-based photoactive-layers in the presence of mesoporous TiO 2. *Journal of Materials Chemistry A* **2015,** *3* (14), 7219-7223.

109.	Aristidou, N.; Sanchez-Molina, I.; Chotchuangchutchaval, T.; Brown, M.; Martinez, L.; Rath, T.; Haque, S. A., The Role of Oxygen in the Degradation of Methylammonium Lead Trihalide Perovskite Photoactive Layers. *Angew. Chem., Int. Ed.* **2015,** *54* (28), 8208-8212.

110.	Edri, E.; Kirmayer, S.; Cahen, D.; Hodes, G., High open-circuit voltage solar cells based on organic–inorganic lead bromide perovskite. *The journal of physical chemistry letters* **2013,** *4* (6), 897-902.

111.	Edri, E.; Kirmayer, S.; Kulbak, M.; Hodes, G.; Cahen, D., Chloride inclusion and hole transport material doping to improve methyl ammonium lead bromide perovskite-based high open-circuit voltage solar cells. *The journal of physical chemistry letters* **2014,** *5* (3), 429-433.

112.	Heo, J. H.; Song, D. H.; Im, S. H., Planar CH3NH3PbBr3 Hybrid Solar Cells with 10.4% Power Conversion Efficiency, Fabricated by Controlled Crystallization in the Spin-Coating Process. *Advanced Materials* **2014,** *26* (48), 8179-8183.

113.	D'Innocenzo, V.; Grancini, G.; Alcocer, M. J.; Kandada, A. R. S.; Stranks, S. D.; Lee, M. M.; Lanzani, G.; Snaith, H. J.; Petrozza, A., Excitons versus free charges in organo-lead tri-halide perovskites. *Nature communications* **2014,** *5.*

114.	Stranks, S. D.; Eperon, G. E.; Grancini, G.; Menelaou, C.; Alcocer, M. J.; Leijtens, T.; Herz, L. M.; Petrozza, A.; Snaith, H. J., Electron-hole diffusion lengths exceeding 1 micrometer in an organometal trihalide perovskite absorber. *Science* **2013,** *342* (6156), 341-344.

115.	Liu, M.; Johnston, M. B.; Snaith, H. J., Efficient planar heterojunction perovskite solar cells by vapour deposition. *Nature (London, U. K.)* **2013,** *501* (7467), 395-398.

116.	Maalej, A.; Abid, Y.; Kallel, A.; Daoud, A.; Lautié, A.; Romain, F., Phase transitions and crystal dynamics in the cubic perovskite CH 3 NH 3 PbCl 3. *Solid state communications* **1997,** *103* (5), 279-284.

117.   Yin, W. J.; Shi, T.; Yan, Y., Unique properties of halide perovskites as possible origins of the superior solar cell performance. *Advanced Materials* **2014,** *26* (27), 4653-4658.

118.   Zhang, W.; Saliba, M.; Moore, D. T.; Pathak, S. K.; Hörantner, M. T.; Stergiopoulos, T.; Stranks, S. D.; Eperon, G. E.; Alexander-Webber, J. A.; Abate, A.; Sadhanala, A.; Yao, S.; Chen, Y.; Friend, R. H.; Estroff, L. A.; Wiesner, U.; Snaith, H. J., Ultrasmooth organic–inorganic perovskite thin-film formation and crystallization for efficient planar heterojunction solar cells. *Nat Commun* **2015,** *6*.

119.   Hao, F.; Stoumpos, C. C.; Chang, R. P.; Kanatzidis, M. G., Anomalous band gap behavior in mixed Sn and Pb perovskites enables broadening of absorption spectrum in solar cells. *Journal of the American Chemical Society* **2014,** *136* (22), 8094-8099.

120.   Noel, N. K.; Stranks, S. D.; Abate, A.; Wehrenfennig, C.; Guarnera, S.; Haghighirad, A.-A.; Sadhanala, A.; Eperon, G. E.; Pathak, S. K.; Johnston, M. B., Lead-free organic–inorganic tin halide perovskites for photovoltaic applications. *Energy & Environmental Science* **2014,** *7* (9), 3061-3068.

121.   Zuo, F.; Williams, S. T.; Liang, P. W.; Chueh, C. C.; Liao, C. Y.; Jen, A. K. Y., Binary-Metal Perovskites Toward High-Performance Planar-Heterojunction Hybrid Solar Cells. *Advanced Materials* **2014,** *26* (37), 6454-6460.

122.   Zhu, H. L.; Xiao, J.; Mao, J.; Zhang, H.; Zhao, Y.; Choy, W. C., Controllable Crystallization of CH3NH3Sn0. 25Pb0. 75I3 Perovskites for Hysteresis-Free Solar Cells with Efficiency Reaching 15.2%. *Advanced Functional Materials* **2017**.

123.   Kumar, M. H.; Dharani, S.; Leong, W. L.; Boix, P. P.; Prabhakar, R. R.; Baikie, T.; Shi, C.; Ding, H.; Ramesh, R.; Asta, M., Lead-Free Halide Perovskite Solar Cells with High Photocurrents Realized Through Vacancy Modulation. *Advanced Materials* **2014,** *26* (41), 7122-7127.

124.   Sabba, D.; Mulmudi, H. K.; Prabhakar, R. R.; Krishnamoorthy, T.; Baikie, T.; Boix, P. P.; Mhaisalkar, S.; Mathews, N., Impact of Anionic Br- Substitution on Open Circuit Voltage in Lead Free Perovskite (CsSnI3-xBrx) Solar Cells. *J. Phys. Chem. C* **2015,** *119* (4), 1763-1767.

125.   Tang, L.-C.; Chang, C.-S.; Huang, J. Y., Electronic structure and optical properties of rhombohedral CsGeI3 crystal. *Journal of Physics: Condensed Matter* **2000,** *12* (43), 9129.

126.   Tang, L. C.; Huang, J. Y.; Chang, C.; Lee, M.; Liu, L., New infrared nonlinear optical crystal CsGeBr3: synthesis, structure and powder second-harmonic generation properties. *Journal of Physics: Condensed Matter* **2005,** *17* (46), 7275.

127.   Cheng, Z.; Lin, J., Layered organic–inorganic hybrid perovskites: structure, optical properties, film preparation, patterning and templating engineering. *CrystEngComm* **2010,** *12* (10), 2646-2662.

128.   Li, C.; Lu, X.; Ding, W.; Feng, L.; Gao, Y.; Guo, Z., Formability of ABX3 (X= F, Cl, Br, I) Halide Perovskites. *Acta Crystallographica Section B: Structural Science* **2008,** *64* (6), 702-707.

129.   Lee, J. W.; Seol, D. J.; Cho, A. N.; Park, N. G., High-Efficiency Perovskite Solar Cells Based on the Black Polymorph of HC (NH2) 2PbI3. *Advanced Materials* **2014,** *26* (29), 4991-4998.

130.   Pellet, N.; Gao, P.; Gregori, G.; Yang, T. Y.; Nazeeruddin, M. K.; Maier, J.; Grätzel, M., Mixed-organic-cation Perovskite photovoltaics for enhanced solar-light harvesting. *Angewandte Chemie International Edition* **2014,** *53* (12), 3151-3157.

131.   Hanusch, F. C.; Wiesenmayer, E.; Mankel, E.; Binek, A.; Angloher, P.; Fraunhofer, C.; Giesbrecht, N.; Feckl, J. M.; Jaegermann, W.; Johrendt, D., Efficient planar heterojunction perovskite solar cells based on formamidinium lead bromide. *The journal of physical chemistry letters* **2014,** *5* (16), 2791-2795.

132.   Im, J.-H.; Chung, J.; Kim, S.-J.; Park, N.-G., Synthesis, structure, and photovoltaic property of a nanocrystalline 2H perovskite-type novel sensitizer (CH 3 CH 2 NH 3) PbI 3. *Nanoscale research letters* **2012,** *7* (1), 1.

133.   Kieslich, G.; Sun, S.; Cheetham, A. K., Solid-state principles applied to organic–inorganic perovskites: new tricks for an old dog. *Chemical Science* **2014,** *5* (12), 4712-4715.

134.   Eperon, G. E.; Paterno, G. M.; Sutton, R. J.; Zampetti, A.; Haghighirad, A. A.; Cacialli, F.; Snaith, H. J., Inorganic cesium lead iodide perovskite solar cells. *J. Mater. Chem. A* **2015,** *3* (39), 19688-19695.

135.   Yi, C.; Luo, J.; Meloni, S.; Boziki, A.; Ashari-Astani, N.; Gratzel, C.; Zakeeruddin, S. M.; Rothlisberger, U.; Gratzel, M., Entropic stabilization of mixed A-cation ABX3 metal halide perovskites for high performance perovskite solar cells. *Energy & Environmental Science* **2016,** *9* (2), 656-662.

136.   Umari, P.; Mosconi, E.; De Angelis, F., Relativistic GW calculations on CH3NH3PbI3 and CH3NH3SnI3 perovskites for solar cell applications. *Scientific reports* **2014,** *4*, 4467.

137.   Bernal, C.; Yang, K., First-principles hybrid functional study of the organic–inorganic perovskites CH3NH3SnBr3 and CH3NH3SnI3. *The Journal of Physical Chemistry C* **2014,** *118* (42), 24383-24388.

138.   Stoumpos, C. C.; Malliakas, C. D.; Kanatzidis, M. G., Semiconducting Tin and Lead Iodide Perovskites with Organic Cations: Phase Transitions, High Mobilities, and Near-Infrared Photoluminescent Properties. *Inorganic Chemistry* **2013,** *52* (15), 9019-9038.

139.   Takahashi, Y.; Obara, R.; Lin, Z.-Z.; Takahashi, Y.; Naito, T.; Inabe, T.; Ishibashi, S.; Terakura, K., Charge-transport in tin-iodide perovskite CH 3 NH 3 SnI 3: origin of high conductivity. *Dalton Transactions* **2011,** *40* (20), 5563-5568.

140.   He, M.; Zheng, D.; Wang, M.; Lin, C.; Lin, Z., High efficiency perovskite solar cells: from complex nanostructure to planar heterojunction. *Journal of Materials Chemistry A* **2014,** *2* (17), 5994-6003.

141.   Cai, B.; Xing, Y.; Yang, Z.; Zhang, W.-H.; Qiu, J., High performance hybrid solar cells sensitized by organolead halide perovskites. *Energy & Environmental Science* **2013,** *6* (5), 1480-1485.

142.   De Wolf, S.; Holovsky, J.; Moon, S.-J.; Löper, P.; Niesen, B.; Ledinsky, M.; Haug, F.-J.; Yum, J.-H.; Ballif, C., Organometallic halide perovskites: sharp optical absorption edge and its relation to photovoltaic performance. *The Journal of Physical Chemistry Letters* **2014,** *5* (6), 1035-1039.

143.   Cao, D. H.; Stoumpos, C. C.; Farha, O. K.; Hupp, J. T.; Kanatzidis, M. G., 2D Homologous Perovskites as Light-Absorbing Materials for Solar Cell Applications. *Journal of the American Chemical Society* **2015,** *137* (24), 7843-7850.

144.   Ishihara, T., Optical properties of PbI-based perovskite structures. *Journal of luminescence* **1994,** *60*, 269-274.

145.   Smith, I. C.; Hoke, E. T.; Solis-Ibarra, D.; McGehee, M. D.; Karunadasa, H. I., A Layered Hybrid Perovskite Solar Cell Absorber with Enhanced Moisture Stability. *Angew. Chem., Int. Ed.* **2014,** *53* (42), 11232-11235.

146.   Choi, H.; Paek, S.; Lim, N.; Lee, Y.; Nazeeruddin, M. K.; Ko, J., Efficient perovskite solar cells with 13.63 % efficiency based on planar triphenylamine hole conductors. *Chem. - Eur. J.* **2014,** *20* (35), 10894-10899.

147.   Habisreutinger, S. N.; Leijtens, T.; Eperon, G. E.; Stranks, S. D.; Nicholas, R. J.; Snaith, H. J., Carbon Nanotube/Polymer Composites as a Highly Stable Hole Collection Layer in Perovskite Solar Cells. *Nano Lett.* **2014,** *14* (10), 5561-5568.

148.   Nejand, B. A.; Ahmadi, V.; Gharibzadeh, S.; Shahverdi, H. R., Cuprous Oxide as a Potential Low-Cost Hole-Transport Material for Stable Perovskite Solar Cells. *ChemSusChem* **2016,** *9* (3), 302-313.

149.   Zuo, C.; Ding, L., Solution-Processed Cu2O and CuO as Hole Transport Materials for Efficient Perovskite Solar Cells. *Small* **2015,** *11* (41), 5528-5532.

150.   Ye, S.; Sun, W.; Li, Y.; Yan, W.; Peng, H.; Bian, Z.; Liu, Z.; Huang, C., CuSCN-Based Inverted Planar Perovskite Solar Cell with an Average PCE of 15.6%. *Nano Lett.* **2015,** *15* (6), 3723-3728.

151.   Chen, W.-Y.; Deng, L.-L.; Dai, S.-M.; Wang, X.; Tian, C.-B.; Zhan, X.-X.; Xie, S.-Y.; Huang, R.-B.; Zheng, L.-S., Low-cost solution-processed copper iodide as an alternative to PEDOT: PSS hole transport layer for efficient and stable inverted planar heterojunction perovskite solar cells. *Journal of Materials Chemistry A* **2015,** *3* (38), 19353-19359.

152.   Park, J. H.; Seo, J.; Park, S.; Shin, S. S.; Kim, Y. C.; Jeon, N. J.; Shin, H. W.; Ahn, T. K.; Noh, J. H.; Yoon, S. C., Efficient CH3NH3PbI3 Perovskite Solar Cells Employing Nanostructured p-Type NiO Electrode Formed by a Pulsed Laser Deposition. *Advanced Materials* **2015,** *27* (27), 4013-4019.

153.   Li, H.; Fu, K.; Hagfeldt, A.; Grätzel, M.; Mhaisalkar, S. G.; Grimsdale, A. C., A Simple 3, 4-Ethylenedioxythiophene Based Hole-Transporting Material for Perovskite Solar Cells. *Angewandte Chemie International Edition* **2014,** *53* (16), 4085-4088.

154.   Lim, I.; Kim, E.-K.; Patil, S. A.; Ahn, D. Y.; Lee, W.; Shrestha, N. K.; Lee, J. K.; Seok, W. K.; Cho, C.-G.; Han, S.-H., Indolocarbazole based small molecules: an efficient hole transporting material for perovskite solar cells. *RSC Adv.* **2015,** *5* (68), 55321-55327.

155.   Petrus, M. L.; Bein, T.; Dingemans, T. J.; Docampo, P., A low cost azomethine-based hole transporting material for perovskite photovoltaics. *J. Mater. Chem. A* **2015,** *3* (23), 12159-12162.

156.   Reddy, S. S.; Gunasekar, K.; Heo, J. H.; Im, S. H.; Kim, C. S.; Kim, D.-H.; Moon, J. H.; Lee, J. Y.; Song, M.; Jin, S.-H., Highly Efficient Organic Hole Transporting Materials for Perovskite and Organic Solar Cells with Long-Term Stability. *Adv. Mater. (Weinheim, Ger.)* **2016,** *28* (4), 686-693.

157.   Wei, Z.; Chen, H.; Yan, K.; Zheng, X.; Yang, S., Hysteresis-free multi-walled carbon nanotube-based perovskite solar cells with a high fill factor. *J. Mater. Chem. A* **2015,** *3* (48), 24226-24231.

158.   Yan, W.; Li, Y.; Ye, S.; Li, Y.; Rao, H.; Liu, Z.; Wang, S.; Bian, Z.; Huang, C., Increasing open circuit voltage by adjusting work function of hole-transporting materials in perovskite solar cells. *Nano Research* **2016**, 1-9.

159.   Wei, H.; Shi, J.; Xu, X.; Xiao, J.; Luo, J.; Dong, J.; Lv, S.; Zhu, L.; Wu, H.; Li, D.; Luo, Y.; Meng, Q.; Chen, Q., Enhanced charge collection with ultrathin AlOx electron blocking layer for hole-transporting material-free perovskite solar cell. *Phys Chem Chem Phys* **2015,** *17* (7), 4937-44.

160.   Choi, H.; Mai, C.-K.; Kim, H.-B.; Jeong, J.; Song, S.; Bazan, G. C.; Kim, J. Y.; Heeger, A. J., Conjugated polyelectrolyte hole transport layer for inverted-type perovskite solar cells. *Nat. Commun.* **2015,** *6*, 7348.

161.   Jung, M.; Kim, Y. C.; Jeon, N. J.; Yang, W. S.; Seo, J.; Noh, J. H.; Il Seok, S., Thermal Stability of CuSCN Hole Conductor-Based Perovskite Solar Cells. *ChemSusChem* **2016,** *9* (18), 2592-2596.

162.   Wang, Y.; Rho, W.-Y.; Yang, H.-Y.; Mahmoudi, T.; Seo, S.; Lee, D.-H.; Hahn, Y.-B., Air-stable, hole-conductor-free high photocurrent perovskite solar cells with CH 3 NH 3 PbI 3–NiO nanoparticles composite. *Nano Energy* **2016,** *27*, 535-544.

163.   Yeo, J.-S.; Kang, R.; Lee, S.; Jeon, Y.-J.; Myoung, N.; Lee, C.-L.; Kim, D.-Y.; Yun, J.-M.; Seo, Y.-H.; Kim, S.-S.; Na, S.-I., Highly efficient and stable planar perovskite solar cells with reduced graphene oxide nanosheets as electrode interlayer. *Nano Energy* **2015,** *12*, 96-104.

164.   Wang, B.; Zhang, Z.-g.; Ye, S.; Gao, L.; Yan, T.; Bian, Z.; Huang, C.; Li, Y., Solution-Processable Cathode Buffer Layer for High-Performance ITO/CuSCN-based Planar Heterojunction Perovskite Solar Cell. *Electrochimica Acta* **2016,** *218*, 263-270.

165.   Hossain, M. I.; Alharbi, F. H.; Tabet, N., Copper oxide as inorganic hole transport material for lead halide perovskite based solar cells. *Solar Energy* **2015,** *120*, 370-380.

166.   Nogueira, A.; Longo, C.; De Paoli, M.-A., Polymers in dye sensitized solar cells: overview and perspectives. *Coordination Chemistry Reviews* **2004,** *248* (13), 1455-1468.

167.   Pudzich, R.; Fuhrmann-Lieker, T.; Salbeck, J., Spiro compounds for organic electroluminescence and related applications. In *Emissive Materials Nanomaterials*, Springer: 2006; pp 83-142.

168.   Malinauskas, T.; Tomkute-Luksiene, D.; Sens, R. d.; Daskeviciene, M.; Send, R.; Wonneberger, H.; Jankauskas, V.; Bruder, I.; Getautis, V., Enhancing thermal stability and lifetime of solid-state dye-sensitized solar cells via molecular engineering of the hole-transporting material Spiro-OMeTAD. *ACS applied materials & interfaces* **2015,** *7* (21), 11107-11116.

169.   Mulholland, M. E.; Navarathne, D.; Petrus, M. L.; Dingemans, T. J.; Skene, W., Correlating on-substrate prepared electrochromes with their solution processed counterparts–towards validating polyazomethines as electrochromes in functioning devices. *Journal of Materials Chemistry C* **2014,** *2* (43), 9099-9108.

170.   Sicard, L.; Navarathne, D.; Skalski, T.; Skene, W., On-Substrate Preparation of an Electroactive Conjugated Polyazomethine from Solution-Processable Monomers and its Application in Electrochromic Devices. *Advanced Functional Materials* **2013,** *23* (28), 3549-3559.

171.   Yang, C. J.; Jenekhe, S. A., Conjugated aromatic poly (azomethines). 1. Characterization of structure, electronic spectra, and processing of thin films from soluble complexes. *Chemistry of Materials* **1991,** *3* (5), 878-887.

172.   Petrus, M.; Bouwer, R.; Lafont, U.; Athanasopoulos, S.; Greenham, N.; Dingemans, T., Small-molecule azomethines: organic photovoltaics via Schiff base condensation chemistry. *Journal of Materials Chemistry A* **2014,** *2* (25), 9474-9477.

173.   Niu, H.; Cai, J.; Zhao, P.; Wang, C.; Bai, X.; Wang, W., Simple approach to regulate the spectra of novel kinds of polyazomethines containing bulky triphenylamine: electrochemistry, electrochromism and photophysical responsive to environment. *Dyes and Pigments* **2013,** *96* (1), 158-169.

174.   Janeliunas, D.; van Rijn, P.; Boekhoven, J.; Minkenberg, C. B.; van Esch, J. H.; Eelkema, R., Aggregation-Driven Reversible Formation of Conjugated Polymers in Water. *Angewandte Chemie International Edition* **2013,** *52* (7), 1998-2001.

175.   Yang, L.; Xu, B.; Bi, D.; Tian, H.; Boschloo, G.; Sun, L.; Hagfeldt, A.; Johansson, E. M., Initial light soaking treatment enables hole transport material to outperform spiro-OMeTAD in solid-state dye-sensitized solar cells. *Journal of the American Chemical Society* **2013,** *135* (19), 7378-7385.

176.   Walzer, K.; Maennig, B.; Pfeiffer, M.; Leo, K., Highly efficient organic devices based on electrically doped transport layers. *Chemical reviews* **2007,** *107* (4), 1233-1271.

177.   Xu, B.; Sheibani, E.; Liu, P.; Zhang, J.; Tian, H.; Vlachopoulos, N.; Boschloo, G.; Kloo, L.; Hagfeldt, A.; Sun, L., Carbazole-Based Hole-Transport Materials for Efficient Solid-State Dye-Sensitized Solar Cells and Perovskite Solar Cells. *Advanced Materials* **2014,** *26* (38), 6629-6634.

178.   Chen, L. M.; Hong, Z.; Li, G.; Yang, Y., Recent progress in polymer solar cells: manipulation of polymer: fullerene morphology and the formation of efficient inverted polymer solar cells. *Advanced Materials* **2009,** *21* (14-15), 1434-1449.

179.   Hou, F.; Su, Z.; Jin, F.; Yan, X.; Wang, L.; Zhao, H.; Zhu, J.; Chu, B.; Li, W., Efficient and stable planar heterojunction perovskite solar cells with an MoO3/PEDOT:PSS hole transporting layer. *Nanoscale* **2015,** *7* (21), 9427-9432.

180.   Igbari, F.; Li, M.; Hu, Y.; Wang, Z.-K.; Liao, L.-S., A room-temperature CuAlO2 hole interfacial layer for efficient and stable planar perovskite solar cells. *J. Mater. Chem. A* **2016,** *4* (4), 1326-1335.

181.   Yan, W.; Li, Y.; Li, Y.; Ye, S.; Liu, Z.; Wang, S.; Bian, Z.; Huang, C., Stable high-performance hybrid perovskite solar cells with ultrathin polythiophene as hole-transporting layer. *Nano Res.* **2015,** *8* (8), 2474-2480.

182.   Cai, M.; Tiong, V. T.; Hreid, T.; Bell, J.; Wang, H., An efficient hole transport material composite based on poly(3-hexylthiophene) and bamboo-structured carbon nanotubes for high performance perovskite solar cells. *J. Mater. Chem. A* **2015,** *3* (6), 2784-2793.

183.   Obrzut, J.; Page, K. A., Electrical conductivity and relaxation in poly (3-hexylthiophene). *Physical Review B* **2009,** *80* (19), 195211.

184.   Geng, J.; Zeng, T., Influence of single-walled carbon nanotubes induced crystallinity enhancement and morphology change on polymer photovoltaic devices. *Journal of the American Chemical Society* **2006,** *128* (51), 16827-16833.

185.   Christians, J. A.; Fung, R. C.; Kamat, P. V., An inorganic hole conductor for organo-lead halide perovskite solar cells. Improved hole conductivity with copper iodide. *J Am Chem Soc* **2014,** *136* (2), 758-64.

186. Qin, P.; Tanaka, S.; Ito, S.; Tetreault, N.; Manabe, K.; Nishino, H.; Nazeeruddin, M. K.; Grätzel, M., Inorganic hole conductor-based lead halide perovskite solar cells with 12.4% conversion efficiency. *Nature communications* **2014,** *5*.

187. Subbiah, A. S.; Halder, A.; Ghosh, S.; Mahuli, N.; Hodes, G.; Sarkar, S. K., Inorganic hole conducting layers for perovskite-based solar cells. *The journal of physical chemistry letters* **2014,** *5* (10), 1748-1753.

188. Hu, L.; Peng, J.; Wang, W.; Xia, Z.; Yuan, J.; Lu, J.; Huang, X.; Ma, W.; Song, H.; Chen, W., Sequential deposition of CH3NH3PbI3 on planar NiO film for efficient planar perovskite solar cells. *Acs Photonics* **2014,** *1* (7), 547-553.

189. Malerba, C.; Biccari, F.; Ricardo, C. L. A.; D'Incau, M.; Scardi, P.; Mittiga, A., Absorption coefficient of bulk and thin film Cu 2 O. *Solar energy materials and solar cells* **2011,** *95* (10), 2848-2854.

190. Musa, A.; Akomolafe, T.; Carter, M., Production of cuprous oxide, a solar cell material, by thermal oxidation and a study of its physical and electrical properties. *Solar Energy Materials and Solar Cells* **1998,** *51* (3), 305-316.

191. Ito, T.; Yamaguchi, H.; Okabe, K.; Masumi, T., Single-crystal growth and characterization of Cu2O and CuO. *Journal of materials science* **1998,** *33* (14), 3555-3566.

192. Scanlon, D. O.; Morgan, B. J.; Watson, G. W., Modeling the polaronic nature of p-type defects in Cu 2 O: The failure of GGA and GGA+ U. *The Journal of chemical physics* **2009,** *131* (12), 124703.

193. Figueiredo, V.; Elangovan, E.; Goncalves, G.; Barquinha, P.; Pereira, L.; Franco, N.; Alves, E.; Martins, R.; Fortunato, E., Effect of post-annealing on the properties of copper oxide thin films obtained from the oxidation of evaporated metallic copper. *Applied Surface Science* **2008,** *254* (13), 3949-3954.

194. O'Regan, B.; Schwartz, D. T.; Zakeeruddin, S. M.; Grätzel, M., Electrodeposited Nanocomposite n–p Heterojunctions for Solid-State Dye-Sensitized Photovoltaics. *Advanced Materials* **2000,** *12* (17), 1263-1267.

195. Ito, S.; Tsujimoto, K.; Nguyen, D.-C.; Manabe, K.; Nishino, H., Doping effects in Sb 2 S 3 absorber for full-inorganic printed solar cells with 5.7% conversion efficiency. *International Journal of Hydrogen Energy* **2013,** *38* (36), 16749-16754.

196. Pattanasattayavong, P.; Yaacobi-Gross, N.; Zhao, K.; Ndjawa, G. O. N.; Li, J.; Yan, F.; O'Regan, B. C.; Amassian, A.; Anthopoulos, T. D., Hole-Transporting Transistors and Circuits Based on the Transparent Inorganic Semiconductor Copper (I) Thiocyanate (CuSCN) Processed from Solution at Room Temperature. *Advanced Materials* **2013,** *25* (10), 1504-1509.

197. Pattanasattayavong, P.; Ndjawa, G. O. N.; Zhao, K.; Chou, K. W.; Yaacobi-Gross, N.; O'Regan, B. C.; Amassian, A.; Anthopoulos, T. D., Electric field-induced hole transport in copper (I) thiocyanate (CuSCN) thin-films processed from solution at room temperature. *Chemical Communications* **2013,** *49* (39), 4154-4156.

198. Kim, J. H.; Liang, P.-W.; Williams, S. T.; Cho, N.; Chueh, C.-C.; Glaz, M. S.; Ginger, D. S.; Jen, A. K. Y., High-performance and environmentally stable planar heterojunction perovskite solar cells based on a solution-processed copper-doped nickel oxide hole-transporting layer. *Adv Mater* **2015,** *27* (4), 695-701.

199. Wang, K.-C.; Shen, P.-S.; Li, M.-H.; Chen, S.; Lin, M.-W.; Chen, P.; Guo, T.-F., Low-Temperature Sputtered Nickel Oxide Compact Thin Film as Effective Electron

Blocking Layer for Mesoscopic NiO/CH3NH3PbI3 Perovskite Heterojunction Solar Cells. *ACS Appl. Mater. Interfaces* **2014,** *6* (15), 11851-11858.

200.   Deng, Y.; Peng, E.; Shao, Y.; Xiao, Z.; Dong, Q.; Huang, J., Scalable fabrication of efficient organolead trihalide perovskite solar cells with doctor-bladed active layers. *Energy Environ. Sci.* **2015,** *8* (5), 1544-1550.

201.   Chang, C.-Y.; Tsai, B.-C.; Hsiao, Y.-C.; Huang, Y.-C.; Tsao, C.-S., High-performance printable hybrid perovskite solar cells with an easily accessible n-doped fullerene as a cathode interfacial layer. *Physical Chemistry Chemical Physics* **2016,** *18* (46), 31836-31844.

202.   Yang, M.; Li, Z.; Reese, M. O.; Reid, O. G.; Kim, D. H.; Siol, S.; Klein, T. R.; Yan, Y.; Berry, J. J.; van Hest, M. F., Perovskite ink with wide processing window for scalable high-efficiency solar cells. *Nature Energy* **2017,** *2* (NREL/JA-5900-67357).

203.   Chang, X.; Li, W.; Chen, H.; Zhu, L.; Liu, H.; Geng, H.; Xiang, S.; Liu, J.; Zheng, X.; Yang, Y., Colloidal Precursor-Induced Growth of Ultra-Even CH3NH3PbI3 for High-Performance Paintable Carbon-Based Perovskite Solar Cells. *ACS Applied Materials & Interfaces* **2016,** *8* (44), 30184-30192.

204.   Li, S.-G.; Jiang, K.-J.; Su, M.-J.; Cui, X.-P.; Huang, J.-H.; Zhang, Q.-Q.; Zhou, X.-Q.; Yang, L.-M.; Song, Y.-L., Inkjet printing of CH 3 NH 3 PbI 3 on a mesoscopic TiO 2 film for highly efficient perovskite solar cells. *Journal of Materials Chemistry A* **2015,** *3* (17), 9092-9097.

205.   Mathies, F.; Abzieher, T.; Hochstuhl, A.; Glaser, K.; Colsmann, A.; Paetzold, U. W.; Hernandez-Sosa, G.; Lemmer, U.; Quintilla, A., Multipass inkjet printed planar methylammonium lead iodide perovskite solar cells. *Journal of Materials Chemistry A* **2016,** *4* (48), 19207-19213.

206.   Hashmi, S. G.; Tiihonen, A.; Martineau, D.; Ozkan, M.; Vivo, P.; Kaunisto, K.; Ulla, V.; Zakeeruddin, S. M.; Grätzel, M., Long term stability of air processed inkjet infiltrated carbon-based printed perovskite solar cells under intense ultra-violet light soaking. *Journal of Materials Chemistry A* **2017,** *5* (10), 4797-4802.

207.   Barrows, A. T.; Pearson, A. J.; Kwak, C. K.; Dunbar, A. D.; Buckley, A. R.; Lidzey, D. G., Efficient planar heterojunction mixed-halide perovskite solar cells deposited via spray-deposition. *Energy & Environmental Science* **2014,** *7* (9), 2944-2950.

208.   Das, S.; Yang, B.; Gu, G.; Joshi, P. C.; Ivanov, I. N.; Rouleau, C. M.; Aytug, T.; Geohegan, D. B.; Xiao, K., High-performance flexible perovskite solar cells by using a combination of ultrasonic spray-coating and low thermal budget photonic curing. *ACS Photonics* **2015,** *2* (6), 680-686.

209.   Heo, J. H.; Lee, M. H.; Jang, M. H.; Im, S. H., Highly efficient CH 3 NH 3 PbI 3−x Cl x mixed halide perovskite solar cells prepared by re-dissolution and crystal grain growth via spray coating. *Journal of Materials Chemistry A* **2016,** *4* (45), 17636-17642.

210.   Remeika, M.; Raga, S. R.; Zhang, S.; Qi, Y., Transferrable optimization of spray-coated PbI 2 films for perovskite solar cell fabrication. *Journal of Materials Chemistry A* **2017,** *5* (12), 5709-5718.

211.   Tenent, R. C.; Barnes, T. M.; Bergeson, J. D.; Ferguson, A. J.; To, B.; Gedvilas, L. M.; Heben, M. J.; Blackburn, J. L., Ultrasmooth, Large-Area, High-Uniformity, Conductive Transparent Single-Walled-Carbon-Nanotube Films for Photovoltaics Produced by Ultrasonic Spraying. *Advanced materials* **2009,** *21* (31), 3210-3216.

212.   Shao, M.; Das, S.; Xiao, K.; Chen, J.; Keum, J. K.; Ivanov, I. N.; Gu, G.; Durant, W.; Li, D.; Geohegan, D. B., High-performance organic field-effect transistors with dielectric and active layers printed sequentially by ultrasonic spraying. *Journal of Materials Chemistry C* **2013,** *1* (28), 4384-4390.

213.   Lefort, M.; Popa, G.; Seyrek, E.; Szamocki, R.; Felix, O.; Hemmerlé, J.; Vidal, L.; Voegel, J. C.; Boulmedais, F.; Decher, G., Spray-On Organic/Inorganic Films: A General Method for the Formation of Functional Nano-to Microscale Coatings. *Angewandte Chemie International Edition* **2010,** *49* (52), 10110-10113.

214.   Ishikawa, T.; Nakamura, M.; Fujita, K.; Tsutsui, T., Preparation of organic bulk heterojunction photovoltaic cells by evaporative spray deposition from ultradilute solution. *Applied physics letters* **2004,** *84* (13), 2424-2426.

215.   Chen, L.-M.; Hong, Z.; Kwan, W. L.; Lu, C.-H.; Lai, Y.-F.; Lei, B.; Liu, C.-P.; Yang, Y., Multi-source/component spray coating for polymer solar cells. *ACS nano* **2010,** *4* (8), 4744-4752.

216.   Girotto, C.; Rand, B. P.; Genoe, J.; Heremans, P., Exploring spray coating as a deposition technique for the fabrication of solution-processed solar cells. *Solar Energy Materials and Solar Cells* **2009,** *93* (4), 454-458.

217.   Wang, T.; Scarratt, N. W.; Yi, H.; Dunbar, A. D.; Pearson, A. J.; Watters, D. C.; Glen, T. S.; Brook, A. C.; Kingsley, J.; Buckley, A. R., Fabricating High Performance, Donor–Acceptor Copolymer Solar Cells by Spray-Coating in Air. *Advanced Energy Materials* **2013,** *3* (4), 505-512.

218.   Barrows, A. T.; Pearson, A. J.; Kwak, C. K.; Dunbar, A. D. F.; Buckley, A. R.; Lidzey, D. G., Efficient planar heterojunction mixed-halide perovskite solar cells deposited via spray-deposition. *Energy Environ. Sci.* **2014,** *7* (9), 2944-2950.

219.   Huang, H.; Shi, J.; Zhu, L.; Li, D.; Luo, Y.; Meng, Q., Two-step ultrasonic spray deposition of CH 3 NH 3 PbI 3 for efficient and large-area perovskite solar cell. *Nano Energy* **2016,** *27*, 352-358.

220.   Wu, Y.; Islam, A.; Yang, X.; Qin, C.; Liu, J.; Zhang, K.; Peng, W.; Han, L., Retarding the crystallization of PbI 2 for highly reproducible planar-structured perovskite solar cells via sequential deposition. *Energy & Environmental Science* **2014,** *7* (9), 2934-2938.

221.   Li, W.; Fan, J.; Li, J.; Mai, Y.; Wang, L., Controllable grain morphology of perovskite absorber film by molecular self-assembly toward efficient solar cell exceeding 17%. *Journal of the American Chemical Society* **2015,** *137* (32), 10399-10405.

222.   Wakamiya, A.; Endo, M.; Sasamori, T.; Tokitoh, N.; Ogomi, Y.; Hayase, S.; Murata, Y., Reproducible fabrication of efficient perovskite-based solar cells: X-ray crystallographic studies on the formation of CH3NH3PbI3 layers. *Chemistry Letters* **2014,** *43* (5), 711-713.

223.   Tait, J. G.; Manghooli, S.; Qiu, W.; Rakocevic, L.; Kootstra, L.; Jaysankar, M.; Masse de la Huerta, C. A.; Paetzold, U. W.; Gehlhaar, R.; Cheyns, D.; Heremans, P.; Poortmans, J., Rapid composition screening for perovskite photovoltaics via concurrently pumped ultrasonic spray coating. *J. Mater. Chem. A* **2016,** *4* (10), 3792-3797.

224.   Abdollahi Nejand, B.; Gharibzadeh, S.; Ahmadi, V.; Shahverdi, H. R., New Scalable Cold-Roll Pressing for Post-treatment of Perovskite Microstructure in Perovskite Solar Cells. *The Journal of Physical Chemistry C* **2016,** *120* (5), 2520-2528.

225.   Nejand, B. A.; Gharibzadeh, S.; Ahmadi, V.; Shahverdi, H. R., Novel Solvent-free Perovskite Deposition in Fabrication of Normal and Inverted Architectures of Perovskite Solar Cells. *Scientific Reports* **2016,** *6*.

226.   Brown, T.; De Rossi, F.; Di Giacomo, F.; Mincuzzi, G.; Zardetto, V.; Reale, A.; Di Carlo, A., Progress in flexible dye solar cell materials, processes and devices. *Journal of Materials Chemistry A* **2014,** *2* (28), 10788-10817.

227.   Burgués-Ceballos, I.; Stella, M.; Lacharmoise, P.; Martínez-Ferrero, E., Towards industrialization of polymer solar cells: material processing for upscaling. *Journal of Materials Chemistry A* **2014,** *2* (42), 17711-17722.

228.   Kaelin, M.; Rudmann, D.; Tiwari, A., Low cost processing of CIGS thin film solar cells. *Solar Energy* **2004,** *77* (6), 749-756.

229.   Hwang, K.; Jung, Y.-S.; Heo, Y.-J.; Scholes, F. H.; Watkins, S. E.; Subbiah, J.; Jones, D. J.; Kim, D.-Y.; Vak, D., Toward Large Scale Roll-to-Roll Production of Fully Printed Perovskite Solar Cells. *Adv Mater* **2015**.

230.   Campoy-Quiles, M.; Ferenczi, T.; Agostinelli, T.; Etchegoin, P. G.; Kim, Y.; Anthopoulos, T. D.; Stavrinou, P. N.; Bradley, D. D.; Nelson, J., Morphology evolution via self-organization and lateral and vertical diffusion in polymer: fullerene solar cell blends. *Nature materials* **2008,** *7* (2), 158-164.

231.   Yeo, J.-S.; Yun, J.-M.; Kim, D.-Y.; Park, S.; Kim, S.-S.; Yoon, M.-H.; Kim, T.-W.; Na, S.-I., Significant vertical phase separation in solvent-vapor-annealed poly (3, 4-ethylenedioxythiophene): poly (styrene sulfonate) composite films leading to better conductivity and work function for high-performance indium tin oxide-free optoelectronics. *ACS applied materials & interfaces* **2012,** *4* (5), 2551-2560.

232.   Chang, C.-Y.; Huang, W.-K.; Chang, Y.-C.; Lee, K.-T.; Chen, C.-T., A solution-processed n-doped fullerene cathode interfacial layer for efficient and stable large-area perovskite solar cells. *J. Mater. Chem. A* **2016,** *4* (2), 640-648.

233.   Tekin, E.; Wijlaars, H.; Holder, E.; Egbe, D. A.; Schubert, U. S., Film thickness dependency of the emission colors of PPE–PPVs in inkjet printed libraries. *Journal of Materials Chemistry* **2006,** *16* (44), 4294-4298.

234.   Hoth, C. N.; Choulis, S. A.; Schilinsky, P.; Brabec, C. J., High photovoltaic performance of inkjet printed polymer: fullerene blends. *Advanced Materials* **2007,** *19* (22), 3973-3978.

235.   Noh, Y.-Y.; Zhao, N.; Caironi, M.; Sirringhaus, H., Downscaling of self-aligned, all-printed polymer thin-film transistors. *Nature nanotechnology* **2007,** *2* (12), 784-789.

236.   Wei, Z.; Chen, H.; Yan, K.; Yang, S., Inkjet printing and instant chemical transformation of a CH3NH3PbI3/nanocarbon electrode and interface for planar perovskite solar cells. *Angewandte Chemie International Edition* **2014,** *53* (48), 13239-13243.

237.   Bag, M.; Jiang, Z.; Renna, L. A.; Jeong, S. P.; Rotello, V. M.; Venkataraman, D., Rapid combinatorial screening of inkjet-printed alkyl-ammonium cations in perovskite solar cells. *Materials Letters* **2016,** *164*, 472-475.

238.   Docampo, P.; Ball, J. M.; Darwich, M.; Eperon, G. E.; Snaith, H. J., Efficient organometal trihalide perovskite planar-heterojunction solar cells on flexible polymer substrates. *Nature communications* **2013,** *4*.

239.   Roldán-Carmona, C.; Malinkiewicz, O.; Soriano, A.; Espallargas, G. M.; Garcia, A.; Reinecke, P.; Kroyer, T.; Dar, M. I.; Nazeeruddin, M. K.; Bolink, H. J., Flexible high efficiency perovskite solar cells. *Energy & Environmental Science* **2014,** *7* (3), 994-997.

240.   Yang, D.; Yang, R.; Zhang, J.; Yang, Z.; Liu, S. F.; Li, C., High efficiency flexible perovskite solar cells using superior low temperature TiO 2. *Energy & Environmental Science* **2015,** *8* (11), 3208-3214.

241.   Yoon, J.; Sung, H.; Lee, G.; Cho, W.; Ahn, N.; Jung, H. S.; Choi, M., Superflexible, high-efficiency perovskite solar cells utilizing graphene electrodes: towards future foldable power sources. *Energy & Environmental Science* **2017**.

242.   Wang, C.; Zhao, D.; Yu, Y.; Shrestha, N.; Grice, C. R.; Liao, W.; Cimaroli, A. J.; Chen, J.; Ellingson, R. J.; Zhao, X., Compositional and morphological engineering of mixed cation perovskite films for highly efficient planar and flexible solar cells with reduced hysteresis. *Nano Energy* **2017,** *35*, 223-232.

243.   Bhandari, K. P.; Collier, J. M.; Ellingson, R. J.; Apul, D. S., Energy payback time (EPBT) and energy return on energy invested (EROI) of solar photovoltaic systems: A systematic review and meta-analysis. *Renewable and Sustainable Energy Reviews* **2015,** *47*, 133-141.

244.   de Wild-Scholten, M. M., Energy payback time and carbon footprint of commercial photovoltaic systems. *Solar Energy Materials and Solar Cells* **2013,** *119*, 296-305.

245.   Goodrich, A.; Hacke, P.; Wang, Q.; Sopori, B.; Margolis, R.; James, T. L.; Woodhouse, M., A wafer-based monocrystalline silicon photovoltaics road map: Utilizing known technology improvement opportunities for further reductions in manufacturing costs. *Solar Energy Materials and Solar Cells* **2013,** *114*, 110-135.

246.   Powell, D. M.; Winkler, M. T.; Choi, H.; Simmons, C. B.; Needleman, D. B.; Buonassisi, T., Crystalline silicon photovoltaics: a cost analysis framework for determining technology pathways to reach baseload electricity costs. *Energy & Environmental Science* **2012,** *5* (3), 5874-5883.

247.   Park, S.-H.; Kim, H.-S., Flash Light Sintering of Nickel Nanoparticles for Printed Electronics. *Thin Solid Films* **2014,** *550*, 575-581.

248.   Kim, H. S.; Dhage, S. R.; Shim, D. E.; Hahn, H. T., Intense pulsed light sintering of copper nanoink for printed electronics. *Appl. Phys. A-Mater. Sci. Process.* **2009,** *97* (4), 791-798.

249.   Perelaer, J.; Abbel, R.; Wuenscher, S.; Jani, R.; van Lammeren, T.; Schubert, U. S., Roll-to-roll Compatible Sintering of Inkjet Printed Features by Photonic and Microwave Exposure. From Non-conductive Ink to 40% Bulk Silver Conductivity in Less Than 15 Seconds. *Adv. Mater. (Weinheim, Ger.)* **2012,** *24* (19), 2620-2625.

250.   Hoesel, M.; Krebs, F. C., Large-scale roll-to-roll photonic sintering of flexo printed silver nanoparticle electrodes. *J. Mater. Chem.* **2012,** *22* (31), 15683-15688.

251.   Kang, J.; Ryu, J.; Kim, H.; Hahn, H., Sintering of inkjet-printed silver nanoparticles at room temperature using intense pulsed light. *Journal of Elec Materi* **2011,** *40* (11), 2268-2277.

252.   Lee, D. J.; Park, S. H.; Jang, S.; Kim, H. S.; Oh, J. H.; Song, Y. W., Pulsed light sintering characteristics of inkjet-printed nanosilver films on a polymer substrate. *Journal of Micromechanics and Microengineering* **2011,** *21* (12), 125023.

253.   Jo, Y.; Oh, S.-J.; Lee, S. S.; Seo, Y.-H.; Ryu, B.-H.; Moon, J.; Choi, Y.; Jeong, S., Extremely flexible, printable Ag conductive features on PET and paper substrates via continuous millisecond photonic sintering in a large area. *J. Mater. Chem. C* **2014,** *2* (45), 9746-9753.

254.   Ryu, J.; Kim, H.-S.; Hahn, H. T., Reactive sintering of copper nanoparticles using intense pulsed light for printed electronics. *Journal of Elec Materi* **2011,** *40* (1), 42-50.

255.   Zarazua, I.; Han, G.; Boix, P. P.; Mhaisalkar, S.; Fabregat-Santiago, F.; Mora-Seró, I.; Bisquert, J.; Garcia-Belmonte, G., Surface Recombination and Collection Efficiency in Perovskite Solar Cells from Impedance Analysis. *J. Phys. Chem. Lett* **2016,** *7* (24), 5105-5113.

256.   Jamnik, J.; Maier, J., Treatment of the impedance of mixed conductors equivalent circuit model and explicit approximate solutions. *Journal of the Electrochemical society* **1999,** *146* (11), 4183-4188.

257.   Chopra, K.; Paulson, P.; Dutta, V., Thin-film solar cells: an overview. *Progress in Photovoltaics: Research and Applications* **2004,** *12* (2-3), 69-92.

258.   Bhattacharya, R.; Rajeshwar, K., Electrodeposition of CdTe thin films. *Journal of the Electrochemical Society* **1984,** *131* (9), 2032-2037.

259.   Scheer, R.; Schock, H.-W., *Chalcogenide photovoltaics: physics, technologies, and thin film devices*. John Wiley & Sons: 2011.

260.   Brewer, P.; Zinck, J.; Olson, G., Reversible modification of CdTe surface composition by excimer laser irradiation. *Applied physics letters* **1990,** *57* (24), 2526-2528.

261.   Dharmadasa, I. M.; Echendu, O. K.; Fauzi, F.; Abdul-Manaf, N. A.; Salim, H. I.; Druffel, T.; Dharmadasa, R.; Lavery, B., Effects of CdCl2 treatment on deep levels in CdTe and their implications on thin film solar cells: a comprehensive photoluminescence study. *J. Mater. Sci.: Mater. Electron.* **2015,** *26* (7), 4571-4583.

262.   Scragg, J. J., *Copper Zinc Tin Sulfide Thin Films for Photovoltaics: Synthesis and Characterisation by Electrochemical Methods*. Springer Science & Business Media: 2011.

263.   Klahr, B.; Gimenez, S.; Fabregat-Santiago, F.; Bisquert, J.; Hamann, T. W., Photoelectrochemical and impedance spectroscopic investigation of water oxidation with "Co–Pi"-coated hematite electrodes. *Journal of the American Chemical Society* **2012,** *134* (40), 16693-16700.

264.   Nakagawa, H.; Matsumoto, H., Optical Absorption and Luminescence of the I−-Center in CdCl2. *Journal of the Physical Society of Japan* **1974,** *36* (6), 1577-1582.

265.   Moutinho, H.; Al-Jassim, M.; Levi, D.; Dippo, P.; Kazmerski, L., Effects of CdCl 2 treatment on the recrystallization and electro-optical properties of CdTe thin films. *Journal of Vacuum Science & Technology A: Vacuum, Surfaces, and Films* **1998,** *16* (3), 1251-1257.

266.   Geiler, H. D.; Glaser, E.; Götz, G.; Wagner, M., Explosive crystallization in silicon. *Journal of applied physics* **1986,** *59* (9), 3091-3099.

267.   Ohdaira, K.; Fujiwara, T.; Endo, Y.; Nishizaki, S.; Matsumura, H., Explosive crystallization of amorphous silicon films by flash lamp annealing. *Journal of Applied Physics* **2009,** *106* (4), 044907.

268.   Pore, V.; Ritala, M.; Leskelä, M.; Saukkonen, T.; Järn, M., Explosive crystallization in atomic layer deposited mixed titanium oxides. *Crystal Growth and Design* **2009,** *9* (7), 2974-2978.

269.   Wood, D.; Rogers, K.; Lane, D.; Coath, J., Optical and structural characterization of CdSxTe1-x thin films for solar cell applications. *Journal of Physics: Condensed Matter* **2000,** *12* (19), 4433.

270.   Zanio, K.; Pollak, F. H., Semiconductors and Semimetals, Vol. 13 (Cadmium Telluride). *Physics Today* **1978,** *31*, 53.

271.   Dharmadasa, I., Recent developments and progress on electrical contacts to CdTe, CdS and ZnSe with special reference to barrier contacts to CdTe. *Progress in crystal growth and characterization of materials* **1998,** *36* (4), 249-290.

272.   Hernandez-Fenollosa, M.; Halliday, D.; Durose, K.; Campo, M.; Beier, J., Photoluminescence studies of CdS/CdTe solar cells treated with oxygen. *Thin Solid Films* **2003,** *431*, 176-180.

273.   Mazzamuto, S.; Vaillant, L.; Bosio, A.; Romeo, N.; Armani, N.; Salviati, G., A study of the CdTe treatment with a Freon gas such as CHF 2 Cl. *Thin Solid Films* **2008,** *516* (20), 7079-7083.

274.   Dharmadasa, I.; Thornton, J.; Williams, R., Effects of surface treatments on Schottky barrier formation at metal/n-type CdTe contacts. *Applied physics letters* **1989,** *54* (2), 137-139.

275.   Ayoub, M.; Hage-Ali, M.; Zumbiehl, A.; Regal, R.; Koebel, J.; Rit, C.; Fougeres, P.; Siffert, P., Study of the resistivity mapping in CdTe: Cl-correlation with annealing and Te-precipitates. *IEEE Transactions on nuclear science* **2002,** *49* (4), 1954-1959.

276.   Bugar, M.; Belas, E.; Grill, R.; Prochazka, J.; Uxa, Š.; Hlidek, P.; Franc, J.; Fesh, R.; Hoschl, P., Inclusions elimination and resistivity restoration of CdTe: Cl crystals by two-step annealing. *IEEE Transactions on nuclear science* **2011,** *58* (4), 1942-1948.

277.   Ayoub, M.; Hage-Ali, M.; Koebel, J.; Zumbiehl, A.; Klotz, F.; Rit, C.; Regal, R.; Fougeres, P.; Siffert, P., Annealing effects on defect levels of CdTe: Cl materials and the uniformity of the electrical properties. *IEEE Transactions on nuclear science* **2003,** *50* (2), 229-237.

278.   Hiie, J., CdTe: CdCl 2: O 2 annealing process. *Thin Solid Films* **2003,** *431*, 90-93.

279.   Dharmadasa, I., Review of the CdCl2 Treatment Used in CdS/CdTe Thin Film Solar Cell Development and New Evidence towards Improved Understanding. *Coatings* **2014,** *4* (2), 282-307.

280.   Liang, P. W.; Liao, C. Y.; Chueh, C. C.; Zuo, F.; Williams, S. T.; Xin, X. K.; Lin, J. J.; Jen, A. K. Y., Additive Enhanced Crystallization of Solution-Processed Perovskite for Highly Efficient Planar-Heterojunction Solar Cells. *Advanced Materials* **2014,** *26* (22), 3748-3754.

281.   Salim, T.; Sun, S.; Abe, Y.; Krishna, A.; Grimsdale, A. C.; Lam, Y. M., Perovskite-based Solar Cells: Impact of Morphology and Device Architecture on Device Performance. *Journal of Materials Chemistry A* **2015,** *3* (17), 8943-8969.

282.   Readey, D.; Quadir, T.; Lee, J., Effects of vapor transport on microstructure development. In *Ceramic Microstructures' 86*, Springer: 1987; pp 485-496.

283.   McIntyre, R., The Effect of HCl-H2 Sintering on the Properties of Compacted Iron Powder. In *Iron Powder Metallurgy*, Springer: 1968; pp 249-254.

284.   Readey, M. J.; Readey, D. W., Sintering of ZrO2 in HCl atmospheres. *Journal of the American Ceramic Society* **1986,** *69* (7), 580-582.

285.   Leyden, M. R.; Lee, M. V.; Raga, S. R.; Qi, Y., Large Formamidinium Lead Trihalide Perovskite Solar Cells Using Chemical Vapor Deposition with High Reproducibility and Tunable Chlorine Concentrations. *Journal of Materials Chemistry A* **2015,** *3* (31), 16097-16103.

286.   Saliba, M.; Tan, K. W.; Sai, H.; Moore, D. T.; Scott, T.; Zhang, W.; Estroff, L. A.; Wiesner, U.; Snaith, H. J., Influence of Thermal Processing Protocol upon the Crystallization and Photovoltaic Performance of Organic-Inorganic Lead Trihalide Perovskites. *J. Phys. Chem. C* **2014,** *118* (30), 17171-17177.

287.   Coble, R., Initial sintering of alumina and hematite. *Journal of the American Ceramic Society* **1958,** *41* (2), 55-62.

288.   Dharmadasa, R.; Dharmadasa, I.; Druffel, T., Intense Pulsed Light Sintering of Electrodeposited CdS Thin Films. *Advanced Engineering Materials* **2014,** *16* (11), 1351-1361.

289.   Pisoni, A.; Jaćimović, J.; Barišić, O. S.; Spina, M.; Gaál, R.; Forró, L.; Horváth, E., Ultra-Low Thermal Conductivity in Organic–Inorganic Hybrid Perovskite CH3NH3PbI3. *The Journal of Physical Chemistry Letters* **2014,** *5* (14), 2488-2492.

290.   Song, Z. N.; Watthage, S. C.; Phillips, A. B.; Tompkins, B. L.; Ellingson, R. J.; Heben, M. J., Impact of Processing Temperature and Composition on the Formation of Methylammonium Lead Iodide Perovskites. *Chemistry of Materials* **2015,** *27* (13), 4612-4619.

291.   Xie, Y.; Shao, F.; Wang, Y.; Xu, T.; Wang, D.; Huang, F., Enhanced Performance of Perovskite CH3NH3PbI3 Solar Cell by Using CH3NH3I as Additive in Sequential Deposition. *ACS Appl. Mater. Interfaces* **2015,** *7* (23), 12937-12942.

292.   Leijtens, T.; Lauber, B.; Eperon, G. E.; Stranks, S. D.; Snaith, H. J., The Importance of Perovskite Pore Filling in Organometal Mixed Halide Sensitized TiO2-Based Solar Cells. *The Journal of Physical Chemistry Letters* **2014,** *5* (7), 1096-1102.

293.   Nguyen, W. H.; Bailie, C. D.; Unger, E. L.; McGehee, M. D., Enhancing the Hole-Conductivity of Spiro-OMeTAD without Oxygen or Lithium Salts by Using Spiro(TFSI)(2) in Perovskite and Dye-Sensitized Solar Cells. *Journal of the American Chemical Society* **2014,** *136* (31), 10996-11001.

294.   Mitzi, D. B., Solution-processed inorganic semiconductors. *Journal of Materials Chemistry* **2004,** *14* (15), 2355-2365.

295.   Ishihara, T.; Takahashi, J.; Goto, T., Exciton state in two-dimensional perovskite semiconductor (C10H21NH3) 2PbI4. *Solid state communications* **1989,** *69* (9), 933-936.

296.   Hong, X.; Ishihara, T.; Nurmikko, A., Dielectric confinement effect on excitons in PbI 4-based layered semiconductors. *Physical Review B* **1992,** *45* (12), 6961.

297.   Muljarov, E.; Tikhodeev, S.; Gippius, N.; Ishihara, T., Excitons in self-organized semiconductor/insulator superlattices: PbI-based perovskite compounds. *Physical Review B* **1995,** *51* (20), 14370.

298.   Borisenko, V.; Hesketh, P. J., *Rapid thermal processing of semiconductors*. Springer Science & Business Media: 2013.

299.   Liu, J.; Leng, J.; Wu, K.; Zhang, J.; Jin, S., Observation of Internal Photoinduced Electron and Hole Separation in Hybrid 2-Dimentional Perovskite Films. *Journal of the American Chemical Society* **2017**.

300.   Paek, S.; Schouwink, P.; Athanasopoulou, E. N.; Cho, K.; Grancini, G.; Lee, Y.; Zhang, Y.; Stellacci, F.; Nazeeruddin, M. K.; Gao, P., From Nano to Micrometer Scale: The Role of Anti-Solvent Treatment on High Performance Perovskite Solar Cells. *Chemistry of Materials* **2017**.

301.   Fedeli, P.; Gazza, F.; Calestani, D.; Ferro, P.; Besagni, T.; Zappettini, A.; Calestani, G.; Marchi, E.; Ceroni, P.; Mosca, R., Influence of the Synthetic Procedures on the Structural and Optical Properties of Mixed-Halide (Br, I) Perovskite Films. *The Journal of Physical Chemistry C* **2015,** *119* (37), 21304-21313.

302.   Cody, G.; Tiedje, T.; Abeles, B.; Brooks, B.; Goldstein, Y., Disorder and the optical-absorption edge of hydrogenated amorphous silicon. *Physical Review Letters* **1981,** *47* (20), 1480.

303.   Shen, W.; Jiang, L.; Yang, H.; Meng, F.; Ogawa, H.; Guo, Q., Bandtail characteristics in InN thin films. *Applied physics letters* **2002,** *80* (12), 2063-2065.

304.   Hassanien, A.; Akl, A. A., Influence of composition on optical and dispersion parameters of thermally evaporated non-crystalline Cd 50 S 50− x Se x thin films. *Journal of Alloys and Compounds* **2015,** *648*, 280-290.

305.   Stoumpos, C. C.; Cao, D. H.; Clark, D. J.; Young, J.; Rondinelli, J. M.; Jang, J. I.; Hupp, J. T.; Kanatzidis, M. G., Ruddlesden-Popper Hybrid Lead Iodide Perovskite 2D Homologous Semiconductors. *Chem. Mater.* **2016,** *28* (8), 2852-2867.

306.   Yang, S.; Niu, W.; Wang, A. L.; Fan, Z.; Chen, B.; Tan, C.; Lu, Q.; Zhang, H., Ultrathin Two-Dimensional Organic–Inorganic Hybrid Perovskite Nanosheets with Bright, Tunable Photoluminescence and High Stability. *Angewandte Chemie International Edition* **2017**.

307.   Gan, X.; Wang, O.; Liu, K.; Du, X.; Guo, L.; Liu, H., 2D homologous organic-inorganic hybrids as light-absorbers for planer and nanorod-based perovskite solar cells. *Solar Energy Materials and Solar Cells* **2017,** *162*, 93-102.

308.   Bisquert, J.; Mora-Sero, I.; Fabregat-Santiago, F., ChemElectroChem, 2014, 1, 289. *Journal of Materials Chemistry A Communication*.

309.   Dualeh, A.; Moehl, T.; Tétreault, N.; Teuscher, J.; Gao, P.; Nazeeruddin, M. K.; Grätzel, M., Impedance Spectroscopic Analysis of Lead Iodide Perovskite-Sensitized Solid-State Solar Cells. *ACS Nano* **2014,** *8* (1), 362-373.

310.   Bag, M.; Renna, L. A.; Adhikari, R. Y.; Karak, S.; Liu, F.; Lahti, P. M.; Russell, T. P.; Tuominen, M. T.; Venkataraman, D., Kinetics of Ion Transport in Perovskite Active Layers and Its Implications for Active Layer Stability. *J. Am. Chem. Soc.* **2015,** *137* (40), 13130-13137.

311.   Azpiroz, J. M.; Mosconi, E.; Bisquert, J.; De Angelis, F., Defect migration in methylammonium lead iodide and its role in perovskite solar cell operation. *Energy & Environmental Science* **2015,** *8* (7), 2118-2127.

CURRICULUM VITAE

Brandon W. Lavery

12111 Circuit Street, Waterford, PA 16441   (814) 460-2004 |
brandon.lavery@icloud.com

EDUCATION

University of Louisville
Louisville, KY
Doctoral Student in Chemical Engineering
2012 to 2017
Thesis: Scalable Manufacturing of Perovskite Solar Cells
GPA: 3.85
Case Western Reserve University
Cleveland, OH
Bachelor of Science in Chemical Engineering
May 2012
Involved in undergraduate research with Dr. Robert Savinell

SKILLS

Programming Languages: Experienced in Java, and HTML
Software: AutoCAD, ChemCAD, Comsol, LabVIEW, MATLAB, Minitab, Multisim, Origin, Microsoft Office, and Crystal Maker
Analytical Characterization Techniques: Scanning Electron Microscopy (**SEM**), X-ray Diffraction (**XRD**), **UV-Vis** Spectroscopy, Cryo Photoluminescence (**PL**), Cyclic Voltammetry, Voltage Sweeps to determine **solar cell efficiency**, Electrochemical Impedance Spectroscopy (**EIS**), Photolectrochemical measurements (**PEC**), Profilometer, Fourier transform infrared spectroscopy (**FTIR**)

- Utilized UV-Visible Absorption Spectroscopy, Scanning Electron Microscopy (SEM), X-Ray Diffraction (XRD), Photoluminescence (PL), Photoelectrochemical (PEC) measurements, and Current Vs. Voltage (JV) efficiency measurements to improve solar cell physical attributes, chemical makeup, and optical properties

Process Engineering: Wet Etching, Spin Coating, Doctor Blading, Thermal Evaporation, Atomic Layer Deposition (**ALD**), Ultra-Sonic Spray Coating, Chemical Bath Deposition, Intense-Pulsed Light Sintering, Electrochemical Deposition, UV and Plasma Cleaning, Small Batch Chemical Synthesis, Vacuum Filtration, Centrifugation, sputtering, **clean room experience**

- Assembled and maintained nitrogen glove box
- Fixed a program for an ultra-sonic spray by using LabView coding

- Repaired and maintained the following equipment: ALD reactor, spin-coater for thin film deposition, XRD instrument, UV-Vis spectroscopy instrument, SEM, PL, profilometer, sputtering system, and a thermal evaporator
  - **Established SOP** for glove box operations, thermal evaporator, and ALD of titanium dioxide and aluminum oxide
- Modified and corrected piping and instrumentation diagrams for 20 reactors at LORD Corporation using AutoCAD
- **Trained** incoming chemical engineers for LORD Corporation

PROFESSIONAL & RESEARCH EXPERIENCE

Conn Center Renewable Energy Lab
Louisville, KY
Graduate Research Assistant
Fall 2012-Current

- **Exploration of intense-pulsed light (IPL) photonic process engineering in CdTe solar cell technology**
  - Intense-pulsed light is the process of using a xenon lamp in a fraction of a second over a wide area to induce a high temperature thermal gradient within a light absorbing material.
  - **Electrodeposited** cadmium telluride (**CdTe**) thin film solar cells were post-treated with IPL to minimize grain boundaries by sintering the CdTe, resulting in higher solar cell efficiency.
    - Enabled by process engineering the electrodeposition to produce cadmium-rich CdTe with a lower melting temperature needed for photonic IPL sintering
    - Improved the CdTe solar cell efficiency with IPL by growing the grains from nanometer to micron size and decreasing the amount of grain boundary recombination centers that decrease cell performance
      - Created the micron-sized grains in under 2 minutes which is faster and more economical than the 30 minutes required by conventional oven techniques
    - Uncovered the mechanism behind enhancing CdTe solar cell efficiency with the popular cadmium chloride treatment
      - Low temperature liquid nitrogen PL was used to view sub-band gap defect states in CdTe before and after cadmium chloride treatment to understand the performance improvements
        - Findings led to redesign of CdTe bath precursors from cadmium sulfate to cadmium chloride and cadmium nitrate precursors
        - Efficiencies of cells increased from 12 to over 15% with new precursors
- **Photonic process engineering of perovskite organic/inorganic solar cells**
  - Created a wet chemistry thin-film manufacturing platform that increased solar cell efficiency from **2 to 16% in one year** using sol-gel and organic halide chemistries
  - Expertise in metal oxide sol-gel and ALD processing needed for high efficiency solar cells
  - Published the first reported sintering of methylammonium lead iodide perovskite solar cells

- Proficiency in **wet etching** of conductive oxides (fluorinated tin oxide (FTO)) with zinc powder and hydrochloric acid was used to create defined counter electrode contacts
- Engineered the **spin coating** processes of depositing titanium dioxide, perovskite, and the organic hole-transport layer Spiro-MeOTAD with excellent accuracy and reproducibility to limit film thickness deviations to within 50 nanometers
  - Experience with surface treatment effects of **UV and oxygen plasma cleaning** on FTO conductive glass led to pinhole-free spin coating of titanium dioxide on glass substrates
- Background in **chemical bath depositions (CBD)** using titanium tetrachloride $TiCl_4$ helped to improve the coverage of the titanium dioxide hole blocking layer and improve solar cell performance
  - Creation of a Comsol **finite element analysis (FEA)** quantitative modeling to study **thermodynamics** in intense pulsed light
    - Used to uncover the temperatures experienced by thin films in the millisecond regime to help predict kinetics of formation for materials and save hours and materials that would be wasted in trial and error based experiments
  - Development of 2-D organometal halide materials with a strong understanding of crystallography phase changes and underlying kinetics

Electrochemical Engineering and Energy Lab
Cleveland, OH
Undergraduate Research Assistant
Fall 2011-2012
- Explored the effects of cell membrane on the conductivities of fuel cells
  - Various membranes were tested under a variety of temperatures to determine the temperature dependence of the membranes' conductivities

Lord Corporation, Saegertown, PA Facility
Saegertown, PA
Chemical Engineering Summer Intern
2009-2011
- Designed new air cylinder mezzanine gates and led as the foreman during construction
- Rerouted a nitrogen generation pressure swing absorption (PSA) system to save cost of using liquid nitrogen
  - Research led to the discovery of a faulty automatic valve restricting the nitrogen generation system and forcing the entire chemical facility to use liquid nitrogen during peak hours of operation
- Led a project that replaced a hazardous chemical storage tank with a safe fiberglass reinforced plastic tank

CURRENT PUBLICATIONS

1. Lavery, B. W.; Kumari, S.; Konermann, H.; Draper, G.; Spurgeon, J. M.; Druffel, T. L., Intense Pulsed Light Sintering of CH3NH3PbI3 Solar Cells. *ACS applied materials & interfaces* 2016, 8 (13), 8419-8426.

2. Rajamanickam, N.; Kumari, S.; Vendra, V. K.; <u>Lavery, B. W.</u>; Spurgeon, J.; Druffel, T.; Sunkara, M. K., Stable and durable CH3NH3PbI3 perovskite solar cells at ambient conditions. *Nanotechnology* 2016**,** *27* (23), 235404.

3. Draper, G. L.; Dharmadasa, R.; Staats, M. E.; <u>Lavery, B. W.</u>; Druffel, T., Fabrication of Elemental Copper by Intense Pulsed Light Processing of a Copper Nitrate Hydroxide Ink. *ACS Appl. Mater. Interfaces* 2015**,** *7* (30), 16478-16485.

4. Dharmadasa, R.; <u>Lavery, B.</u>; Dharmadasa, I. M.; Druffel, T., Intense Pulsed Light Treatment of Cadmium Telluride Nanoparticle-Based Thin Films. *ACS Appl. Mater. Interfaces* 2014**,** *6* (7), 5034-5040.

5. Dharmadasa, I. M.; Echendu, O. K.; Fauzi, F.; Abdul-Manaf, N. A.; Salim, H. I.; Druffel, T.; Dharmadasa, R.; <u>Lavery, B.</u>, Effects of CdCl2 treatment on deep levels in CdTe and their implications on thin film solar cells: a comprehensive photoluminescence study. *J. Mater. Sci.: Mater. Electron.* 2015**,** *26* (7), 4571-4583.

6. Dharmadasa, R.; <u>Lavery, B. W.</u>; Dharmadasa, I.; Druffel, T., Processing of CdTe thin films by intense pulsed light in the presence of CdCl2. *Journal of Coatings Technology and Research* 2015**,** *12* (5), 835-842.

7. Dharmadasa, I. M.; Madugu, M. L.; Olusola, O. I.; Echendu, O. K.; Fauzi, F.; Diso, D. G.; Weerasinghe, A. R.; Druffel, T.; Dharmadasa, R.; <u>Lavery, B.</u>, Electroplating of CdTe thin films from cadmium sulphate precursor and comparison of layers grown by 3-electrode and 2-electrode systems. *Coatings* 2017**,** *7* (2), 17.

FUTURE PUBLICATIONS

8. Krishnamraju A.; <u>Lavery, B.W.</u>; Druffel, T., Atmospheric Processing of Perovskite Solar Cells using Intense Pulse Light Sintering. 2017.

9. <u>Lavery, B.W.</u>; Ankireddy, K.; Druffel, T., Bandgap Tuning of 2-D Perovskite Materials using Intense Pulsed Light. 2017.

10. <u>Lavery, B.W.</u>; Ankireddy, K.; Druffel, T., Mechanisms of Photonic Sintering in Perovskite Solar Cells. 2017.

11. Druffel, T.; Ankireddy, K.; <u>Lavery, B.W.</u>, A Review of Intense Pulsed Light Sintering. 2017.

12. <u>Lavery, B. W.</u>; Venkat, V.; Druffel, T.; Sunkara, M., Progress and challenges with durability and scalable manufacturing of perovskite based solar cells. 2017.

13. Thapa, A.; <u>Lavery, B.W.</u>; Babajide, P.; Druffel, T.; Sumanasekera, G., High Capacity NMC cathode for Li-ion Batteries by Co-precipitation Method. 2017.

CURRENT RESEARCH PROJECTS

- **Solving the manufacturing reproducibility problems of the perovskite solar cell (PSC)** by utilizing finite element analysis simulations and experimental results to determine the fundamental sintering mechanisms in perovskites by matching the sintering energies to bond-dissociation energies and relating the IPL-induced temperatures to melting point temperatures

- **Tuning the 2-D Perovskite band gap** by using intense pulsed light to eliminate longer chain organic cations in-between 3-D lead iodide octahedra structures to selectively choose the periodicity of 2-D layers which determines the band gap in 2-D perovskites

PRESENTATIONS AND AWARDS

- **Conferences**
  - **1st Place** in the 2015 poster presentation at the RE3 renewable energy conference, Poster and Oral Presentation in 2015 ECS Phoenix Conference, **3rd Place** in the 2013 poster contest at the University of Louisville Graduate Research Symposium, Honorable mention in the 2013 poster presentation at the RE3 renewable energy conference
- **Scholarships**
  - **Provost's special scholarship** 2008-2012 (Case Western), Lawrence scholarship 2008-2012 (Case Western), Cross scholarship 2008-2016
- **Other Awards and Certifications**
- **1st Place** in regional JETS (Junior Engineering Technical Society) competition 2008, **Eagle scout** award from Boy Scouts of America 2006, **Lean Six Sigma Green Belt** 2017

REFERENCES

- **Dr. Thad Druffel** email: thad.druffel@louisville.edu , phone: 502-338-6476
- **Dr. Mahendra Sunkara** email: mahendra@louisville.edu , phone: 502-439-5896
- **Dr. William (Hank) Paxton** email: william.paxton@louisville.edu , phone: 270-331-1116